

From brain tissue to structure:
The architecture of α -amino-3-hydroxy-5-methyl-4-isoxazolepropionic
acid receptors from two distinct brain regions

by

Prashant A. Rao

A DISSERTATION

Presented to the Neuroscience Graduate Program
and the Oregon Health & Science University

School of Medicine

in partial fulfillment

of the requirements for the degree of

Doctor of Philosophy

March 2023

School of Medicine
Oregon Health & Science University

CERTIFICATE OF APPROVAL

This is to certify that the Ph.D. dissertation of
PRASHANT A. RAO
has been approved

Mentor/Advisor, Eric Gouaux, Ph.D.

Member and Chair, Steve Reichow, Ph.D.

Member, Francis Valiyaveetil, Ph.D.

Member, Larry Trussell, Ph.D.

Member, Sasha Sobolevsky, Ph.D.

TABLE OF CONTENTS

ACKNOWLEDGEMENTS	iii
LIST OF FIGURES AND TABLES.....	v
LIST OF ABBREVIATIONS.....	vi
ABSTRACT	vii

CHAPTER 1: Introduction

Ligand-gated ion channels in the central nervous system.....	1
Ionotropic glutamate receptors	3
AMPA receptors mediate excitatory synaptic transmission	4
Molecular architecture of AMPA receptors.....	6
Biophysical properties of AMPARs: ion permeation, kinetics, gating cycle.....	9
AMPA receptor assembly: subunit composition and auxiliary proteins	15
Studying native AMPAR complexes: significance and approach	21
Prelude to the dissertation.....	24

CHAPTER 2: Immunoaffinity purification of native AMPARs from mammalian brain tissue

Purification and biochemical analysis of native AMPA receptors from three different mammalian species
(*PLOS One*, Published)

CHAPTER 3: Architecture and molecular composition of hippocampal AMPARs

Hippocampal AMPA receptor assemblies and mechanism of allosteric inhibition
(*Nature*, Published)

CHAPTER 4: Architecture and conformational mobility of calcium-permeable cerebellar AMPARs

ABSTRACT	73
----------------	----

INTRODUCTION	74
MATERIALS AND METHODS	76
Purification of 3x-FLAG-tagged 11b8 scFv	76
Preparation of mouse cerebella.....	76
Immunoaffinity purification of GluA1-containing CP-AMPARs.....	76
Cryo-EM data acquisition.....	77
Cryo-EM data processing	77
RESULTS.....	78
Immunoaffinity purification of cerebellar GluA1-containing CP-AMPARs	78
Conformational mobility of ATD dimers	80
Structure determination of the LBD-TMD layer	84
Architecture of the LBD layer.....	85
Putative TARP-like densities at the B'/D' positions	86
Interactions between the M3-S2 linkers.....	87
The upper gate adopts a compact, asymmetric conformation	89
Defining subunit occupancy for cerebellar CP-AMPARs.....	89
DISCUSSION	91
CHAPTER 5: Concluding remarks	
OUTLOOK AND SUMMARY.....	97
FUTURE DIRECTIONS	99
REFERENCES	101

Acknowledgements

My time in OHSU has been the most formative experience of my life, both scientifically and socially. I genuinely believe that success can never be solely attributed to one individual, and thus, my dissertation would not be possible without the help, support, and guidance from a number of people.

I would like to begin by thanking Dr. Sriram Subramaniam, who took a chance on me, despite my inexperience and naivety as a young kid with minimal research experience, and gave me an opportunity to work in his lab. That experience enabled me to develop my passion for cryo-EM and laid the foundation for the scientist I have developed into now. In his lab, I was surrounded by incredible scientists and people, all of whom, collectively inspired me to take the leap into graduate school. Specifically, Joel Meyerson, Alan Merk, and Kedar Narayan gave me the confidence to pursue graduate school, and importantly, served as benchmarks of success that I strive to emulate. Without their example and support, I would not have reached this point.

Second, I would like to thank current and former Gouaux lab members, who made the lab a truly special place. I could not be more grateful to have interacted and become friends with so many wonderful people. In particular, I benefited greatly from Yan Zhao and Zad Jalali-Yazdi's expertise, who challenged me with their ideas, comments, and insight. I also want to thank Vikas Navratna, April Goehring, Steve Mansoor, Sarah Clark, and Jonathan Coleman, all of whom were immensely supportive in multiple ways. A special thank you to Vikas for bringing me delicious food many times with no expectation of repayment. And to April, who was enormously patient when helping me overcome my struggles with molecular biology.

I'd also like to thank Claudia Lopez and Craig Yoshioka at the Pacific Northwest Cryo-EM Center who provided excellent support for scheduling and operation of the microscopes, but also their willingness to help me at all times. I consider PNCC to be the top cryo-EM national lab, largely because of them. Separately, I'd like to thank all the members of my thesis dissertation committee for dedicating their time to support me and advise my research. And Isabelle, Arpita,

Rich, Alex, James, and Kim, who made the past several years on the first floor a fantastic experience.

To my parents and my brother, Vishnu, thank you so much. The scientist I have become, and will continue to develop into, is large part due to all of you. To my brother, for setting the bar high and providing an example of selfless and tireless commitment towards a goal – thank you. To my mom, who is by far the most special person in my life, who sends me food from across the country, provides me with love, optimism and wisdom, and encourages me to be my best self – I dedicate this dissertation to you. And to my Dad, who is my scientific hero, which I say with zero exaggeration. Your genuine passion for science, and idealistic pursuit of knowledge, without any desire for recognition or status, is the standard that I aspire to achieve.

Finally, to Eric, my mentor, who has had the greatest impact on my success – thank you. During our first meeting after beginning my rotation, you pointed out that one of my FSEC traces which was labeled as a “negative control” was, in fact, not a negative control. You mentioned that if there is only one thing you take away from your PhD, it is how to setup controls. Even though you were partially joking, that sentiment has stuck with me. I have, and will continue to take all your words, support, and guidance to heart. You are uncompromisingly meticulous, and have provided assurance, guidance, and patience, at every point during my time in your lab. While this marathon is over, I am excited to begin the next one.

List of Figures and Tables

FIGURE 1.1. SCHEMATIC REPRESENTATION OF A GLUTAMATERGIC SYNAPSE.....	5
FIGURE 1.2. AMPAR ARCHITECTURE AND DOMAIN ARRANGEMENT.....	7
FIGURE 1.3. Ca^{2+} PERMEABILITY AND THE ION PERMEATION PATHWAY	10
FIGURE 1.4. ASSEMBLY AND TOPOLOGY OF THE MOST ABUNDANT AUXILIARY PROTEINS.....	17
FIGURE 1.5. SUBUNIT-SPECIFIC LABELING OF NATIVE AMPARS USING ANTIBODY FRAGMENTS	23
FIGURE 4.1. IMMUNOAFFINITY PURIFICATION WORKFLOW TO ISOLATE CEREBELLAR CP-AMPARS	78
FIGURE 4.2. BIOCHEMICAL & CRYO-EM ANALYSIS OF GLUA1-CONTAINING CEREBELLAR CP-AMPARS.....	79
FIGURE 4.3. DATA PROCESSING TO RESOLVE THE STRUCTURE OF A SINGLE ATD DIMER	80
FIGURE 4.4. DEFINING TWO CONFORMATIONS OF A GLUA1-CONTAINING ATD DIMER.....	81
FIGURE 4.5. STRUCTURAL MODELING OF THE ATD LAYER	82
FIGURE 4.6. DATA PROCESSING WORKFLOW TO RESOLVE THE LBD-TMD LAYER.....	83
FIGURE 4.7. THE CRYO-EM STRUCTURE OF THE LBD-TMD LAYERS.....	84
FIGURE 4.8. ARCHITECTURE OF THE LBD LAYER.....	85
FIGURE 4.9. TARP-LIKE DENSITY FEATURES AT THE B'/D' POSITIONS	86
FIGURE 4.10. STRUCTURAL AND GEOMETRIC ANALYSIS OF THE GATING MACHINERY	88
FIGURE 4.11. POSITIONAL OCCUPANCY OF GLUA1 IN THE LBD-TMD MAP	90
TABLE 4.1. CRYO-EM DATA COLLECTION AND PROCESSING STATISTICS	95

List of Abbreviations

AMPA	α -amino-3-hydroxy-5-methyl-4-isoxazolepropionic acid receptor
ATD	amino terminal domain
CI-AMPA	calcium-impermeable AMPA receptor
CKAMP	cystine-knot AMPAR modulating protein
CNIH	cornichon
CNS	central nervous system
COM	center of mass
CP-AMPA	calcium-permeable AMPA receptor
CPT1c	carnitine palmitoyl-transferase 1C
Cryo-EM	cryo-electron microscopy
CTD	carboxy-terminal domain
CTF	contrast transfer function
EDTA	ethylenediaminetetraacetic acid
EM	electron microscopy
EPSC	excitatory postsynaptic current
ER	endoplasmic reticulum
Fab	fragment antibody
FRRS1L	ferric chelate reductase 1-like
FSEC	fluorescence size-exclusion chromatography
Glu	glutamate
GlyR	glycine receptor
GSG1L	germline-specific gene 1-like
iGluR	ionotropic glutamate receptor
IPTG	Isopropyl β -D-1-thiogalactopyranoside
LBD	ligand binding domain
LGIC	ligand-gated ion channel
LL	lower lobe
mAb	monoclonal antibody
MND	motor neuron disease
MPQX	[[3,4-Dihydro-7-(4-morpholinyl)-2,3-dioxo-6-(trifluoromethyl)-1(2 <i>H</i>)-quinoxaliny]methyl]phosphonic acid
ms	milliseconds
NMDA	n-methyl-D-aspartate
NP1	neuronal pentraxin-1
PCR	polymerase chain reaction
PDB	protein data bank
scFv	single-chain variable fragment
SEC	size-exclusion chromatography
SynDIG	synapse differentiation-inducing gene protein
TARP	transmembrane AMPA receptor regulatory protein
TBS	tris-buffered saline
TM	transmembrane
TMD	transmembrane domain
UL	upper lobe

Abstract

Throughout the central nervous system (CNS), a family of ligand-gated ion channels known as α -amino-3-hydroxy-5-methyl-4-isoxazolepropionic acid receptors (AMPA_Rs) translate chemical signals to electrical impulses. AMPA_Rs are cation-selective receptors clustered near pre-synaptic glutamate release sites which open their transmembrane pore upon binding glutamate. This sub-millisecond opening results in depolarization of the postsynaptic membrane, activating a diverse range of signal transduction pathways and cellular processes. AMPA_Rs are tetramers, comprised of four homologous subunits – GluA1-4, assembling as both homomers and heteromers. The majority of AMPA_Rs are heteromeric GluA2-containing assemblies, while those lacking a GluA2 subunit constitute a distinct subtype which are permeable to calcium and display inward rectification, higher single-channel conductance, and faster kinetics. AMPA_Rs do not act alone; indeed, over 10 different auxiliary proteins can decorate the periphery of the receptor and shape subcellular trafficking, pharmacology, and kinetic properties. Consequently, the functional and biophysical properties of AMPA_Rs are underpinned by distinct region-specific expression patterns of receptor subunits and auxiliary proteins.

While structural mechanisms of receptor gating and kinetics have been proposed through decades of recombinant investigations, these studies are limited to the use of engineered receptor/auxiliary protein complexes, which have difficulty replicating the *in vivo* assembly and architecture of AMPA_Rs. This absence of structural information prevents not only a *bona fide* understanding of these receptor complexes, but also an accurate blueprint from which to study their kinetics and physiology. Therefore, to resolve the architecture and assembly of native AMPA_Rs, I employed an immunoaffinity purification strategy, leveraging modified antibody fragments with engineered affinity tags to selectively purify AMPA_Rs directly from brain tissue. I purified native AMPA_Rs from pig, sheep, cow, rat and mouse brains, determining that the purification efficiency was highest in rodents, and subsequently carried out single-particle cryo-

EM on hippocampal Ca²⁺-impermeable (CI) and cerebellar Ca²⁺-permeable (CP) antagonist-bound AMPARs from mouse brains.

The hippocampus is the nexus for memory storage and retrieval in the mammalian brain. Central to the function of the hippocampus are neuronal circuits in which the information processing is largely mediated by CI-AMPARs. I elucidated three distinct hippocampal CI-AMPAR assemblies, discovering the GluA2 subunit to exclusively occupy the gating-critical B/D positions of the receptor, suggesting that differential insertion of GluA1 or GluA3 subunits at the A/C positions is a mechanism of synaptic tuning. I revealed that the composition and assembly of auxiliary proteins is conserved for hippocampal receptors, in which TARP- γ 8 and CNIH2 occupy the B'/D' and the A'/C' positions, respectively. Finally, I defined the position of crucial residues that modulate the permeation and gating of the receptor, including RNA-editing-dependent amino acid variations.

The cerebellum is primarily responsible for regulating motor movement and balance control. In the cerebellum, GluA1-containing CP-AMPARs are involved in plasticity-dependent synaptic circuitry and complex motor behavior physiology. I elucidated structures of cerebellar CP-AMPAR receptors, discovering that these assemblies exhibit no apparent receptor subunit positional preference; permissive to both GluA1 and GluA4 at the gating-critical B/D positions, indicating non-conserved stoichiometry underlies synaptic signaling. Furthermore, cerebellar CP-AMPARs harbor a compact, asymmetric gate, an expanded LBD layer conformation, and a strikingly conformationally mobile ATD layer, atypical of antagonist-bound AMPARs, potentially underscoring a non-canonical gating mechanism.

Collectively, this dissertation defines an *in vivo* structural landscape of AMPARs with region-specificity.

Chapter 1

INTRODUCTION

Ligand-gated ion channels in the central nervous system

Our daily living processes require the precise interplay of cell-cell communication in the nervous system. A complex network consisting of billions of cells communicate in order to process and adapt to external sensory stimuli, while simultaneously maintaining and regulating our internal environment. Intercellular communication occurs primarily through chemical, electrical, or mechanical signaling mechanisms. Central to the molecular mechanism of chemical signaling are ligand-gated ion channels (LGICs), which are integral transmembrane proteins expressed on the cell surface that are activated by chemical messengers known as neurotransmitters.

LGICs underlie numerous physiological processes including memory storage¹⁻³, pain sensation⁴⁻⁶, and muscle contraction⁷⁻¹⁰ by converting chemical substances to electrical currents. They function as facilitators of diffusive ion transport across the lipid bilayer, generating transient electrical signals which in turn trigger downstream signaling events in the cell. Neurotransmitters, which comprise a diverse array of chemical substances including amino acids, nucleotides, peptides, and monoamines, are typically released from presynaptic cells, and diffuse across the synaptic cleft before binding to LGICs¹¹⁻¹³. These non-covalent interactions induce LGICs to undergo a conformational transition into a temporary ion-conducting state. In this ion-conducting state, Na⁺, K⁺, Ca²⁺, and/or Cl⁻ ions are permitted to permeate through the receptor channels and pass through post-synaptic membranes. Thus, the ionic influx can either be excitatory (depolarizing the membrane) or inhibitory (hyperpolarizing the membrane) to the cell, depending on the ion permeability of LGICs.

Evidence for the existence of LGICs surfaced in the early 1900's from T. R. Elliot who noticed that epinephrine is released by the nerve ending on each occasion when sympathetic nerve impulses are stimulated¹⁴, and also by R. S. Lillie who proposed that a transient change of passive ionic permeability across the cell membrane occurred as a result of a nerve signal¹⁵. At that time, LGICs remained enigmatic entities until direct evidence of their existence was made possible in the 1950s by Bernard Katz, who proposed the concept of ligand binding and channel

gating¹⁶. This was later followed by a landmark experiment performed by Neher and Sakmann who, by using single-channel recordings, demonstrated that LGICs were indeed ion channels activated by a ligand (in this study – acetylcholine) when they discovered discrete channel openings and closings when recording from frog nerve muscle fibers¹⁷. Progressively, our knowledge about LGICs expanded through the 1980s when cloning and sequencing methods enabled the first successful sequencing of a receptor subunit from a member of the LGIC family^{18,19}.

Following complete genomic and DNA sequencing analysis, LGICs can be sub-divided into three distinct superfamilies: Cys-loop receptors²⁰, ATP-gated receptors (P2XRs)²¹, and ionotropic glutamate receptors (iGluRs)²². The Cys-loop family constitutes the largest class of LGICs, which include the nicotinic acetylcholine receptor (nAChR), 5-hydroxytryptamine-3 receptors (5-HT₃R), γ -aminobutyric acid type A receptors (GABA_ARs), and glycine receptors (GlyRs). The nAChR and 5-HT₃Rs are excitatory while the GABA_AR and GlyR are inhibitory. These receptors are denoted as Cys-loop receptors due to the presence of an extracellular loop 13 residues long flanked by two cysteine residues connected by a disulfide bridge²³. Cys-loop LGICs are pentameric channels, consisting of five homologous subunits assembled around a central ion conducting pore. Each subunit harbors an extracellular domain (ECD) comprised of primarily β -sheets, a transmembrane domain (TMD) with four α -helices forming the ion channel, and a smaller intracellular domain (ICD)²⁴. The binding of a neurotransmitter at the interface of two subunits in the ECD induces a conformational rearrangement opening the receptor gate²⁵.

Purinergic (P2X) receptors are trimeric ATP-gated ion channels that are widely distributed throughout the nervous system. P2X receptors play physiological roles ranging from regulation of blood pressure²⁶ to modulation of synaptic transmission²⁷ and cardiac rhythm²⁸. P2X receptors are non-selective cation channels, forming both homomeric and heteromeric subtypes from seven subunit isoforms (P2X1-P2X7). All P2X subtypes share a common topology containing

intracellular termini, two transmembrane helices forming the ion channel, and a large extracellular domain containing the orthosteric ATP binding site²⁸.

Ionotropic glutamate receptors

iGluRs are a family of LGICs which open their ion-conducting pores in response to the agonist glutamate, the principal neurotransmitter at the majority of excitatory synapses in the central nervous system (CNS)²² (Fig. 1.1). Ionotropic glutamate receptors can be divided into three major subfamilies, denoted by their selective exogenous or synthetic agonists: kainate²⁹, N-methyl-D-aspartate (NMDA)³⁰, and α -amino-3-hydroxy-5-methyl-4-isoxazolepropionic acid (AMPA)³¹. These three classes of receptors all share a similar architecture, but have distinct functional, pharmacological, and structural properties. iGluRs assemble as tetramers, where each subunit adopts a layered architecture, distinct from Cys-loop and P2X receptors³². iGluR assembly is comprised of two extracellular domains – an amino-terminal domain (ATD)³³, which plays a fundamental role in subtype-specific receptor assembly^{34,35} and trafficking^{36,37}; as well as a ligand-binding domain (LBD) which is dedicated to agonist recognition^{38,39}. One of the major architectural features distinguishing iGluRs from the two other families of the LGICs is a domain responsible for agonist binding^{38,39}, whereas Cys-loop receptors and P2X receptors have agonist binding sites at subunit interfaces²⁵. The membrane-embedded transmembrane domain (TMD) forms the ion channel³² and a cytoplasmic C-terminal domain (CTD) participates in synaptic localization and trafficking⁴⁰.

Unlike their cognate iGluR family members, kainate receptors' primary functions remain elusive, as they only play a minor role in synaptic signaling. Kainate receptors have been reported to modulate pre-synaptic neurotransmitter release^{41,42}, enhance neuronal excitability^{43–45}, and participate in maturation of neuron circuits during development^{46,47}. Conversely, NMDA receptors (NMDARs) are ubiquitously expressed throughout the CNS, located at both presynaptic^{48–50} and postsynaptic sites^{51,52}, and are obligate heteromers. Functional NMDA receptors require

assembly with at least two GluN1 subunits⁵², along with simultaneous binding of glutamate and glycine for activation^{53,54}. NMDA receptor activation is particularly complex, as channel opening requires not only dual agonist binding, but also relief of endogenous Mg²⁺ binding in the pore⁵⁵. Due to voltage dependence of the extracellular block by Mg²⁺, NMDARs require membrane depolarization for cationic permeation^{56,57}. This depolarization is commonly provided by the fast activation of AMPARs⁵⁸, which mediate the majority of excitatory synaptic transmission in the mammalian brain.

AMPARs mediate excitatory synaptic transmission

Early investigations found glutamate to be at high concentrations in mammalian brains relative to other amino acids⁵⁹⁻⁶¹. Initially, this abundance was primarily attributed to enzymatic reactions related to metabolic functions in nerve tissue⁶². However, in the late 1950s, evidence emerged showing that glutamate is a chemical neurotransmitter when T. Hayashi revealed that application of glutamate into the motor cortex in dogs, monkeys, and humans generated clonic convulsions⁶³. Later studies discovered that glutamate induced muscle contraction in crustacean tissue⁶⁴ and excitatory action in spinal cord neuronal cells⁶⁵ supporting the notion that glutamate governed electrical signaling in the CNS. The most compelling evidence came from J. Raymond, A. Nieoullon, D. Dememes, and A. Sans through autoradiographic identification and biochemical characterization of glutamate uptake sites⁶⁶. These seminal studies crystallized the importance of glutamate for excitatory synaptic transmission and were the precursor for discovering one of the principle postsynaptic components responsible for the actions of glutamate in neurons – AMPA receptors⁶⁷. AMPARs primarily reside at the postsynaptic density of glutamatergic synapses⁶⁷, where binding of glutamate to their extracellular LBDs allows the influx of cations such as Na⁺ and Ca²⁺ through the channel pore^{68,69}, thus depolarizing the postsynaptic membrane and activating NMDA receptors. At normal membrane resting potentials, NMDA receptor channels are

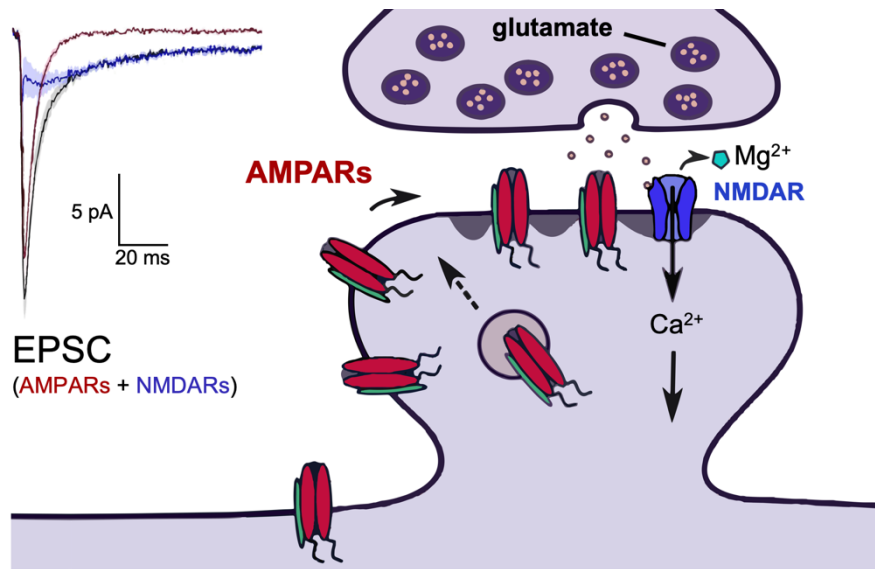


Figure 1.1. Schematic representation of a glutamatergic synapse. An illustration depicting a simplified excitatory synapse. Glutamate is released from presynaptic vesicles which diffuses across the synaptic cleft to activate AMPA receptors. As a result of AMPAR-mediated membrane depolarization, NMDA receptors are activated, collectively resulting in an excitatory postsynaptic current (EPSC) (inset). (Adapted from: Perszyk et al. 2016 [75]).

blocked by Mg²⁺ such that the initial charge flow through AMPARs results in a very rapid rising phase and rapid decay phase^{70,71}. However, in response to this initial depolarization, Mg²⁺ leaves the pore of NMDA receptors, permitting calcium conduction through their channels^{72,73}. Due to the intrinsic kinetics of AMPARs, the current through NMDA receptors has a slow rise and decay time^{70,73,74}. As a result, NMDARs contribute to the late, slow phase of the collective inward cationic current known as an EPSC, or excitatory postsynaptic current⁷⁵. (Fig. 1.1). Consequently, postsynaptic AMPARs are a key component governing the vast majority of excitatory synaptic transmission within the CNS, with their dysfunction implicated in the progression of numerous neurological conditions, including Alzheimer's disease⁷⁶⁻⁷⁸, motor neuron disease⁷⁹⁻⁸², and epilepsy^{81,83-85}.

The most notable role of AMPARs in the CNS is illustrated in the hippocampus, where changes in AMPAR-mediated activity are believed to form the molecular basis of learning and

memory⁸⁶⁻⁸⁸. Initial studies on the hippocampus spawned from a famous report⁸⁹ by William Beecher Scoville and Brenda Milner describing the results of surgical destruction of the hippocampi in an attempt to relieve epileptic seizures in Henry Molaison, known as "Patient H.M." The unexpected outcome of the surgery was severe anterograde and partial retrograde amnesia; Patient H.M. was unable to form new episodic memories after his surgery and could not remember any events that occurred just before his surgery, although he did retain memories of events that occurred many years earlier extending back into his childhood. From this seminal study, the hippocampus emerged as a structure crucial to memory formation^{86-88,90,91}. Indeed, initial studies on the hippocampus showed that high-frequency stimulation of the perforant path produces a long-term strengthening of the synaptic response⁹². This process, involving a prolonged strengthening of synapses that results in long-lasting increase of signal transmission between neurons is what is conventionally described as long-term potentiation (LTP)^{90,91,93}. By contrast, low-frequency stimulation was found to produce the opposite phenomenon: a long-term decrease in synaptic efficacy, deemed long term depression (LTD)^{90,94-96}. These early findings were the precursors to extensive research towards understanding the molecular basis of LTP and LTD. AMPARs have emerged as a central element of both LTP and LTD, and their role in these post-synaptic plasticity mechanisms has been extensively characterized.

Molecular architecture of AMPA receptors

In a study from 1984, mRNA was isolated from human fetal brain and "transplanted" into *Xenopus laevis* oocytes⁹⁷, showing that glutamate and kainate could induce currents from these cells. In light of this study, a cDNA library from brain mRNA was produced and GluR1, now known as the GluA1 AMPAR subunit, was identified⁹⁸. Following the identification of the GluA1 amino acid sequence, several other labs cloned and identified the remaining AMPAR subunits GluA2-4⁹⁹⁻¹⁰². These four pore-forming subunits, constitute the AMPAR iGluR subfamily, sharing ~70% overall sequence homology. GluA1-4 assemble into a tetrameric layered architecture made up of

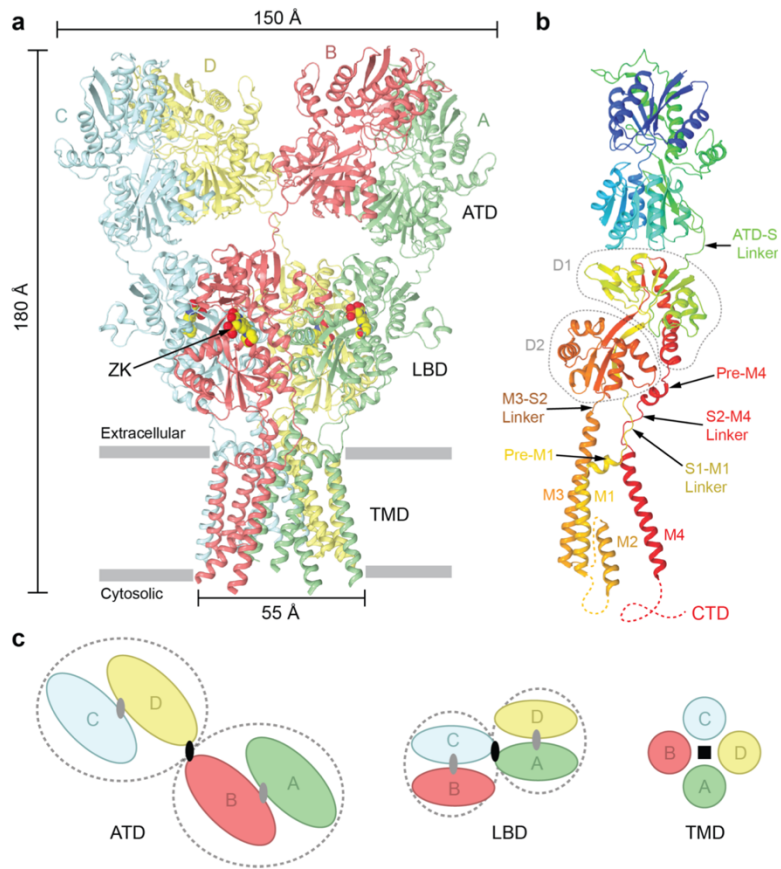


Figure 1.2. AMPAR architecture and domain arrangement. (a) Crystal structure of a homomeric AMPAR in the closed, antagonist-bound state (PDB: 3KG2) viewed parallel to the membrane. Each of the four GluA2 subunits are colored: green (A), red (B), blue (C) and yellow (D). (b) A single GluA2 subunit, rainbow-colored from blue (N-terminus) to red (C-terminus). The LBD upper (D1) and lower (D2) lobes are indicated by grey, dashed contours. (c) Top-down representations of each domain layer viewed parallel to the global axis of rotational symmetry. The axes of local two-fold symmetry in the ATD and LBD dimers are labeled with grey ovals. The axes of overall two-fold symmetry and local four-fold symmetry in the TMD are labeled with black ovals and a black square, respectively. Grey, dashed ovals encapsulate local dimer pairs in the ATD and LBD layers. (Reproduced from: Twomey et al. 2018 [153]).

the stratified ATD, LBD, TMD, and CTD layers (Fig. 1.2a,b). AMPA receptors form “Y-shaped” structures with overall two-fold symmetry in the absence of an agonist, a unique property for a tetrameric ion channel, which otherwise adopts four-fold symmetry. AMPA receptors form both homo- and heteromeric receptors, assembled from a combination of the GluA1-GluA4 subunits. The two extracellular layers – the ATD and LBD, form two pairs of dimers each and comprise the majority of the receptor mass (~75%)¹⁰³.

The primary structure of all AMPA receptor subunits begins with a signal peptide sequence which proceeds to encode the ATD layer; the most distal layer relative to the plasma membrane. The ATDs form quaternary structures in the shape of clamshells, consisting of two distinct lobes (R1 and R2) connected by three short loops, which dimerize through interactions at the R1 lobes³³ (Fig. 1.2c), and are posttranslationally modified by disulfide bonds and multiple N-linked glycosylation sites. The R2 lobes connect to the LBD layer via polypeptide linkers which extend towards the plasma membrane and are ~20 amino acids (aa) in length (Fig. 1.2a,b). The sequence and length of these linkers vary depending on the receptor subunit and allow for substantial mobility of the ATD layer relative to the LBDs.

Similar in modular shape to the ATDs, are the LBDs, which form a clamshell-shaped quaternary structures comprised of an upper (D1) and lower (D2) lobe (Fig. 1.2a,b). X-ray crystallography determined that the LBDs of adjacent subunits dimerize via the D1 lobes, with the agonist binding site located at the cleft between the D1 and D2 lobes³⁹. Agonist binding brings the D1 and D2 lobes closer together, which is commonly described as clamshell closure. Agonist efficacy correlates with the degree of clamshell closure, where stronger agonists, such as quisqualate induce greater clamshell closure¹⁰⁴, compared to weaker agonists, such as kainate³⁹. Clamshell closure facilitates gating of the channel pore by transducing mechanical force through the flexible polypeptide linkers S1-M1, M3-S2, and S2-M4. Alternative splicing of an exon encoding a region of the S2-M4 linker produces either “flip” or “flop” isoforms for all AMPAR subunits¹⁰⁵. Flop isoforms of GluA2-4 have faster desensitization kinetics than flip variants¹⁰⁵⁻¹¹⁰ and are conformationally heterogeneous³², likely owing to its glycine-rich sequence. Furthermore, the flip/flop region is immediately followed by an RNA editing site, known as the R/G site¹¹¹. The conversion of arginine to glutamine in flip/flop variants of GluA2-GluA4 results in slower desensitization kinetics. Collectively, the S1-M1, M3-S2, and S2-M4 linkers transduce conformational changes in the LBD to the TMD.

The TMD, reminiscent of potassium voltage-gated ion channels in an inverted rotation, is made up of three transmembrane helices (M1, M3, and M4) and an intracellular re-entrant loop (M2) between the M1 and M3 helices (Fig. 1.2a,b). While the LBD layer, under non-desensitized conditions is two-fold symmetric, the membrane-residing TMD adopts pseudo four-fold symmetry (Fig. 1.2c). The M3 segments extend out of the plasma membrane, forming a helical bundle crossing which constitutes the extracellular gate of the ion channel pore. Within the plasma membrane, the M1 and M4 helices peripherally surround the amphipathic segment of the M3 helices. The M2 re-entrant loop harbors an N-terminal helix and an extended C-terminal region, which lines the intracellular portion of the ion channel pore to form the selectivity filter. The M4 helix imparts stability to the receptor by inserting between the M1 and M3 of neighboring subunits, locking together the TMDs of individual subunits. Finally, extending intracellularly from the M4 helices is the carboxy-terminal domain (CTD), which varies in length between receptor subunits and splice variants. The CTD can be regulated by phosphorylation to influence retrograde trafficking^{112,113} and channel open probability¹¹⁴, however, a structural description of the CTD is unknown, as this region is inherently flexible and shows no secondary structure.

Biophysical properties of AMPARs: ion permeation, kinetics, gating cycle

The composition of AMPAR subunits within the receptor tetramer gives rise to distinct ion permeability^{69,102} and kinetic^{102,109,110} profiles. One of the functional hallmarks of AMPARs is how receptor subunit composition dictates cell excitability by gating the flow of cations into the cell. GluA2-containing AMPARs are nonselective for monovalent cations⁶⁹, where upon channel opening, K⁺ exits and Na⁺ enters the cell. The negative charge inside the cell, coupled with diminished intracellular concentration of sodium, drives sodium transport into the cell, whereas K⁺ follows its concentration gradient outside the cell. This ion transport mechanism is applicable to GluA2-containing AMPARs; however, in the absence of GluA2 within the receptor tetramer, ion permeation and channel conductance is profoundly different. AMPARs lacking the GluA2 subunit

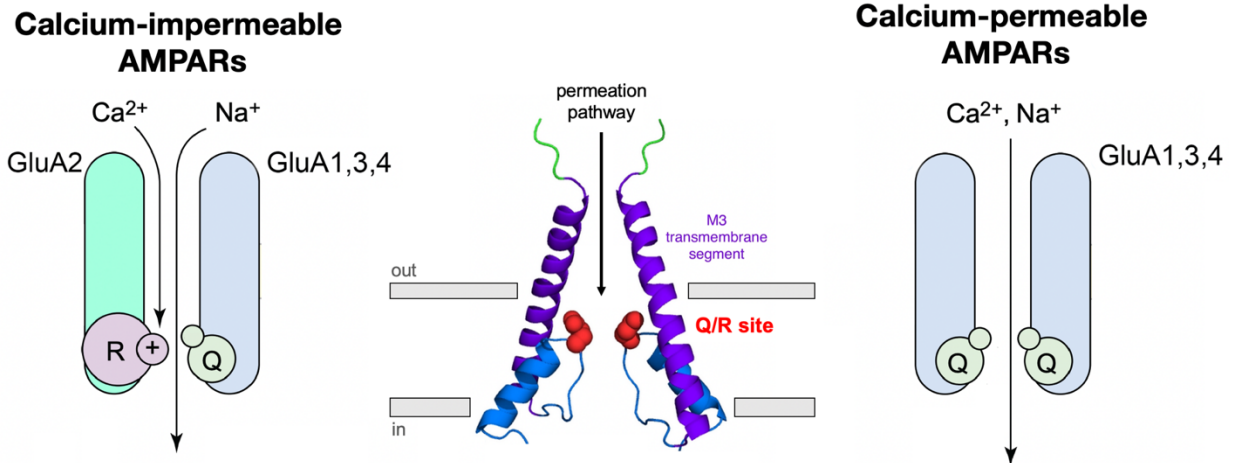


Figure 1.3. Ca^{2+} -permeability and the ion permeation pathway. The permeation pathway of AMPARs is defined by the M3 helices (purple) and the M2 pore loop (blue). At the apex of M2, resides the Q/R site (red), a key determinant of ion permeation. GluA2 is post-translationally edited from a genetically encoded glutamine to a positively charged arginine, rendering GluA2-containing AMPARs impermeable to calcium. For clarity, selected elements of the permeation pathway for only two subunits are shown. The initial segments of the M3-S2 linkers are colored green (Adapted from Wollmuth, 2015).

display faster kinetics^{115,116}, higher single-channel conductance^{115,116}, and permeability to Ca^{2+} ions^{69,115,116}. The overwhelming majority of AMPARs are GluA2-containing AMPARs^{117,118}, however, GluA2-lacking AMPAR expression is present in mature neurons^{119–123} and glia^{123–125}, and their expression dynamically regulated under basal, activated, and stressed conditions. While cells expressing GluA2-lacking AMPARs are predisposed to oxidative stress¹²⁶ and excitotoxicity¹²⁷, they play a significant role in motor coordination^{125,128}, synaptic plasticity^{129–132}, and fear erasure¹³³. Furthermore, during early postnatal development, expression of GluA2 is low compared to that of the other receptor subunits, which increases rapidly after the first postnatal week^{117,130}. This, coupled with the transiently high expression of GluA4¹³⁴, renders many neonatal AMPARs Ca^{2+} -permeable, suggesting that such calcium-permeable AMPARs may play a role in neonatal synaptic functions.

In the mature adult brain, diheteromeric GluA1/GluA2 and GluA2/GluA3^{118,135} receptors are the most abundant assemblies, whereas GluA4 expression is down-regulated¹¹⁷, representing

a switch in abundance of calcium-permeable AMPARs. Seminal proteomic studies have proposed that close to 80% of AMPA receptors in adult mammalian brains harbor the GluA2 subunit¹¹⁷, with notable abundant populations of GluA2-lacking AMPARs located primarily in the hippocampus^{129,131} and the cerebellum^{122,125,136}. These calcium-permeable receptors are expressed primarily in inhibitory interneurons, containing populations of GluA1 homomers¹³¹ and GluA1-GluA4 diheteromers¹²¹, in the hippocampus and cerebellum, respectively. How then, does GluA2 render AMPARs impermeable to calcium ions? Remarkably, GluA2 RNA is post-transcriptionally modified by editing a codon residing in the pore channel region that is converted from Gln607 to Arg607 (Q/R site) (Fig. 1.3). By virtue of Q/R site editing, located at the apex of the ion selectivity filter (Fig. 1.3), the permeation properties are altered: they have low permeability for divalent cations^{69,137}, are insensitive to the voltage-dependent block by endogenous polyamines¹³⁶, and have a low single-channel conductance^{115,119}. Conversely, GluA2-lacking AMPARs, have high permeability to Ca^{2+} ¹¹⁵, are blocked by endogenous polyamines^{138,139}, display inward rectification¹³⁹, and have higher single-channel conductance^{115,140}.

The ion permeation pathway is largely formed by the M3 transmembrane segment and the M2 pore loop (Fig. 1.3). The overall arrangement of these regions is reminiscent of K^+ -selective channels, but inverted such that the M2 pore loop is located towards the intracellular side of the membrane. The Q/R site is located at the apex of the M2 loop and contributes to the narrow constriction in the pore (Fig. 1.3), where hydrated permeant ions are stripped for recognition¹⁴¹. Computational modeling and functional studies have predicted that the organizing principles thought to govern selectivity are contingent upon the subunit-mediated electrostatic interactions of both the Q/R site components and cations, as unsolvated Na^+ and Ca^{2+} ions are comparable in size¹⁴¹⁻¹⁴³. Studies of native AMPARs have revealed that the incorporation of the GluA2 subunit in AMPARs, thus far, has been determined to preferentially occupy at minimum two positions – B/D^{144,145}. Under the assumption that calcium-impermeable AMPARs have two GluA2 subunits at the B/D positions, consequently, two Arg residues reside at the Q/R site, with

two Gln at the equivalent A/C subunit positions. This effectively renders two positive charges and two partial negative charges, arising from glutamines more electronegative side-chain oxygen atom in each of the A/C subunits. This difference in charge attractivity dictates ion selectivity between monovalent cations and calcium, presenting a high energy barrier and a molecular explanation why GluA2 renders receptors impermeable to calcium. Nonetheless, precise models for cation selectivity are absent, limiting a definitive mechanism of how the principles of charge and electromotive forces relegate receptors to different cationic permeability properties.

Gating and kinetics

The gating behavior of AMPARs is conventionally regarded as the series of conformational changes that occur upon ligand binding/unbinding to alter the functional state of the ion channel, whereas the kinetics of AMPARs describes the rate at which these gating processes occur. The kinetics of AMPARs occurs on a timescale of 10 milliseconds or less, which varies according to receptor subtype^{69,108}, RNA splicing and editing^{105,108}, post-translational modifications^{87,146}, and association with auxiliary proteins^{147–152}. The simplified kinetic model¹⁵³ begins with activation, followed by rapid desensitization, and then finally deactivation. These functional states occur in a stepwise manner, and have been characterized through X-ray structures^{154–157}, cryo-EM structures^{150,158–160}, and electrophysiological recordings^{106,111,115,153,161}, which have generated a wealth of mechanistic information of the basic gating and kinetic principles of AMPARs. However, one should exercise caution when interpreting kinetic models derived from these data, as they do not account for multiple sub-conductance levels or the flexible protein energy landscape.

Activation

In the absence of an agonist, the receptor resides in a closed, non-conducting state. Studies of conventional excitatory synapses have revealed that upon action-potential mediated presynaptic release, the concentration of glutamate in the synaptic cleft rapidly increases from

~20 nM to a physiological concentration of ~1 mM for <10 ms¹⁶². Neighboring neurons and glia then immediately uptake glutamate, rapidly returning the concentration of glutamate back to basal conditions. Consistent with these rapid release and uptake kinetics are the mechanisms of activation. Upon agonist binding, activation involves the receptor undergoing two sequential steps: clamshell closure of the LBDs^{68,150,159,163} and the activation gate opening. Glutamate binding results in a closed-cleft conformation stabilized by the formation of hydrogen bonds that involve amino acid side chains of residues in both the solvent-exposed regions of D1 and D2⁶⁸. The D2 lobe is directly connected to the M3 helix through the M3-S2 linker, which upon clamshell closure, triggers tension in this linker to mechanically pull open the channel gate^{150,159}. The channel gate is the extracellular entrance to the channel pore, comprised of the helical bundle crossing of the M3 segments. The gate opens by an outward translation away from the central axis, along with a rotation of the M3 helices along a hinge point at Ala621¹⁵⁰. Receptors display a single burst of channel opening, even with sustained agonist application, typically over a time course of a few milliseconds¹⁵³. These bursts can occupy one of four unitary subconductance levels, contingent upon subunit cooperativity and the complex relationship of agonist binding coupled to channel opening^{164–167}.

Desensitization

Immediately following activation is desensitization, the most energetically stable state, characterized by the loss of ion conduction despite the presence of an agonist. Desensitization occurs on the order of ms and results in ~90% decrease in current amplitude¹⁵⁵. Our understanding of the structural mechanisms underlying rapid desensitization has been exquisitely characterized through a broad range of structural studies using X-ray and cryo-EM of both isolated LBDs and full-length receptors, respectively, in combination with extensive physiological studies^{106,150,154,155,160,168–171}.

The first step of desensitization is the rearrangement of the D1-D1 dimer interface between LBDs of adjacent subunits. This idea was initially proposed through a seminal study which demonstrated that a single leucine to tyrosine substitution GluA2(L483Y), at the D1-D1 interface prevents desensitization almost entirely¹⁷². Leu483 is located in the dimer interface, and when mutated to tyrosine, promotes formation of additional interactions with residues located on the opposite LBD. The importance of this interface was later confirmed by X-ray crystallography of intact LBD dimers bound to cyclothiazide, an inhibitor of AMPA receptor desensitization¹⁵⁵. In each of these studies, both the mutation GluA2(L483Y) or cyclothiazide stabilized the dimer formation, providing the first evidence that stabilization of the LBD dimer interface can prevent desensitization. Further studies confirmed the importance of the dimer interface by mutating residues lining the dimer interface and observing changes in desensitization kinetics¹⁵⁴. More recently, cryo-EM structures have revealed that LBD dimers undergo dramatic rearrangement which include both a translation and a large rotation of the upper D1 lobes in each LBD dimer^{150,160,173}. As a result, the D1 lobes become largely separated, while the D2 portions remain connected to the ion channel at approximately the same spatial arrangement as in the closed state. This results in a loss of local two-fold rotational symmetry and the intradimer interface.

Deactivation

Lastly, to complete the full gating cycle, the receptor undergoes deactivation, which is characterized as a series of conformational changes that happen during recovery from desensitization back to the resting state¹⁵³. Upon recovery, the LBD clamshells reopen and release glutamate and the D1 lobes rotate back to restore the local two-fold rotational symmetry of the LBD dimers. Structural rearrangements describing these conformational changes are not yet available, as little is known about the potential asynchronous contribution of individual subunits, the order of LBD dimer interfaces reassembly, or the extent of opening to release glutamate.

AMPA assembly: subunit composition and auxiliary proteins

The subunit composition of AMPARs is developmentally regulated^{117,130,134,174}, region¹¹⁷ and cell type-specific^{175–177} and activity-dependent^{71,112,113,178}, leading to a diverse expression pattern of receptor subtypes. This diversity of positional occupancy of receptor subunits directly translates to differences in pharmacology^{22,120}, ion permeation¹¹⁰, gating and kinetics^{111,161}, and rectification^{119,139}. By solving the first full-length structure of an AMPAR, Sobolevsky, Rosconi and Gouaux established a universal framework describing subunit occupancy by defining the four receptor subunit positions as A-D³².

In the ATD layer, local dimers between subunits A-B and C-D form on each side of the overall central axis, with a cross-dimer interface between subunits B and D (Fig. 1.2c). In the LBD layer, the local dimer pairs are switched to A-D and B-C, with the cross-dimer interface formed between subunits A and C (Fig. 1.2c). As a result of this switch, there is swapping of domains between the ATD (AB and CD) and LBD (AD and BC) dimers. Therefore, AMPARs harbor two pairs of diagonally opposed subunits, referred to as A/C and B/D. Each pair is conformationally distinct: in the A/C pair, the LBDs are located closer to the channel pore, and denoted as “pore-proximal”, whereas the comparable B/D pair is denoted as “pore-distal” (Fig. 1.2a). Bridging the regions just above the M3 bundle crossing are three polypeptide linkers that resolve the symmetry mismatch between the LBDs and TMDs (Fig. 1.2a,b). The linkers that connect the M3 helices to the LBD exhibit greater structural change between the resting and activated states in the B/D chains, as opposed to the A/C chains. Thus, the assembly of these central elements of the gating machinery have significant functional implications.

AMPA assembly is established in the endoplasmic reticulum (ER)¹⁷⁹. The biogenesis of AMPARs relies on the individual subunit domains and auxiliary proteins to play critical roles in this process. A stepwise process was outlined by Schwenk and Fakler by employing co-expression of AMPARs with ER-interacting proteins, combined with native gel-electrophoresis and electrophysiological recordings¹⁸⁰. Throughout this “assembly line” process, GluA1–4

subunits pass through discrete stages where they assemble from monomers to tetramers. Biochemical experiments with isolated ATDs have shown that these proteins can self-assemble with varying degrees of affinity¹⁸¹, suggesting receptor subunit dimerization is most likely driven by high-affinity interactions of the ATDs. The second state of assembly proceeds to promote binding of the proteins FRRS1L (ferric chelate reductase 1-like) and CPT1c (carnitine palmitoyl-transferase 1C) to the receptor. Both FRRS1L and CPT1c are integral transmembrane proteins that promote stable binding. As a consequence, the two dimers are assembled together into dimers-of-dimers, thus forming the receptor tetramer. The final step of assembly occurs when postsynaptic auxiliary proteins replace FRRS1L and CPT1c. Dissociation of FRRS1L/CPT1c and binding of postsynaptic auxiliary proteins leads to the fully functional assembled receptor complex. How AMPARs exit from the ER still remains unknown, although it is well-established that auxiliary proteins, such as cornichons¹⁸² and TARPs¹⁸³ promote ER export.

Auxiliary proteins

AMPARs are subject to modulation by a variety of structurally diverse auxiliary proteins, defined as proteins unable to form ion channels alone, yet able to directly interact with a pore-forming receptor subunit (Fig. 1.4a,b). These functional interactions markedly influence receptor trafficking, gating, kinetics, and pharmacology. Indeed, the physiology of AMPAR relies on the interaction with auxiliary proteins. Across the CNS, over 30 different auxiliary proteins are known to co-assemble with AMPARs¹⁸⁴, typically binding to the transmembrane domain and decorating the periphery of the receptor. As such, many fundamental questions remain unanswered about the stoichiometry and molecular interactions of these auxiliary proteins with AMPARs, and importantly, how this translates to modulation of receptor function. Nevertheless, it is universally accepted that native AMPARs are multiprotein assemblies with diverse, complex physiology.

In 2000, Lu Chen and colleagues identified the first AMPAR auxiliary protein from experiments on the stargazer mouse, a mutant that lacks stargazin¹⁸⁵. These mice exhibited stark

thought to co-assemble with voltage-gated calcium channels, but Chen and co. observed that this mouse lacked excitatory transmission at glutamatergic cerebellar mossy fiber to granule cell synapses. Moreover, it was observed that cerebellar granule neurons contained intracellular AMPA receptors, but lacked AMPA receptors on the cell surface. Astonishingly, transfecting stargazin in *stg/stg* neurons restored AMPAR function, representing the first evidence that auxiliary proteins assemble with AMPARs to promote and anchor AMPARs at postsynaptic sites, through interaction with PSD-95. Taken together, this study established stargazin to have a direct interaction with AMPARs. The importance of this study cannot be understated, as it helped explain the discrepancy between the biophysical properties of native AMPARs that differed from studies of *in vitro* AMPARs, and fundamentally changed the understanding of AMPAR structure, physiology, and assembly. As a result, almost all AMPARs are considered multi-protein complexes, as they co-assemble with a constellation of transmembrane auxiliary proteins.

Following this discovery, stargazin, now conventionally referred to as TARP- γ 2, was later found to be part of an extended family of closely related proteins known as transmembrane AMPAR regulatory protein (TARPs), which are related in amino acid sequence to claudin¹⁸⁶, a four-helix transmembrane protein (Fig. 1.4b). TARPs are classified into Type I ($-\gamma$ 2, $-\gamma$ 3, $-\gamma$ 4, and $-\gamma$ 8) and Type II ($-\gamma$ 5 and $-\gamma$ 7) TARPs, based on differences in their amino acid sequence and functional properties¹⁵². TARPs were originally named “ γ -subunits” based on their sequence homology with the γ 1 calcium channel subunit¹⁸⁷, which is expressed only in skeletal and cardiac muscles and does not interact with AMPA receptors. The overall architecture of TARPs are similar to proteins of the claudin family, which are tetraspanin transmembrane proteins which regulate permeability of tight junctions¹⁸⁸. TARPs have four transmembrane helices, TM1-4, with an extracellular domain comprised of five beta-strands and four extracellular loops (Fig. 1.4b). TM3 also has a small extracellular loop, which connects to TM4. Importantly, Type I TARPs have a C-terminal tail of TM4 which extends into the cytosol harboring a PDZ binding motif, enabling TARPs to anchor AMPA receptor complexes to postsynaptic sites (Fig. 1.4b). Sequence comparison

between the two types of TARPs reveal that Type I TARPs have a larger extracellular domain compared to Type II TARPs, along with the canonical TTPV PSD-95 binding motif on their C-termini, which Type II TARPs do not contain. Furthermore, the most distinct functional difference between the two types of TARPs is that all Type I TARPs promote trafficking, whereas Type II TARPs do not¹⁸⁸. As is the case with AMPARs, the distribution of TARPs in the CNS is region-specific. For example, in the cerebral cortex, striatum, and hippocampus, γ -8 is differentially more abundant than any other TARP isoform^{117,189}, whereas in the brainstem, γ -2, -4, -7, and -8 are all equally abundant^{117,128,147,149,152}. Thus, it is hypothesized that regional differences in TARP abundance contributes to synapse-specific differences in EPSC kinetics^{148,151,152}.

The profound impact of the discovery of TARPs led to the exploration of additional auxiliary proteins which assemble with AMPARs. In 2012, a number of additional protein constituents were identified from a combinatorial proteomic approach of immunoprecipitation and mass spectrometric analysis¹⁸⁴. This study revealed different classes of auxiliary proteins, notably, cornichons, CKAMPS, GSG1L, and SynDIG1/4 (Fig. 1.4b). Cornichons are a class of transmembrane proteins, first characterized as cargo transporters, shuttling proteins from the ER through secretory endosomes¹⁹⁰. However, only in mammalian variants do cornichons maintain interaction with their cargo, in this case AMPARs, and remain co-assembled when reaching their final destination. There are four mammalian cornichon isoforms, cornichon-1-4, however, only cornichon-2 (CNIH2) and cornichon-3 (CNIH3) assemble with AMPARs to modulate the trafficking and channel kinetics of the receptor. Like TARPs, cornichons facilitate anterograde transport^{182,191}, slow desensitization and deactivation kinetics^{192,193}, and attenuate voltage-dependent polyamine block¹³⁸. Interestingly, although cornichons do not have an anchoring motif or signal peptide, both their N and C termini are extracellular¹⁹⁴, atypical for a membrane protein. The majority of cornichons' molecular mass is buried within the plasma membrane, with a tetraspanin-like topology, similar to TARPs (Fig. 1.4b). However, unlike TARPs, cornichons do not have a large extracellular domain, and moreover, TM2 in cornichons starts in the cytoplasm

but does not penetrate into the extracellular region. Instead, a loop extends from the middle of the end of TM2, and reenters the cytoplasmic region. This region is known as the cornichon-specific segment due to the sequence and topology disparity between the two families of proteins (Fig. 1.4b).

Cystine-knot AMPAR modulating proteins (CKAMPs) are proteins within the Shisa family of scaffold proteins¹⁹⁵, characterized by an N-terminal cysteine-rich and a C-terminal proline-rich region (Fig. 1.4b). CKAMP44 and CKAMP52 are the two most studied CKAMPs, both of which have cytosolic PDZ binding domains to anchor receptor complexes at postsynaptic membranes (Fig. 1.4b). CKAMP52 is found at a relatively lower abundance level than CKAMP44 in the CNS, although both proteins have lower abundance compared to TARPs and cornichons¹¹⁷. Germline-specific gene 1-like^{195,196} (GSG1L), like TARPs, belongs to the claudin superfamily of tetraspanin membrane proteins (Fig. 1.4b). However, unlike prototypical TARPs, GSG1L lacks a PDZ binding domain and imparts a negative influence to channel activity by reducing channel conductance and slowing the recovery from desensitization¹⁹⁶. Finally, SynDIG1/4, known as the proline-rich transmembrane proteins 1 and 2, are the lowest abundant auxiliary proteins compared to those described previously¹¹⁷, and promote synaptic localization¹⁹⁷⁻²⁰⁰ and slow desensitization kinetics^{198,201}.

It was initially presumed that one auxiliary protein associated with every pore-forming receptor subunit. However, an experimental approach which leveraged fluorescently tagged TARPs suggested a variable stoichiometry between 1-4 auxiliary proteins per receptor²⁰². The locations of these auxiliary protein binding sites were first proposed in 2012 by Jochen Schwenk, derived from a combination of proteomic, biochemical, and binding studies¹⁸⁴. Only in 2016 did cryo-EM analysis enable visualization of the first structures of AMPA receptors co-assembled with stargazin, supporting the variable assembly of 1, 2, or 4 TARPs per receptor^{158,203}. These structural studies relied on recombinant expression methods to resolve the architecture and arrangement of TARP γ -2 assembled with a homomeric GluA2 receptor. TARP γ -2 was observed

to surround the receptor transmembrane domain at four positions defined as A'-D' (Fig 1.4a). Following these preliminary structural studies, cryo-EM structures of AMPARs bound to cornichons¹⁹⁴, and GSG1L¹⁶⁰ emerged, further supporting these defined binding positions. The A'/C' positions reside beneath the LBD dimer, while the B'/D' sites reside beneath the dimer-dimer interface (Fig. 1.4a). Auxiliary proteins with a bulkier extracellular region such as TARPs and GSG1L, interact with the LBDs and seem to preferentially occupy the more sterically accessible B'/D' positions^{160,204}, whereas cornichons, which lack any extracellular elements, preferentially occupy the A'/C' positions^{145,163}, and primarily through the CNIH2/3 specific segment, modulate receptor function by interacting with the receptor M1-M2 loop^{145,163}. These distinctions in occupancy of the A'-D' positions are especially important, as positional arrangement of auxiliary proteins defines access to different parts of the gating machinery. Collectively, these studies provided an abundance of structural information about the arrangement of auxiliary proteins and their mechanisms of modulation. However, there remains uncertainty about the *in vivo* assembly and stoichiometry of auxiliary proteins, as many of these studies relied on engineered constructs and expression in heterologous cells.

Studying native AMPAR complexes: significance and approach

Appropriately interrogating the functional mechanisms of AMPARs relies on interpretation of their molecular structures. Over the past few decades, recombinant methodologies have contributed significantly to our structural understanding of AMPAR complexes. Yet, despite the wealth of knowledge gained from these seminal studies, there still remains a fundamental disconnect between these structures and *in vivo* AMPARs. At the onset of my dissertation, structural analysis of AMPARs was limited to GluA2 homomers co-assembled with a single auxiliary protein^{158,203}. While GluA2 homomers do exist *in vivo*¹⁴⁴, it is universally accepted that most native AMPARs are heteromeric and likely assemble with a constellation of auxiliary proteins, not just one^{117,135,144}. Moreover, these studies relied on artificial, engineered constructs,

which have difficulty replicating differential expression patterns of receptor subunits and auxiliary proteins.

One of the key features of AMPARs which enables distinct functional properties is their region-specific abundance profiles. Quantitative proteomics and single-molecule methods defined distinct abundance levels of AMPAR subunits and auxiliary proteins for all the major brain regions¹¹⁷. In the hippocampus, the GluA1 and GluA2 subunits exhibit high abundance, compared to GluA3 and GluA4. Additionally, compared to all the major auxiliary proteins (Fig. 1.4b), TARP- γ 8 and CNIH2 exhibit distinctly high abundance. Conversely, in the cerebellum, GluA1 and GluA4 are highly abundant compared to the GluA2 and GluA3 subunits. In contrast to the hippocampus, TARP- γ 2 and TARP- γ 7 are the most abundant auxiliary proteins in the cerebellum, compared to TARP- γ 8 and CNIH2. The absence of structures from these brain regions leaves many questions unanswered, namely: What is the subunit composition and auxiliary protein arrangement(s) of AMPARs in the hippocampus and cerebellum? And how can these structures inform us about gating mechanisms and synaptic signaling?

Several investigations over the past years have probed the assembly and composition of native AMPARs. Studies from Wenthold¹³⁵ and Lu²⁰⁵ have used single-cell genetics, immunocytochemistry, and immunoprecipitation to quantify the *in vivo* assembly of AMPARs. Jochen Schwenk and Bernd Fakler have designed elegant mass spectrometry experiments to quantify region-specific abundance of receptor subunits and auxiliary proteins in adult rats^{117,184}. Using negative staining microscopy, Teru Nakagawa and Tom Waltz provided the first glimpse of native AMPARs in 2005²⁰⁶. In this study Nakagawa and Walz successfully purified AMPARs from rat brains and decorated these purified receptors with subunit-specific and TARP-specific antibody fragments. While resolution limitations prevented elucidation of any secondary structure elements, this study was the first to employ antibody fragments for immunoaffinity purification and subunit-specific labeling for visualization of native AMPARs. Only in 2019, did Yan Zhao and

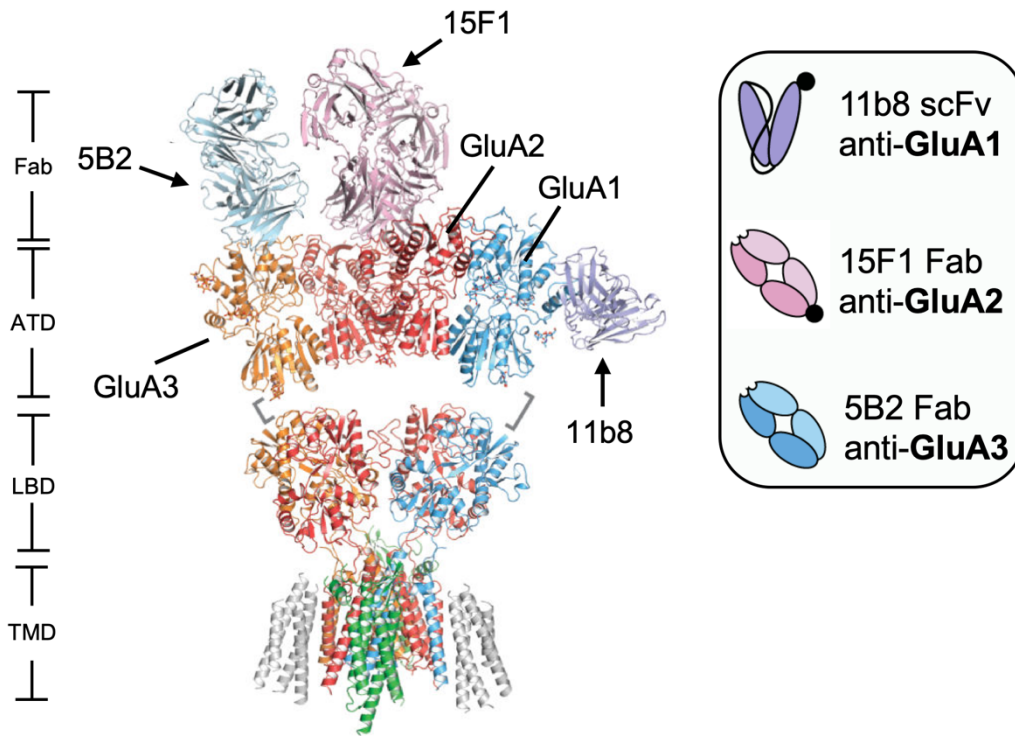


Figure 1.5. Subunit-specific labeling of native AMPARs using antibody fragments. The architecture of a native triheteromeric GluA1/GluA2/GluA3 receptor complex illustrates how subunit-specific labeling using antibody fragments distinguishes homologous receptor subunits. All three antibodies bind to epitopes on the ATD layer with nanomolar affinity to their respective receptor subunits. Auxiliary proteins are colored in green and grey. (Adapted from Zhao et al. 2019 [144]).

colleagues determine structures of native AMPAR assemblies with sufficient resolution to describe subunit composition, auxiliary protein assembly, and detailed molecular interactions¹⁴⁴.

To accomplish this, a former postdoc in the lab, Yan Zhao, developed an immunoaffinity purification strategy to isolate GluA2-containing AMPARs from brain tissue. By leveraging an engineered a twin-StreptII tag to an antibody fragment – 15F1¹⁷⁸, which exhibits sub-nanomolar specificity for GluA2 and no cross-reactivity against other receptor subunits, he was able to selectively purify GluA2-containing AMPARs directly from rat brains (Fig. 1.5). Additional antibody fragments, 11b8¹⁴⁴ and 5B2¹⁴⁴, were used to decorate the ATD layer of the receptor and label GluA1 and GluA3, respectively (Fig. 1.5). Remarkably, all three antibodies recognize conformational epitopes and display no cross-reactivity with the other receptor subunits. By

carrying out single-particle cryo-EM, Yan resolved 10 different receptor subtypes, defined by the tetrameric arrangement of receptor subunits. In addition, he also described the inter- and intradomain interfaces of the receptor subunits and showed how receptor subunit arrangement is not random, with the GluA2 subunit preferentially occupying the B/D positions, and the GluA1 and GluA3 subunits predominantly occupying the A/C positions. Lastly, he visualized distinct density features surrounding the receptor transmembrane domain, occupied by auxiliary proteins at the A'/C' and B'/D' positions, confirming these positions defined by previous recombinant structural studies.

My dissertation aims to build from this seminal work by employing single-particle cryo-EM to determine structures of hippocampal and cerebellar AMPARs. First, I have purified and biochemically compared AMPARs isolated from ungulate and rodent brains. Second, I have determined the architecture and assembly of three different hippocampal AMPAR assemblies. And third, I have detailed unique structural observations of cerebellar GluA1-containing Ca^{2+} -permeable AMPARs.

Prelude to the dissertation

The following chapters document my scientific journey during my doctoral studies. Chapter 2 highlights a purification strategy and biochemical comparison of AMPARs isolated from ungulate and rodent brains. I employed an immunoaffinity purification strategy to purify native AMPA receptor complexes from the brains of three different ungulate mammals – pigs, sheep, and cows. Biochemical comparison with rodent complexes demonstrated that structural determination of native AMPA receptors is achievable from a distinct clade of mammals with genetic and physiological traits closer to humans. Native AMPA receptor complexes from pigs, sheep, and cows displayed homogenous, monodisperse biochemical behavior, consistent with results from rodents. Furthermore, I highlighted species-dependent differences in molecular size and abundance, observing that native receptor complexes from sheep exhibit the greatest abundance

compared to the other four mammals, while the purification efficiency was the highest in rodents. This work provides the first biochemical analysis of pig, sheep, and cow variants of AMPARs, setting the stage for future cryo-EM studies.

Building from this, Chapter 3 details how we employed a similar method for AMPAR isolation, along with subunit-specific labeling using antibody fragments, to resolve three distinct AMPA receptor subtypes directly isolated from hippocampal tissue by a combination of single molecule methods – single particle cryo-EM and single molecule total internal reflection fluorescence microscopy. I determined multiple structures of heteromeric AMPA receptor complexes and the arrangement and interaction sites of the three most abundant auxiliary proteins – TARP- γ 8, CNIH2, and SynDIG4, all of which surround the receptor transmembrane domain at distinct binding sites. Furthermore, I have studied the TARP- γ 8 specific antagonist, JNJ-55511118¹⁸⁹, and have shown how this brain-region specific molecule binds to the receptor and antagonizes ion channel gating, not only defining the molecular pose of the small molecule, but also answering the long-standing mystery of why such small molecules incompletely antagonize receptor activity.

Chapter 4 explores the structural composition and assembly of a rare subtype of AMPARs – Ca²⁺-permeable AMPARs. I immunoaffinity purified antagonist-bound Ca²⁺-permeable AMPARs directly from mouse cerebella and discovered that the ATD dimers adopt a wide range of conformations which “splay outward” from the central axis, strikingly distinct compared to Ca²⁺-impermeable-AMPARs. I present five distinct GluA1-containing receptor assemblies, with GluA1 able to access each of the four A-D positions, including the gating-critical B/D positions. Finally, I highlight distinct changes in the M3 helices and M3-S2 linkers between our CP-AMPARs and previously solved CI-AMPARs, which are crucial elements of the receptor gating machinery linking agonist binding to channel gating. I describe a compact, asymmetric gate conformation along with interactions between the M3-S2 linkers, potentially underscoring a molecular basis for higher single-channel conductance and faster kinetics, emblematic of CP-AMPARs.

The results from this dissertation provide unique insight into the fundamental composition of native AMPA receptors, placing the molecular architecture of glutamate receptors on an unprecedented and accurate structural blueprint. Moreover, I believe that isolation and analysis of native receptor complexes provides an important, new direction to the structural biology field as a whole, showing how one elucidates the bona fide composition and structure of a brain region-specific receptor complex.

Chapter 2

IMMUNOAFFINITY PURIFICATION OF NATIVE AMPARS FROM MAMMALIAN BRAIN
TISSUE

Published content from: Rao P et al. (2023) Purification and biochemical analysis of native AMPA receptors from three different mammalian species. *PLOS One* 18(3):e0275351. doi: 10.1371/journal.pone.0275351.

RESEARCH ARTICLE

Purification and biochemical analysis of native AMPA receptors from three different mammalian species

Prashant Rao¹, Eric Gouaux^{1,2*}

1 Vollum Institute, Oregon Health & Science University, Portland, OR, United States of America, **2** Howard Hughes Medical Institute, Oregon Health and Science University, Portland, OR, United States of America

* gouauxe@ohsu.edu**OPEN ACCESS**

Citation: Rao P, Gouaux E (2023) Purification and biochemical analysis of native AMPA receptors from three different mammalian species. *PLoS ONE* 18(3): e0275351. <https://doi.org/10.1371/journal.pone.0275351>

Editor: Janesh Kumar, Centre for Cellular and Molecular Biology CSIR, INDIA

Received: September 13, 2022

Accepted: November 29, 2022

Published: March 17, 2023

Peer Review History: PLOS recognizes the benefits of transparency in the peer review process; therefore, we enable the publication of all of the content of peer review and author responses alongside final, published articles. The editorial history of this article is available here: <https://doi.org/10.1371/journal.pone.0275351>

Copyright: © 2023 Rao, Gouaux. This is an open access article distributed under the terms of the [Creative Commons Attribution License](https://creativecommons.org/licenses/by/4.0/), which permits unrestricted use, distribution, and reproduction in any medium, provided the original author and source are credited.

Data Availability Statement: All relevant data are within the manuscript and its [Supporting Information](#) files.

Funding: This work was supported by the National Institutes of Health (NINDS) grant 2R01NS038631

Abstract

The majority of fast, excitatory synaptic transmission in the central nervous system (CNS) is mediated by α -amino-3-hydroxy-5-methyl-4-isoxazolepropionic acid receptors (AMPA receptors), which are glutamate-activated ion channels integral to synaptic plasticity, motor coordination, learning, and memory. Native AMPARs are multiprotein assemblies comprised of a tetrameric receptor core that co-assembles with a broad range of peripheral auxiliary proteins which shape subcellular localization and signaling properties of the resulting complexes. Structure determination of AMPARs has traditionally relied on recombinant expression systems; however, these methods are not well suited to elucidate the diverse array of AMPAR assemblies that are differentially expressed in mammalian brains. While recent studies of native receptor complexes have advanced our understanding of endogenous assemblies, receptors thus far have only been isolated from rodent brain tissue. Here, we employed an immunoaffinity purification strategy to isolate native AMPARs from the brains of three different mammals—pigs, sheep, and cows. Compared to rodents, pigs, sheep, and cows are ungulate mammals, animals with closer genomic identity with humans. Here we determined the molecular size, overall yield, and purity of native AMPARs isolated from these three mammals, thereby demonstrating that structural determination and biochemical analysis is possible from a clade of mammals evolutionarily distinct from rodents.

Introduction

AMPA receptors (AMPA receptors), widely regarded as the primary mediators of fast synaptic transmission in the central nervous system (CNS), are ionotropic ion channels that translate chemical signals to electrical impulses. AMPARs are cation-selective receptor assemblies enriched at postsynaptic membranes that upon activation by glutamate, elicit local membrane depolarization [1]. AMPARs are ubiquitously expressed in the CNS and thus influence many pivotal excitatory signaling pathways, most notably those that underlie synaptic plasticity, motor coordination, learning, and memory [2–4].

AMPA receptors are tetramers assembled from four homologous subunits: GluA1–4 [5]. AMPARs are organized in a three-layered architecture comprising an amino-terminal domain

to Eric Gouaux and that Eric Gouaux is an investigator with the Howard Hughes Medical Institute (HHMI). The funders had no role in study design, data collection and analysis, decision to publish, or preparation of the manuscript.

Competing interests: The authors have declared that no competing interests exist.

(ATD) layer, which guides functional assembly and trafficking, a ligand binding domain (LBD) layer, which harbors the glutamate binding sites, and the membrane-embedded transmembrane domain (TMD) layer, which forms the non-selective, cation permeable ion channel pore [6]. In non-desensitized states, the extracellular ATD and LBD layers are each arranged as a dimer-of-dimers with local and overall two-fold rotational symmetry, making extensive subunit interactions that play critical roles in gating and assembly [6–9]. The subunit composition of AMPARs is remarkably variable, with distinct homomeric and heteromeric receptor assemblies expressed throughout the CNS [10–12]. This architectural heterogeneity underscores functional diversity, yielding ion channels with a wide range of gating kinetics [13, 14], pharmacology [15–19], and ion channel permeation properties [20–22]. Furthermore, AMPA receptors co-assemble with auxiliary proteins which decorate the periphery of the receptor, thereby influencing the assembly [23–26], trafficking [27–30], and kinetic properties [18, 30–32] of the receptor complexes. There are over 30 AMPAR auxiliary proteins, many of which exhibit a high degree of brain region specificity, further expanding the architectural and functional complexity of AMPAR assemblies [10].

Despite decades of structural studies describing the gating and kinetic properties of recombinant AMPARs [8, 33–35], visualizing the architecture and the molecular composition of native AMPAR assemblies has proven more challenging. Indeed, while heterologous expression systems [36, 37] have succeeded in overexpressing specific AMPAR complexes [8, 38, 39], often using covalent linkage to force auxiliary subunit position and stoichiometry [9, 34, 40], isolation of native receptors from brain tissue has shed light on the diverse ensemble of receptor assemblies, not only by defining subunit composition and arrangement, but also by mapping the auxiliary subunit type and position, as well as by suggesting the presence of previously unseen auxiliary subunits [12, 41]. Moreover, the diversity of brain region- and cell-specific composition of AMPA receptor subunits and auxiliary proteins has not yet been recapitulated in heterologous expression systems. Therefore, by extracting AMPARs directly from biological tissue we can authentically define the molecular composition and architecture of AMPARs.

In a recent study, an immunoaffinity purification strategy was developed to isolate AMPARs from rat brains by leveraging the 15F1 Fab, an anti-GluA2 antibody fragment [12]. These purified GluA2-containing receptors were subjected to cryo-EM analysis, which enabled visualization of the molecular composition, subunit arrangement, and architecture of an ensemble of native AMPAR assemblies [12]. Rodent variants have been used extensively not only for structural analysis but also for electrophysiology and binding assays, providing a consistent framework for the integration of structural and functional data into mechanistic schemes. Here, we demonstrate the isolation of native AMPARs from a different clade of mammals—ungulates. Consisting of primarily hoofed mammals, ungulates have genetic and physiological traits more similar to humans than rodents [42, 43], and present advantages as models for therapeutic and translational neurological research [44–46]. Exploiting the conserved epitope of the 15F1-Fab in ungulates, we were able to isolate native AMPARs from pig, sheep, and cow brain tissue. GFP fluorescence was used to follow AMPARs throughout the isolation process to determine and compare the purity, molecular size, and total yield from ungulates and rodents, altogether revealing that structural characterization and biochemical analysis of native AMPARs is feasible from ungulate mammals.

Results

Rodents and ungulates share a conserved 15F1 epitope

In mammalian brains, close to 80% of AMPARs are assembled with at least one GluA2 subunit [10]. Therefore, employing the 15F1 Fab for immunoaffinity purification enables the isolation

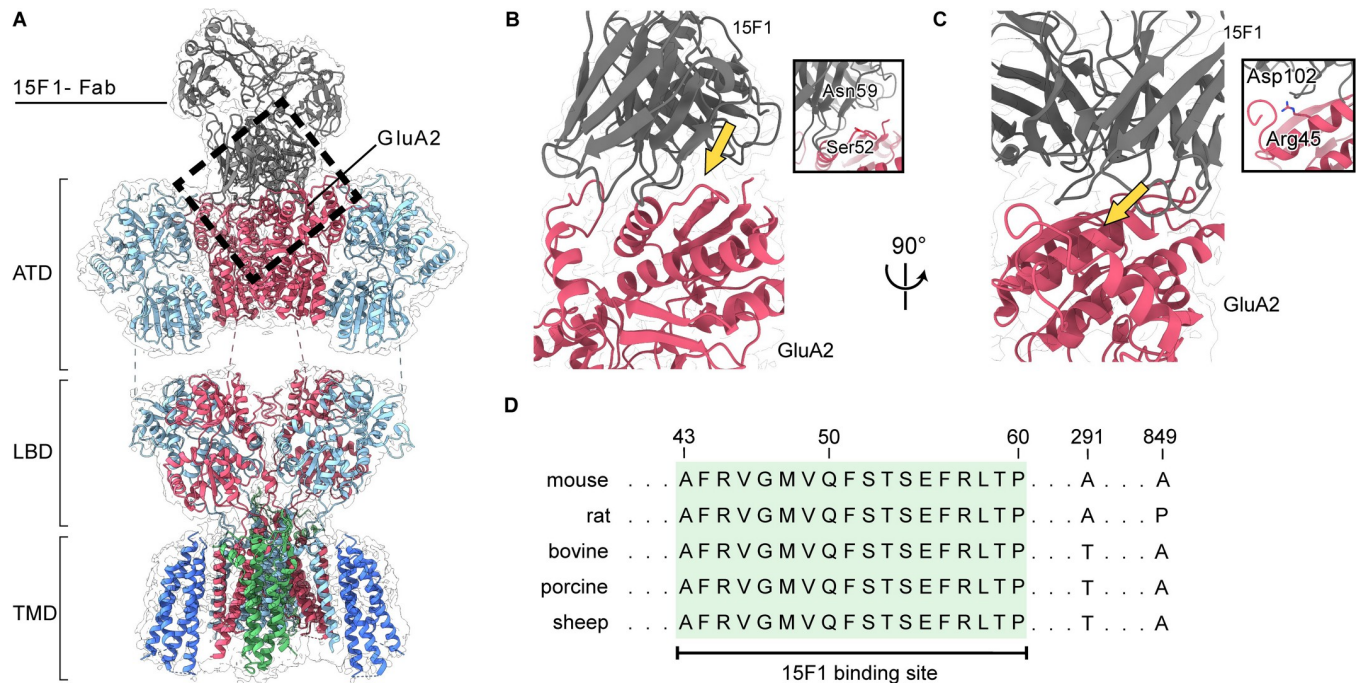


Fig 1. Conservation of the 15F1 Fab binding site. (A) Molecular model and cryo-EM map of the GluA1/GluA2 diheteromeric structure purified from mouse hippocampi (PDB: 7LDD) [41]. GluA1, GluA2, 15F1, TARP- γ 8, and CNIH2 are colored cyan, red, grey, green, and blue, respectively. The black dashed rectangle highlights the 15F1-Fab binding site on the ATD layer of GluA2. (B, C) Views of the interaction sites between 15F1 and GluA2. Insets: Close-up views of the regions indicated by the yellow arrows. (D) GluA2 sequence alignment of selected mammalian species. Conserved residues of the 15F1 binding region are highlighted in green. Unshaded residues denote sequence disparities between the selected mammals.

<https://doi.org/10.1371/journal.pone.0275351.g001>

of the major population of native AMPARs from whole brains. With rodent variants, 15F1 displays sub-nanomolar affinity for GluA2 and has no detectable cross-reactivity with the other AMPA receptor subunits [12]; however, it was unclear if these binding properties would be preserved in AMPARs from pigs, sheep, and cows. To identify the 15F1 epitope, we carefully examined the previously solved rodent AMPAR structures and found that the structural resolution of the 15F1-receptor binding region was the highest from the hippocampal GluA1/GluA2 diheteromeric complex (PDB: 7LDD) [41]. Inspection of the hippocampal GluA1/GluA2 structure permitted us to definitively map the binding region of 15F1 to the periphery of the ATD layer, encompassed by residues Ala43–Pro60, where we observe the C α atoms from the variable loops of 15F1 within ~4–5 Å of the side chains on the upper lobe of the GluA2 ATD clamshell (Fig 1A). We denote a possible hydrogen bond interaction between Ser52 on the ATD layer with Asn59 of the 15F1 variable loop (Fig 1B), along with a possible electrostatic interaction between Arg46 of GluA2 and Asp102 of 15F1 (Fig 1C), both of which appear to be important interaction sites. However, due to insufficient resolution of the 15F1 Fab region of the density map, we cannot conclusively define these potential contacts. Nevertheless, the rodent sequences of the 15F1 epitope were compared to those of pigs, sheep, and cows, all of which exhibited complete sequence conservation (Fig 1D), indicating that an immunoaffinity purification strategy of GluA2-containing AMPAR complexes using the 15F1 Fab would likely be feasible from these mammals. Notably, the 15F1 epitope is also conserved in humans, but obtaining non-chemically treated brain tissue proved to be challenging. Before attempting our purification strategy, we modified the 15F1-Fab DNA coding sequence by cloning a GFP tag between the twin-Strep tag and the C-terminus of the heavy chain and

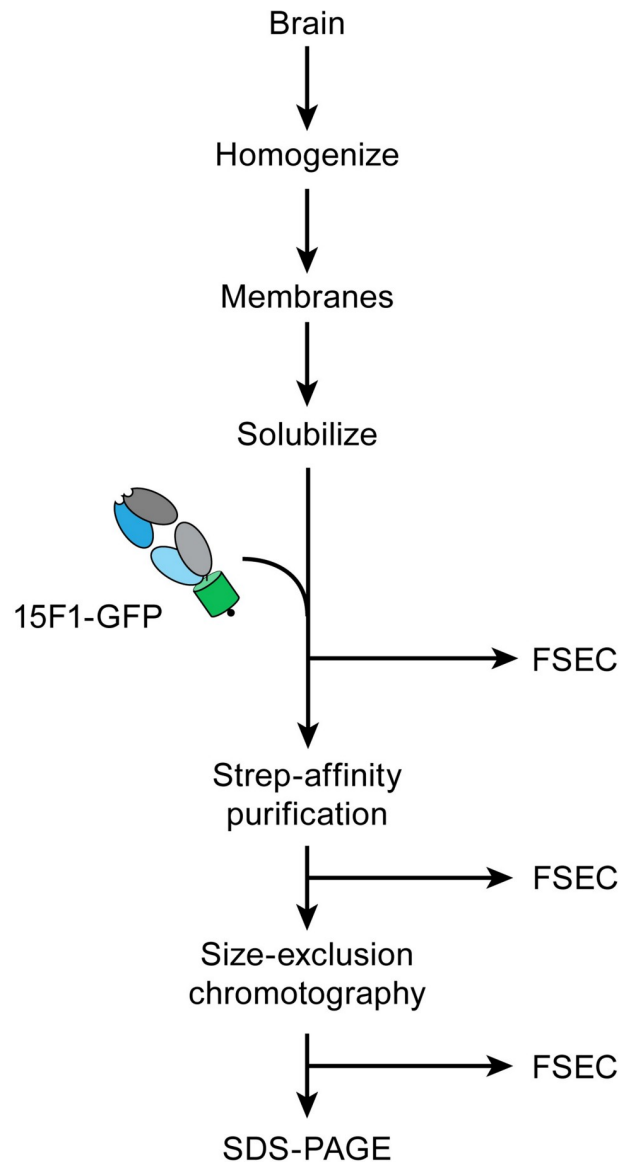


Fig 2. Immunoaffinity purification workflow. The outline of the immunoaffinity purification strategy. After membrane solubilization, FSEC analysis was performed at each step.

<https://doi.org/10.1371/journal.pone.0275351.g002>

expressed this antibody in SF9 insect cells using baculovirus expression. This modification enabled us to follow AMPARs throughout the purification process using GFP fluorescence.

Brain acquisition and membrane preparation

Using the engineered Fab, denoted 15F1-GFP, we performed identical immunoaffinity purification workflows for both rodents and ungulates (Fig 2), consistent with previous studies demonstrating isolation of native AMPARs from brain tissue [12, 41]. First, we acquired rodent and sheep brain tissue donated by neighboring researchers at OHSU. Procuring cow and pig brains proved to be more challenging, as we were unable to find any labs nearby which used these animal models. However, we inquired with commercial vendors and found that many slaughterhouses discard animal heads. Therefore, we purchased pig and cow brains from local

sources that were willing to remove whole brains from adult animal carcasses. With these whole brains in hand, we focused our efforts on brain homogenization and membrane preparation.

In light of the difference in mass of more than two orders of magnitude between rodent and ungulate brains (Table 1), we adopted two different strategies for homogenization. Prior to sonication, rodent brains were homogenized using a conventional, hand-held Dounce-homogenizer, whereas ungulate brains, due to their substantially larger mass, required more vigorous homogenization with a large blender. Post-homogenization, membranes were prepared using a two-step centrifugation strategy consisting of a low-speed 5000 x g spin, followed by an ultracentrifugation step at 150,000 x g. The low-speed centrifugation step was implemented to first pellet insoluble tissue and cell debris. With ungulate brains, we found the majority of the brain homogenate to pellet during this step. Recovering AMPARs from this material, however, required solubilization under harsh conditions with ionic detergents, thus disrupting the native structure and likely promoting denaturation of the receptor complexes. Next, the supernatant was subjected to ultracentrifugation which pelleted the membranes. We measured the mass of membranes for each mammal (Table 1), before resuspending them in homogenization buffer.

Detection of native AMPARs using 15F1-GFP

Solubilization of membranes using detergent is an effective approach to extract membrane proteins from the lipid bilayer [47]. We elected to use digitonin as it is capable of efficiently extracting and preserving the structural integrity of AMPARs, while also retaining co-assembled AMPAR auxiliary proteins [8, 12, 39, 41, 48]. To assess if brain size correlates with AMPAR abundance, we first solubilized equal masses of membranes from each mammal in 2% digitonin (w/v) and incubated this material with 15F1-GFP. Using fluorescence-size exclusion chromatography (FSEC) [49], we observed distinct peaks corresponding to GluA2-containing AMPARs based on GFP fluorescence and elution time (Fig 3A). We compared the peak heights of all five mammals and found that sheep and pigs exhibited the highest abundance of AMPARs, and surprisingly, we observed that cows display the lowest abundance. This discrepancy in molecular abundance was unexpected considering sheep, pigs, and cows have similar brain masses and are from the same clade of mammals. However, we are cautious not to overinterpret these FSEC profiles, as estimating abundance from solubilization of membrane pellets is challenging, due to the technical difficulty of weighing wet membranes. Nevertheless, the reason for this disparity remains unclear, although we speculate it could be due to the incidental removal of AMPARs in the first centrifugation step during membrane preparation.

Post-solubilization, we also observed that sheep AMPARs elute earlier than the other four mammalian receptor variants (Fig 3A), which we estimate corresponds to a larger molecular

Table 1. Quantification of AMPARs and brain tissue amongst different species.

	Brain mass (g)	Mass of membranes (g)	Mass of purified AMPAR complexes (μg)	Receptor/brain tissue % ($\times 10^{-8}$)	Receptor/membrane % ($\times 10^{-7}$)	Molecular weight: Solubilization (kDa)	Molecular weight: SEC-purified (kDa)	Molar quantity (picomoles)
Cow	281	20.9	7.0	2.5	3.4	830	802	8.7
Sheep	98	15	19.7	20	13.1	850	841	23.4
Pig	109.8	4.6	13.7	12	29.8	832	830	16.5
Rat	1.7	0.5	2.1	124	42	827	811	2.6
Mouse	0.6	0.3	0.5	83	17	839	837	0.6

<https://doi.org/10.1371/journal.pone.0275351.t001>

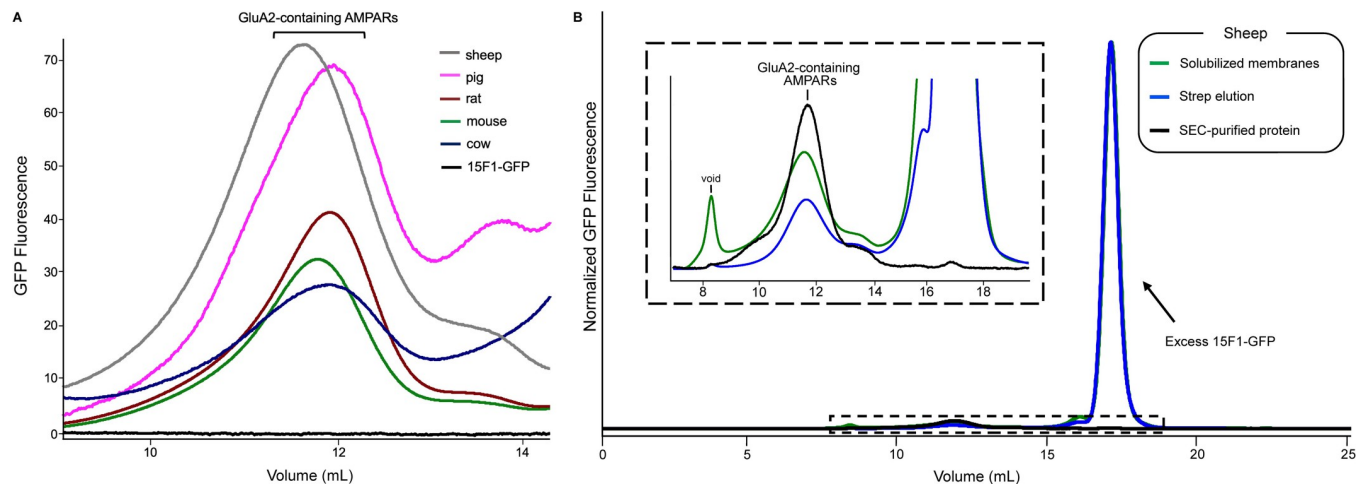


Fig 3. Solubilization and immunoaffinity purification. (A) Cross-species comparison of GluA2 elution position and abundance. The 15F1-GFP Fab was added to digitonin-solubilized membranes and the resulting samples were analyzed by FSEC. All traces were from equal masses of membranes. (B) FSEC traces of native sheep AMPARs analyzed throughout the immunoaffinity purification process using GFP fluorescence. Inset: Magnified view highlighting the peaks corresponding to native sheep AMPARs outlined by the dashed rectangular box.

<https://doi.org/10.1371/journal.pone.0275351.g003>

size of 11–23 kDa (Table 1). This raises the possibility that variability in receptor and/or auxiliary subunit composition between these species account for this divergence. High-resolution proteomic analysis from rat brains has previously determined abundance profiles of auxiliary proteins that co-assemble with native AMPARs [10, 11]. The most abundant co-assembled constituents are transmembrane AMPAR regulatory proteins (TARPs), cornichons, and ferric chelate reductase 1 like protein (FRSS1L) [10], all of which bind to the receptor, largely via the transmembrane domain, and have well-described functional properties that include modulation of gating [18, 30, 32], regulation of surface trafficking [24, 26, 28, 30], and modification of pharmacology [50–52]. We compared the sequences of these auxiliary proteins from all five mammals to determine if the sheep variants have a larger predicted molecular size. The amino acid sequences were nearly identical for almost all TARPs and cornichons, although we found an additional 10, 13, 13, and 15 amino acid (aa) appendage to the N-terminal domain of the TARP- γ 8 sheep variant compared to cows, pigs, mice, and rats, respectively (S1A Fig in S1 File). The cornichon-2 variant in cows differed from all other variants with a 15 aa N-terminal sequence addition. A comparison of the FRSS1L variants revealed a 49, 49, and 58 aa addition in the sequence of the sheep variant compared to rodents, pigs, and cows, respectively (S1B Fig in S1 File). Moreover, previous studies have shown that FRSS1L and TARP- γ 8 bind in two-fold arrangements to separate AMPARs populations [24, 41], diminishing the possibility of combined assembly with the same receptor. Therefore, the amino acid extensions of both the TARP- γ 8 and FRSS1L sheep variants appear insufficient to be solely responsible for the estimated differences in size.

To examine if the difference in molecular size was contingent upon the architectural variance of the receptor tetramer, we directly compared the sequences of the AMPAR subunits between all the five mammals. Sequence identity was high between receptor subunits from the different species; however, we noted several differences in predicted glycosylation sites. Sheep have more predicted O- or N-linked glycosylation sites than rodent variants for the GluA1, GluA3, and GluA4 subunits, 1, 4, and 4 more respectively. For the GluA2 subunit, the rodent variant has 1 more predicted glycan than the sheep variant. Predicting how these differences in post-translational modifications will affect the sizes of various heteromeric receptor assemblies presents a challenge, but we surmise that the variability of glycosylation contributes to the

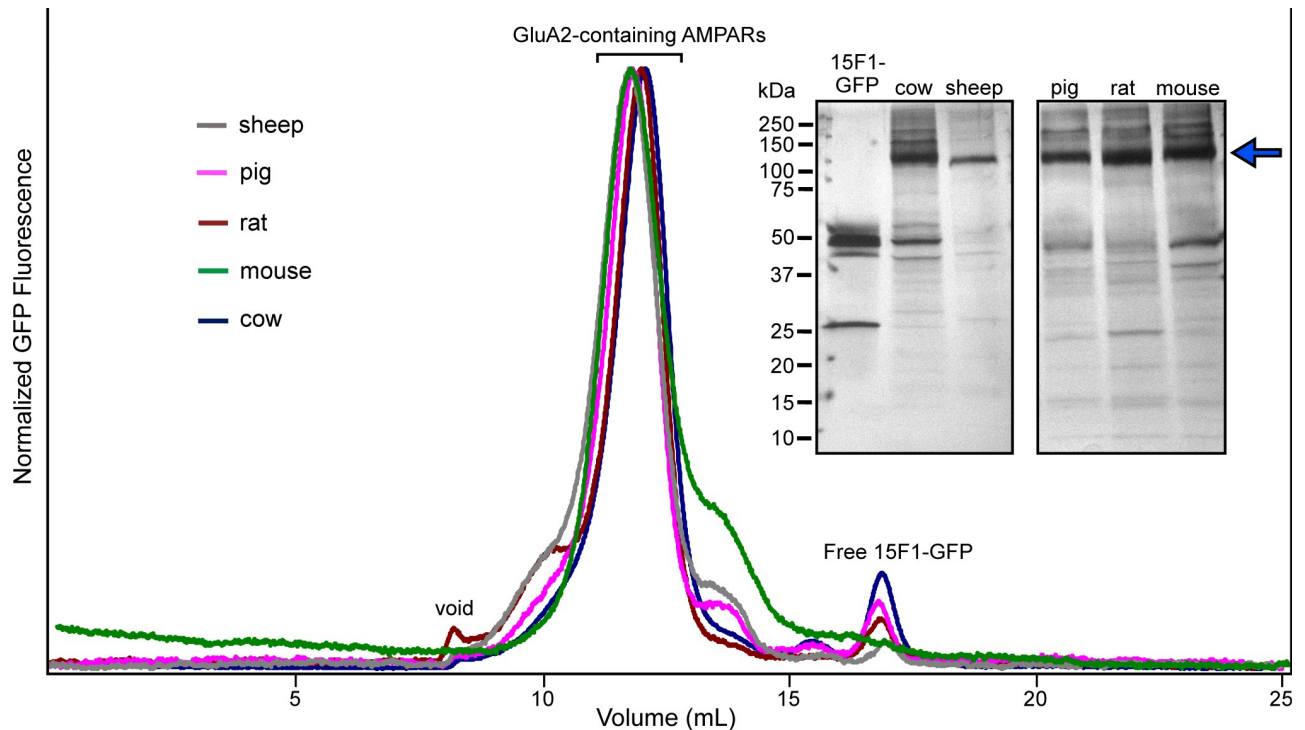


Fig 4. Analysis of purified native AMPARs. Overlaid FSEC profiles of 15F1 Fab-purified AMPAR assemblies from the five mammals. Inset: Silver-stained, SDS-PAGE analysis of purified receptors. The blue arrow indicates the migration position of the majority of the AMPAR subunits. The samples were run on two different gels and positioned adjacent to each other for clarity.

<https://doi.org/10.1371/journal.pone.0275351.g004>

discrepancies in molecular size. Furthermore, we cannot rule out the possibility that differential assembly associated with auxiliary proteins may also be a contributing factor.

Immunoaffinity purification workflow and analysis

To purify native AMPARs, we first solubilized membranes amassed from a single brain of each animal and individually incubated the digitonin-solubilized suspensions with the 15F1-GFP Fab. We immobilized 15F1-GFP-bound AMPARs to Streptactin resin using the twin StrepII tag encoded on the C-terminal region of 15F1 and released 15F1-GFP Fab by incubating the resin with d-desthiobiotin. Size-exclusion chromatography was used to separate native AMPARs from excess 15F1-GFP Fab (Fig 3B, S2 Fig in S1 File), and we determined the purity and overall yields of the different populations of native AMPARs. For all five mammals, we isolated native AMPAR complexes in the picomole (pmol) range, sufficient for biochemical, mass spectrometric, and cryo-EM analysis [53, 54]. We purified the highest amount, about 23 pmol, from sheep, and the smallest amount—0.6 pmol from mice. We observed homogeneous FSEC profiles from all five mammals that eluted at approximately similar positions (Fig 4). SDS-PAGE analysis of the purified samples corroborated our FSEC results, as we found the most prominent bands for all species to correspond to AMPAR subunits (Fig 4). We observed additional, undetermined bands, migrating from 15–55 kDa, which we attribute to co-purified auxiliary proteins (Fig 4).

Discussion

Strategies to purify membrane proteins from native sources have re-emerged as a subject of considerable attention in the structural biology community. The first membrane protein

structures solved from bacteria, mitochondria, and chloroplasts relied on native purification methods [55–57]. However, these strategies were limited to targets with uniquely high endogenous abundance. The advent of purification tags, along with powerful sequencing and cloning methods stimulated rapid progress in using heterologous expression methods to facilitate structural studies of a wide range of membrane proteins, and also the generation of elegant methods for interrogating their functional properties. Recently, a resurgence of improved native membrane protein purification methods has provided unprecedented insight into molecular architecture, novel protein-protein interactions, and functional mechanisms, previously unattainable by conventional recombinant methods. Isolation of native AMPARs from rodent brain tissue using the 15F1 Fab, in particular, has led to unique insights into the structural assembly and region-specific molecular pharmacology. Immunoaffinity purification and cryo-EM analysis of AMPARs from rat brains defined the stoichiometry and arrangement of a spectrum of AMPARs, including a triheteromeric GluA1/GluA2/GluA3 assembly, which was previously unknown [12]. A subsequent study used single-molecule methods to define the unique auxiliary protein stoichiometry of mouse hippocampal AMPARs and how a forebrain-specific molecule, JNJ-55511118, binds to native AMPARs and antagonizes ion channel gating [41].

In the present study, we exploited the 15F1 Fab to purify native AMPARs from cow, sheep, pig, rat, and mouse brains. Modification of the 15F1 antibody to include a covalently attached fluorophore allowed us to follow receptors throughout our purification workflow and demonstrated a commensurate strategy for isolating native AMPARs from two distinct mammalian clades. Surprisingly, we were able to purify more AMPAR assemblies per unit of brain mass from rodents, compared to the larger mammals from the ungulate clade. This purification efficiency of native rodent AMPARs was considerably higher than pigs, cows, and sheep, as the purified molar quantities from these three species were only ~15–40x and ~3–10x compared to mice and rats, respectively, even though ungulate brains have ~100x the mass of rodent brains. Whether this purification inefficiency is unique to ungulates or simply a consequence of their brain tissue composition, remains an open question. Repeating the immunoaffinity purification workflow with multiple brains from each mammal, under careful consideration of variables such as age and sex, will allow for precise interpretation of the observations we describe here. However, despite the unexpectedly lower purification efficiency, we successfully purified pmols of native AMPAR assemblies from pigs, sheep, and cow brains, a quantity sufficient for cryo-EM, biochemical, and mass spectrometric analysis. Recent studies have demonstrated the feasibility of structural studies of native membrane protein complexes [58, 59] from pmol of purified protein [58, 59].

The disparity of AMPAR abundance and molecular size between native cow and sheep AMPARs is unresolved. Whereas native pig and sheep AMPARs seem to be relatively equivalent in purity, abundance, and molecular size, native cow AMPARs display markedly lower abundance, molecular size, and purification efficiency. The possibility remains that cow brains could simply be inherently less amenable to our immunoaffinity purification strategy due to the tissue composition of their brains. Conversely, native sheep AMPARs display the highest abundance and purification efficiency compared to pig and cow AMPARs, indicating that sheep are the favorable ungulate species for structural investigations of native AMPAR assemblies.

The immunoaffinity purification methodology we outlined offers avenues for adaptation, which we presume can lead to deeper insight into native AMPAR assemblies. For example, one could apply this methodology to evaluate age-dependent associated changes of AMPARs. Prior studies in mice have suggested that distinct populations of AMPAR complexes exist in the early postnatal period, compared to adulthood [10, 60]. Resolving the architecture and

molecular composition of native AMPARs from different developmental phases offers the opportunity to shed light on the structural dynamics of AMPAR assembly. In addition, during the homogenization step we described earlier, one can introduce sedimentation and sucrose gradient centrifugation to isolate specific sub-cellular fractions such as endoplasmic reticulum (ER) membranes. AMPARs poised for anterograde trafficking at the ER have yet to be visualized and are anticipated to co-assemble with a set of architecturally distinct auxiliary proteins compared to synaptic AMPARs [24]. Furthermore, provided one has an antibody with high-affinity and specificity for a non-GluA2 AMPAR subunit, one can isolate specific heteromeric assemblies by incorporating an additional antibody affinity purification step prior to SEC. We anticipate that this purification workflow will serve as a starting point for future studies and lead to the expansion of animal models used to characterize native AMPARs.

Materials and methods

Ethics statement

We did not perform any experimental manipulations on live animals. We did not perform any euthanasia, anesthesia, or any animal sacrifice in this study. Pig and cow brains were obtained directly from commercial sources. Sheep and rodent brains were dissected from donated animal carcasses, euthanized prior to our acquisition.

Expression and purification of 15F1-GFP

As previously described [41], the DNA sequences encoding the Fab domains of the light and heavy chains from the 15F1 monoclonal antibody were cloned into a bicistronic pFastBac1 vector for baculovirus expression in Sf9 insect cells, with the following modifications. The GP64 signal peptide (MVSAIVLYVLLAAAAHSAFA) was included at the N terminus of the heavy and light chains, whereas an eGFP tag, followed by a twin-Strep II tag, were introduced at the C terminus of the heavy chain. Insect cells were transduced with baculovirus and cultured at 27°C. After 96 hrs, the supernatant was collected and the pH was adjusted to 8.0, followed by clarification at 10,000 x g for 20 min at 4°C. The supernatant was concentrated by tangential flow filtration using a 50-kDa molecular-mass cut-off filter and dialyzed against TBS buffer (20 mM Tris, pH 8.0, 150 mM NaCl) for 36 hrs. Strep-Tactin affinity chromatography was used to isolate the 15F1-GFP Fab, which was further purified by SEC in the presence of TBS buffer. Peak fractions were pooled and stored at -80°C. Concentrated 15F1-GFP was used for purification and FSEC experiments.

Ungulate brain tissue homogenization

Pig (age: ~1 year) and cow (age: ~2.5 years) brains were purchased directly from Tails & Trotters (Portland, OR) and Carlton Farms (Carlton, OR), respectively, and stored on ice during the drive back to the lab (15 min– 1.5 hr). Sheep (ewe, age: ~1.5 years) brains were kindly donated by Dr. Charles Roselli (OHSU). We scheduled brain dissections at least two weeks in advance, coordinating with the vendors and Dr. Roselli on a specified time to pick up brains. All ungulate brains were dissected from animal heads within 20 min and immediately placed on ice. Upon arrival to the lab, brains were washed with ice-cold PBS, before being placed in homogenization buffer (TBS + 0.8 μM aprotinin, 2 μg ml⁻¹ leupeptin, 2 mM pepstain A, 1 mM phenylmethylsulfonyl fluoride) with all subsequent steps performed at 4°C. Brains were blended in an Oster blender for 2 min with homogenization buffer. The blended material was sonicated for 1.5 min, 3 sec ON, 5 sec OFF, power= 4.0, and the homogenate was centrifuged at 5000 x g for 15 min. Next, the supernatant was decanted and subjected to ultracentrifugation

at 150,000 $\times g$ for 1 hr to pellet the membranes. Membranes were resuspended in TBS + 1 μM (R,R)-2b (N,N'-[biphenyl-4,4'-Diyl]dipropylpropane-2,1-Diyl]dipropylpropane-2-Sulfonamide) + 1 μM MPQX ([3,4-dihydro-7-(4-morpholinyl)-2,3-dioxo-6-(trifluoromethyl)-1(2H)-quinoxaliny]methyl]phosphonic acid) + 10% glycerol.

Rodent brain tissue homogenization

From donated rat (adult Sprague Dawley) and mouse (28–40 days, C57BL/6) carcasses, whole brains were first dissected, washed with PBS, and placed carefully in ice-cold homogenization buffer. Brains were homogenized using a Teflon-glass grinder and further disrupted using a sonicator for 5 min with cycles of 3 sec on and 6 s off, at medium power, on ice. The homogenate was subjected to centrifugation at 5000 $\times g$ for 15 min. The membrane fraction was collected by ultracentrifugation at 150,000 $\times g$ for 1 hr at 4°C.

Purification of native AMPARs

Membranes from all species underwent the same purification steps unless otherwise noted. Membrane pellets were solubilized in 2% digitonin (w/v), 1 μM (R,R)-2b, 1 μM MPQX for 3 hrs with gentle agitation. Ultracentrifugation was used to clarify the material before 15F1-GFP was incubated directly with the solubilized supernatant. After incubation on ice for 20 min with gentle agitation, 15F1-GFP-bound AMPARs were column-purified with Streptactin resin with buffer A (TBS, 1 μM (R,R)-2b, 1 μM MPQX, 0.075% (w/v) digitonin) supplemented with 8 mM d-desthiobiotin and concentrated for SEC. The eluted sample was further purified using a Superose 6 10/300 column (GE Healthcare) in the presence of buffer A. Peak fractions were pooled and concentrated using a 100-kDa cut-off concentrator. The homogeneity and molecular size of the purified native AMPARs were analyzed by silver stained SDS-PAGE and FSEC.

Supporting information

S1 File.

(PDF)

S1 Raw images.

(PDF)

Acknowledgments

We thank Dr. Charles Roselli for donating sheep brains, Dr. John Williams and members of his lab for donating rodent carcasses, Aaron Silverman and Tails & Trotters for dissecting pig brains, T. Provitola for assistance with figures, R. Hallford for proofreading the manuscript, and the Gouaux laboratory members for helpful discussions. This article is subject to HHMI's Open Access to Publications policy. HHMI lab heads have previously granted a nonexclusive CC BY 4.0 license to the public and a sublicensable license to HHMI in their research articles. Pursuant to those licenses, the author-accepted manuscript of this article can be made freely available under a CC BY 4.0 license immediately upon publication. The content is solely the responsibility of the authors and does not necessarily represent the official views of the National Institutes of Health.

Author Contributions

Conceptualization: Prashant Rao, Eric Gouaux.

Formal analysis: Prashant Rao, Eric Gouaux.

Funding acquisition: Eric Gouaux.

Investigation: Prashant Rao, Eric Gouaux.

Methodology: Prashant Rao, Eric Gouaux.

Resources: Eric Gouaux.

Supervision: Eric Gouaux.

Validation: Prashant Rao, Eric Gouaux.

Visualization: Prashant Rao.

Writing – original draft: Prashant Rao.

Writing – review & editing: Prashant Rao, Eric Gouaux.

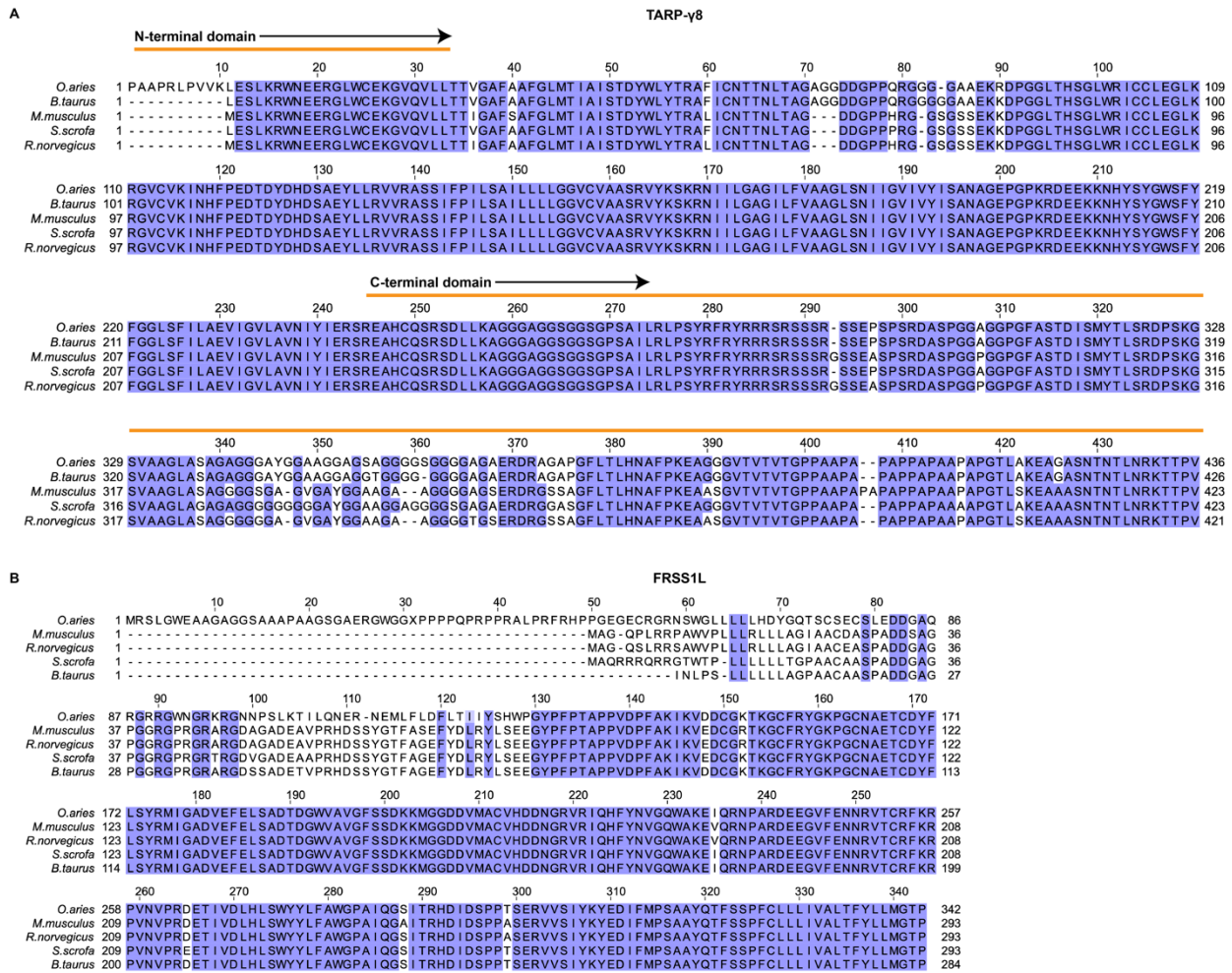
References

1. Traynelis SF, Wollmuth LP, McBain CJ, Menniti FS, Vance KM, Ogden KK, et al. Glutamate receptor ion channels: structure, regulation, and function. *Pharmacol Rev.* 2010; 62: 405–96. <https://doi.org/10.1124/pr.109.002451> PMID: 20716669
2. Saab AS, Neumeier A, Jahn HM, Cupido A, Šimek AAM, Boele HJ, et al. Bergmann glial AMPA receptors are required for fine motor coordination. *Science (1979).* 2012; 337: 749–753. <https://doi.org/10.1126/science.1221140> PMID: 22767895
3. Penn AC, Zhang CL, Georges F, Royer L, Breillat C, Hosy E, et al. Hippocampal LTP and contextual learning require surface diffusion of AMPA receptors. *Nature.* 2017; 549: 384–388. <https://doi.org/10.1038/nature23658> PMID: 28902836
4. Diering GH, Huganir RL. The AMPA Receptor Code of Synaptic Plasticity. *Neuron.* 2018; 100: 314–329. <https://doi.org/10.1016/j.neuron.2018.10.018> PMID: 30359599
5. Keinänen K, Wisden W, Sommer B, Werner P, Herb A, Verdoorn TA, et al. A Family of AMPA-Selective Glutamate Receptors. *Science (1979).* 1990; 249: 556–560. <https://doi.org/10.1126/science.2166337> PMID: 2166337
6. Sobolevsky AI, Rosconi MP, Gouaux E. X-ray structure, symmetry and mechanism of an AMPA-subtype glutamate receptor. *Nature.* 2009; 462: 745–756. <https://doi.org/10.1038/nature08624> PMID: 19946266
7. Twomey EC, Sobolevsky AI. Structural Mechanisms of Gating in Ionotropic Glutamate Receptors. *Biochemistry.* 2018; 57: 267–276. <https://doi.org/10.1021/acs.biochem.7b00891> PMID: 29037031
8. Chen S, Zhao Y, Wang Y, Shekhar M, Tajkhorshid E, Gouaux E. Activation and Desensitization Mechanism of AMPA Receptor-TARP Complex by Cryo-EM. *Cell.* 2017; 170: 1234–1246.e14. <https://doi.org/10.1016/j.cell.2017.07.045> PMID: 28823560
9. Twomey EC, Yelshanskaya M v., Grassucci RA, Frank J, Sobolevsky AI. Structural Bases of Desensitization in AMPA Receptor-Auxiliary Subunit Complexes. *Neuron.* 2017; 94: 569–580.e5. <https://doi.org/10.1016/j.neuron.2017.04.025> PMID: 28472657
10. Schwenk J, Baehrens D, Haupt A, Bildl W, Boudkazi S, Roeper J, et al. Regional diversity and developmental dynamics of the AMPA-receptor proteome in the mammalian brain. *Neuron.* 2014; 84: 41–54. <https://doi.org/10.1016/j.neuron.2014.08.044> PMID: 25242221
11. Schwenk J, Harmel N, Brechet A, Zolles G, Berkefeld H, Müller CS, et al. High-Resolution Proteomics Unravel Architecture and Molecular Diversity of Native AMPA Receptor Complexes. *Neuron.* 2012; 74: 621–633. <https://doi.org/10.1016/j.neuron.2012.03.034> PMID: 22632720
12. Zhao Y, Chen S, Swensen AC, Qian W-J, Gouaux E. Architecture and subunit arrangement of native AMPA receptors elucidated by cryo-EM. *Science.* 2019; 364: 355–362. <https://doi.org/10.1126/science.aaw8250> PMID: 30975770
13. Swanson GT, Kamboj SK, Cull-Candy SG. Single-Channel Properties of Recombinant AMPA Receptors Depend on RNA Editing, Splice Variation, and Subunit Composition. *J. Neurosci.* 1997; 17: 58–69. <https://doi.org/10.1523/JNEUROSCI.17-01-00058.1997> PMID: 8987736
14. Lomeli H, Mosbacher J, Melcher T, Höger T, Geiger JRP, Kuner T, et al. Control of Kinetic Properties of AMPA Receptor Channels by Nuclear RNA Editing. *Science (1979).* 1994; 266: 1709–1713. <https://doi.org/10.1126/science.7992055> PMID: 7992055

15. Bowie D. Polyamine-mediated channel block of ionotropic glutamate receptors and its regulation by auxiliary proteins. *J Biol Chem.* 2018; 293: 18789–18802. <https://doi.org/10.1074/jbc.TM118.003794> PMID: 30333231
16. Jackson AC, Milstein AD, Soto D, Farrant M, Cull-Candy SG, Nicoll RA. Probing TARP modulation of AMPA receptor conductance with polyamine toxins. *Journal of Neuroscience.* 2011; 31: 7511–7520. <https://doi.org/10.1523/JNEUROSCI.6688-10.2011> PMID: 21593335
17. Tikhonov DB, SamoiloVA M v., Buldakova SL, Gmiro VE, Magazanik LG. Voltage-dependent block of native AMPA receptor channels by dicationic compounds. *British Journal of Pharmacology.* 2000; 129: 265–274. <https://doi.org/10.1038/sj.bjp.0703043> PMID: 10694232
18. Coombs ID, Soto D, Zonouzi M, Renzi M, Shelley C, Farrant M, et al. Cornichons modify channel properties of recombinant and glial AMPA receptors. *J Neurosci.* 2012; 32: 9796–804. <https://doi.org/10.1523/JNEUROSCI.0345-12.2012> PMID: 22815494
19. Schober DA, Gill MB, Yu H, Gernert DL, Jeffries MW, Ornstein PL, et al. Transmembrane AMPA receptor regulatory proteins and cornichon-2 allosterically regulate AMPA receptor antagonists and potentiators. *J Biol Chem.* 2011; 286: 13134–42. <https://doi.org/10.1074/jbc.M110.212522> PMID: 21343286
20. Bats C, Soto D, Studniarczyk D, Farrant M, Cull-Candy SG. Channel properties reveal differential expression of TARPed and TARPless AMPARs in stargazer neurons. *Nature Neuroscience* 2012; 15: 853–861. <https://doi.org/10.1038/nn.3107> PMID: 22581185
21. Hume RI, Dingleline R, Heinemann SF. Identification of a site in glutamate receptor subunits that controls calcium permeability. *Science.* 1991; 253: 1028–1031. <https://doi.org/10.1126/science.1653450> PMID: 1653450
22. Burnashev N, Villarreal A, Sakmann B. Dimensions and ion selectivity of recombinant AMPA and kainate receptor channels and their dependence on Q/R site residues. *The Journal of Physiology.* 1996; 496: 165–173. <https://doi.org/10.1113/jphysiol.1996.sp021674> PMID: 8910205
23. Shi Y, Lu W, Milstein AD, Nicoll RA. The Stoichiometry of AMPA Receptors and TARPs Varies by Neuronal Cell Type. *Neuron.* 2009; 62: 633–640. <https://doi.org/10.1016/j.neuron.2009.05.016> PMID: 19524523
24. Schwenk J, Boudkazi S, Kocylowski MK, Brechet A, Zolles G, et al. An ER Assembly Line of AMPA-Receptors Controls Excitatory Neurotransmission and Its Plasticity. *Neuron.* 2019; 104: 680–692 <https://doi.org/10.1016/j.neuron.2019.08.033> PMID: 31604597
25. Bats C, Farrant M, Cull-Candy SG. A role of TARPs in the expression and plasticity of calcium-permeable AMPARs: Evidence from cerebellar neurons and glia. *Neuropharmacology.* 2013. pp. 76–85. <https://doi.org/10.1016/j.neuropharm.2013.03.037> PMID: 23583927
26. Jacobi E, von Engelhardt J. AMPA receptor complex constituents: Control of receptor assembly, membrane trafficking and subcellular localization. *Molecular and Cellular Neuroscience.* 2018; 91: 67–75. <https://doi.org/10.1016/j.mcn.2018.05.008> PMID: 29842943
27. Troyano-Rodriguez E, Mann S, Ullah R, Ahmad M. PRRT1 regulates basal and plasticity-induced AMPA receptor trafficking. *Molecular and Cellular Neuroscience.* 2019; 98: 155–163. <https://doi.org/10.1016/j.mcn.2019.06.008> PMID: 31216424
28. Bissen D, Foss F, Acker-Palmer A. AMPA receptors and their minions: auxiliary proteins in AMPA receptor trafficking. *Cell Mol Life Sci.* 2019; 76: 2133–2169. <https://doi.org/10.1007/s00018-019-03068-7> PMID: 30937469
29. Díaz-Alonso J, Nicoll RA. AMPA receptor trafficking and LTP: Carboxy-termini, amino-termini and TARPs. *Neuropharmacology.* 2021; 108710. <https://doi.org/10.1016/j.neuropharm.2021.108710> PMID: 34271016
30. Shi Y, Suh YH, Milstein AD, Isozaki K, Schmid SM, Roche KW, et al. Functional comparison of the effects of TARPs and cornichons on AMPA receptor trafficking and gating. *PNAS.* 2010; 107: 16315–9. <https://doi.org/10.1073/pnas.1011706107> PMID: 20805473
31. Cho C-H, St-Gelais F, Zhang W, Tomita S, Howe JR. Two Families of TARP Isoforms that Have Distinct Effects on the Kinetic Properties of AMPA Receptors and Synaptic Currents. *Neuron.* 2007; 55: 890–904. <https://doi.org/10.1016/j.neuron.2007.08.024> PMID: 17880893
32. Kato AS, Gill MB, Ho MT, Yu H, Tu Y, Siuda ER, et al. Hippocampal AMPA Receptor Gating Controlled by Both TARP and Cornichon Proteins. *Neuron.* 2010; 68: 1082–1096. <https://doi.org/10.1016/j.neuron.2010.11.026> PMID: 21172611
33. Sun Y, Olson R, Horning M, Armstrong N, Mayer M, Gouaux E. Mechanism of glutamate receptor desensitization. *Nature.* 2002; 417: 245–253. <https://doi.org/10.1038/417245a> PMID: 12015593
34. Yelshanskaya M v., Patel DS, Kottke CM, Kurnikova MG, Sobolevsky AI. Opening of glutamate receptor channel to subconductance levels. *Nature.* 2022; 605: 172–178. <https://doi.org/10.1038/s41586-022-04637-w> PMID: 35444281

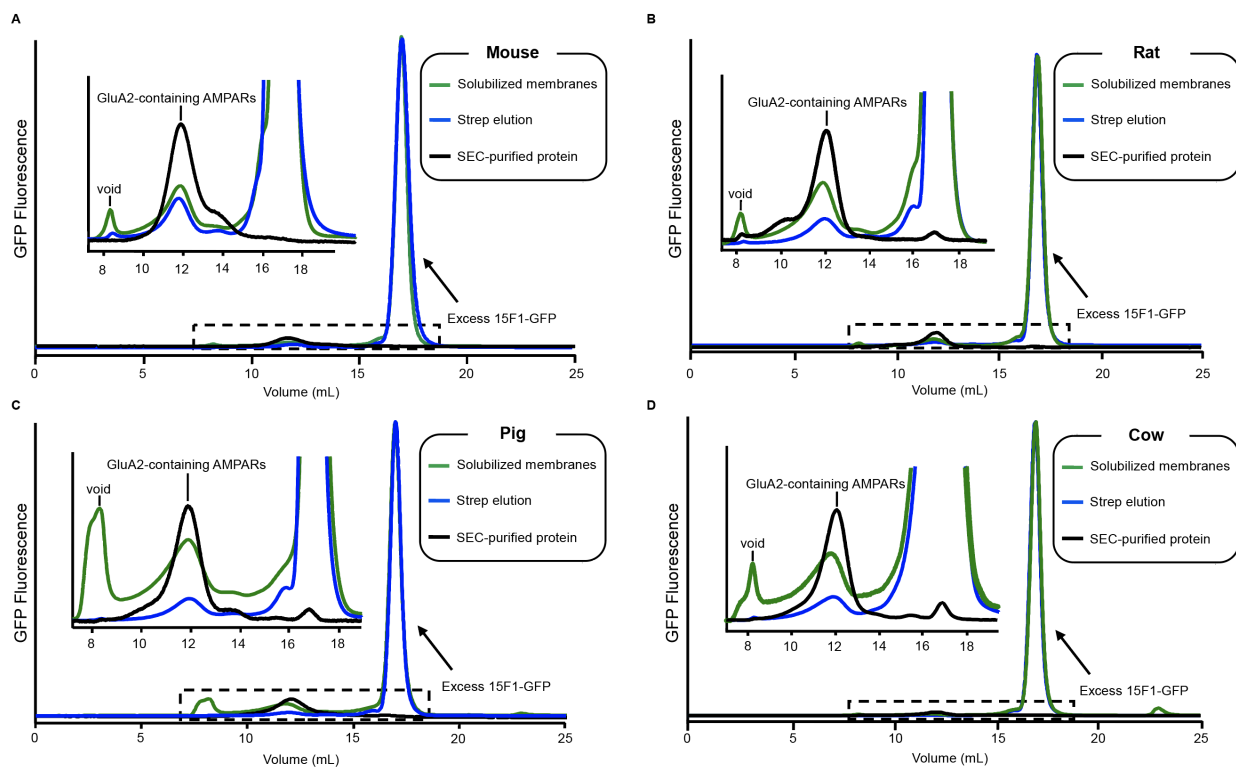
35. Dürr KL, Chen L, Stein RA, De Zorzi R, Folea IM, Walz T, et al. Structure and Dynamics of AMPA Receptor GluA2 in Resting, Pre-Open, and Desensitized States. *Cell*. 2014; 158: 778–792. <https://doi.org/10.1016/j.cell.2014.07.023> PMID: 25109876
36. Luckow VA, Lee SC, Barry GF, Olins P O. Efficient generation of infectious recombinant baculoviruses by site-specific transposon-mediated insertion of foreign genes into a baculovirus genome propagated in *Escherichia coli*. *J Virol*. 1993; 67: 4566–4579. <https://doi.org/10.1128/JVI.67.8.4566-4579.1993> PMID: 8392598
37. Goehring A, Lee CH, Wang KH, Michel JC, Claxton DP, Bacongus I, et al. Screening and large-scale expression of membrane proteins in mammalian cells for structural studies. *Nature Protocols*. 2014; 9: 2574–2585. <https://doi.org/10.1038/nprot.2014.173> PMID: 25299155
38. Nakagawa T. Structures of the AMPA receptor in complex with its auxiliary subunit cornichon. *Science*. 2019; 366: 1259–1263. <https://doi.org/10.1126/science.aay2783> PMID: 31806817
39. Zhao Y, Chen S, Yoshioka C, Bacongus I, Gouaux E. Architecture of fully occupied GluA2 AMPA receptor–TARP complex elucidated by cryo-EM. *Nature*. 2016; 536: 108–111. <https://doi.org/10.1038/nature18961> PMID: 27368053
40. Herguedas B, Watson JF, Ho H, Cais O, García-Nafria J, Greger IH. Architecture of the heteromeric GluA1/2 AMPA receptor in complex with the auxiliary subunit TARP-γ8. *Science*. 2019; eaav9011. <https://doi.org/10.1126/science.aav9011> PMID: 30872532
41. Yu J, Rao P, Clark S, Mitra J, Ha T, Gouaux E. Hippocampal AMPA receptor assemblies and mechanism of allosteric inhibition. *Nature*. 2021; 594: 448–453. <https://doi.org/10.1038/s41586-021-03540-0> PMID: 33981040
42. Jolles AE, Ezenwa VO. Ungulates as model systems for the study of disease processes in natural populations. *J Mammal*. 2015; 96: 4. <https://doi.org/10.1093/jmammal/gyu007> PMID: 32287382
43. Niemann H, Kues W, Carnwath JW. Transgenic Farm Animals: Current Status and Perspectives for Agriculture and Biomedicine. 2009; 1–30. https://doi.org/10.1007/978-3-540-85843-0_1
44. Aigner B, Renner S, Kessler B, Klymiuk N, Kurome M, Wunsch A, et al. Transgenic pigs as models for translational biomedical research. *J Mol Med*. 2010; 88: 653–664. <https://doi.org/10.1007/s00109-010-0610-9> PMID: 20339830
45. Murray SJ, Mitchell NL. The Translational Benefits of Sheep as Large Animal Models of Human Neurological Disorders. *Frontiers in Veterinary Science*. 2022; 9: 831838. <https://doi.org/10.3389/fvets.2022.831838> PMID: 35242840
46. Roth JA, Tuggle CK. Livestock Models in Translational Medicine. *ILAR Journal*. 2015; 56: 1–6. <https://doi.org/10.1093/ilar/ilv011> PMID: 25991694
47. Bon C le, Michon B, Popot JL, Zoonens M. Amphipathic environments for determining the structure of membrane proteins by single-particle electron cryo-microscopy. *Quarterly Reviews of Biophysics*. 2021;54. <https://doi.org/10.1017/S0033583521000044> PMID: 33785082
48. Twomey EC, Yelshanskaya M v., Grassucci RA, Frank J, Sobolevsky AI. Channel opening and gating mechanism in AMPA-subtype glutamate receptors. *Nature*. 2017; 549: 60–65. <https://doi.org/10.1038/nature23479> PMID: 28737760
49. Kawate T, Gouaux E. Fluorescence-Detection Size-Exclusion Chromatography for Precrystallization Screening of Integral Membrane Proteins. *Structure*. 2006; 14: 673–681. <https://doi.org/10.1016/j.str.2006.01.013> PMID: 16615909
50. Milstein AD, Nicoll RA. Regulation of AMPA receptor gating and pharmacology by TARP auxiliary subunits. *Trends Pharmacol Sci*. 2008; 29: 333–9. <https://doi.org/10.1016/j.tips.2008.04.004> PMID: 18514334
51. Kato AS, Gill MB, Yu H, Nisenbaum ES, Brecht DS. TARPs differentially decorate AMPA receptors to specify neuropharmacology. *Trends in Neurosciences*. 2010; 33: 241–248. <https://doi.org/10.1016/j.tins.2010.02.004> PMID: 20219255
52. Menuz K, Stroud RM, Nicoll RA, Hays FA. TARP auxiliary subunits switch AMPA receptor antagonists into partial agonists. *Science (1979)*. 2007; 318: 815–817. <https://doi.org/10.1126/science.1146317> PMID: 17975069
53. Jeong H, Clark S, Goehring A, Dehghani-Ghahnaviyeh S, Rasouli A, Tajkhorshid E, et al. Structures of the TMC-1 complex illuminate mechanosensory transduction. *Nature*. 2022; 610: 796–803. <https://doi.org/10.1038/s41586-022-05314-8> PMID: 36224384
54. Zhu H, Gouaux E. Architecture and assembly mechanism of native glycine receptors. *Nature*. 2021; 599: 513–517. <https://doi.org/10.1038/s41586-021-04022-z> PMID: 34555840
55. Deisenhofer J, Epp O, Miki K, Huber R, Michel H. Structure of the protein subunits in the photosynthetic reaction centre of *Rhodospseudomonas viridis* at 3Å resolution. *Nature*. 1985; 318: 618–624. <https://doi.org/10.1038/318618a0> PMID: 22439175

56. Weiss MS, Abele U, Weckesser J, Welte W, Schiltz E, Schulz GE. Molecular Architecture and Electrostatic Properties of a Bacterial Porin. *Science* (1979). 1991; 254: 1627–1630. <https://doi.org/10.1126/science.1721242> PMID: 1721242
57. Abrahams JP, Leslie AGW, Lutter R, Walker JE. Structure at 2.8 Å resolution of F1-ATPase from bovine heart mitochondria. *Nature*. 1994; 370: 621–628. <https://doi.org/10.1038/370621a0> PMID: 8065448
58. Gu J, Zhang L, Zong S, Guo R, Liu T, Yi J, et al. Cryo-EM structure of the mammalian ATP synthase tetramer bound with inhibitory protein IF1. *Science* (1979). 2019; 364: 1068–1075. <https://doi.org/10.1126/science.aaw4852> PMID: 31197009
59. Ho C-M, Beck JR, Lai M, Cui Y, Goldberg DE, Egea PF, et al. Malaria parasite translocon structure and mechanism of effector export. *Nature*. 2018; 561: 70–75. <https://doi.org/10.1038/s41586-018-0469-4> PMID: 30150771
60. Brill J, Huguenard JR. Sequential Changes in AMPA Receptor Targeting in the Developing Neocortical Excitatory Circuit. *Journal of Neuroscience*. 2008; 28: 13918–13928. <https://doi.org/10.1523/JNEUROSCI.3229-08.2008> PMID: 19091980



S1 Figure. Sequence alignment of TARP- γ 8 and FRRS1L

(A) Sequence alignment of the five selected TARP- γ 8 mammalian variants. Shaded regions highlight complete conservation across all species. (B) Sequence alignment of the five selected FRRS1L mammalian variants. Shaded regions highlight complete conservation across all species.



S2 Figure. FSEC analysis of receptor complexes during immunoaffinity purification

(A-D) Normalized FSEC profiles enable the visualization of the AMPAR complexes throughout the immunoaffinity purification workflow. Insets: Magnified views of the dashed rectangular regions, displaying peaks corresponding to native AMPARs.

Hippocampal AMPA receptor assemblies and mechanism of allosteric inhibition

<https://doi.org/10.1038/s41586-021-03540-0>

Jie Yu^{1,8}, Prashant Rao^{1,8}, Sarah Clark¹, Jaba Mitra^{2,3}, Taekjip Ha^{3,4,5,6} & Eric Gouaux^{1,7}✉

Received: 31 January 2021

Accepted: 12 April 2021

Published online: 12 May 2021

 Check for updates

AMPA-selective glutamate receptors mediate the transduction of signals between the neuronal circuits of the hippocampus¹. The trafficking, localization, kinetics and pharmacology of AMPA receptors are tuned by an ensemble of auxiliary protein subunits, which are integral membrane proteins that associate with the receptor to yield bona fide receptor signalling complexes². Thus far, extensive studies of recombinant AMPA receptor–auxiliary subunit complexes using engineered protein constructs have not been able to faithfully elucidate the molecular architecture of hippocampal AMPA receptor complexes. Here we obtain mouse hippocampal, calcium-impermeable AMPA receptor complexes using immunoaffinity purification and use single-molecule fluorescence and cryo-electron microscopy experiments to elucidate three major AMPA receptor–auxiliary subunit complexes. The GluA1–GluA2, GluA1–GluA2–GluA3 and GluA2–GluA3 receptors are the predominant assemblies, with the auxiliary subunits TARP-γ8 and CNIH2–SynDIG4 non-stochastically positioned at the B'/D' and A'/C' positions, respectively. We further demonstrate how the receptor–TARP-γ8 stoichiometry explains the mechanism of and submaximal inhibition by a clinically relevant, brain-region-specific allosteric inhibitor.

Decades of studies have revealed the central role that ionotropic glutamate receptors have in fast excitatory signalling throughout hippocampal neuronal circuits³ and in synaptic potentiation and depression^{1,4}. One subfamily of ionotropic glutamate receptors—called AMPA receptors (AMPA receptors)—has particularly important roles in the glutamatergic synapses of the hippocampus¹. AMPARs are tetrameric assemblies^{5–7}, which are composed of subunits GluA1–GluA4⁸, of which subunits GluA1 and GluA2 are the most abundantly expressed in the hippocampus^{9,10}. However, AMPARs do not function in isolation as they co-assemble with auxiliary subunits that modulate the trafficking, localization, kinetics and pharmacology of the assembled receptor complex^{2,11}, which further shapes synaptic responses, synaptic plasticity and neuronal circuit activity.

The most prevalent auxiliary subunits in the hippocampus are transmembrane AMPAR regulatory protein gamma 8 (TARP-γ8)¹², cornichon-2 (CNIH2)¹³ and synapse differentiation-induced gene 4 (SynDIG4)⁹. Despite more than two decades having passed since the discovery of the first auxiliary subunit of the AMPARs¹⁴, the molecular and structural composition of hippocampal AMPA receptors (hpAMPARs) remains unresolved. Previous studies revealed structures of the GluA1–GluA2–TARP-γ8 and GluA2–CNIH3 complexes^{15,16}; however, these experiments used artificial, engineered recombinant proteins, leaving the question of the ensemble of AMPAR complexes of the hippocampus unresolved. Therefore, we isolated native, calcium-impermeable AMPAR complexes from mammalian hippocampi and used single-particle cryo-electron microscopy (cryo-EM) and single-molecule total internal

reflection fluorescence (TIRF) experiments¹⁷ to define the functionally relevant molecular composition and structures of the most highly populated classes of hpAMPARs. With these native complexes in hand, we proceeded to elucidate the stoichiometry, pose and mechanism of a clinically relevant, brain-region-selective antagonist, bound to its physiological, functional target.

Structure and composition of hpAMPARs

We isolated GluA2-containing hpAMPARs from mouse hippocampi, followed by immunological labelling of the receptor subunits with the anti-GluA1 11B8 single-chain variable fragment (scFv) and the anti-GluA3 5B2 antigen-binding fragment (Fab)¹⁸ (Extended Data Fig. 1a), with inclusion of the competitive antagonist MPQX and the TARP-γ8-specific antagonist JNJ-55511118 (JNJ)¹⁹. The presence of GluA1–GluA4 subunits, PSD-95, TARP-γ8 and CNIH2 was confirmed by western blot (Extended Data Figs. 1b, 2 and Supplementary Fig. 1), the results of which suggest that our isolation procedure, which represents complexes derived from total receptor mass, had released the synaptic AMPAR complexes from the postsynaptic density. We collected a large single-particle cryo-EM dataset (Supplementary Table 1) and initial two-dimensional classification revealed densities for the 11B8 scFv, the anti-GluA2 15F1 Fab and the 5B2 Fab (Extended Data Fig. 1c, d) bound to their cognate receptor subunits. Two prominent density features extend from the transmembrane domain (TMD) 'up' along the sides of the ligand-binding domain (LBD) of the receptor, probably from the extracellular loops of TARP-γ8

¹Vollum Institute, Oregon Health & Science University, Portland, OR, USA. ²Department of Materials Science and Engineering, University of Illinois at Urbana-Champaign, Urbana, IL, USA.

³Department of Biophysics and Biophysical Chemistry, Johns Hopkins University, Baltimore, MD, USA. ⁴Department of Biophysics, Johns Hopkins University, Baltimore, MD, USA. ⁵Department of Biomedical Engineering, Johns Hopkins University, Baltimore, MD, USA. ⁶Howard Hughes Medical Institute, Baltimore, MD, USA. ⁷Howard Hughes Medical Institute, Portland, OR, USA. ⁸These authors contributed equally: Jie Yu, Prashant Rao. ✉e-mail: gouauxe@ohsu.edu

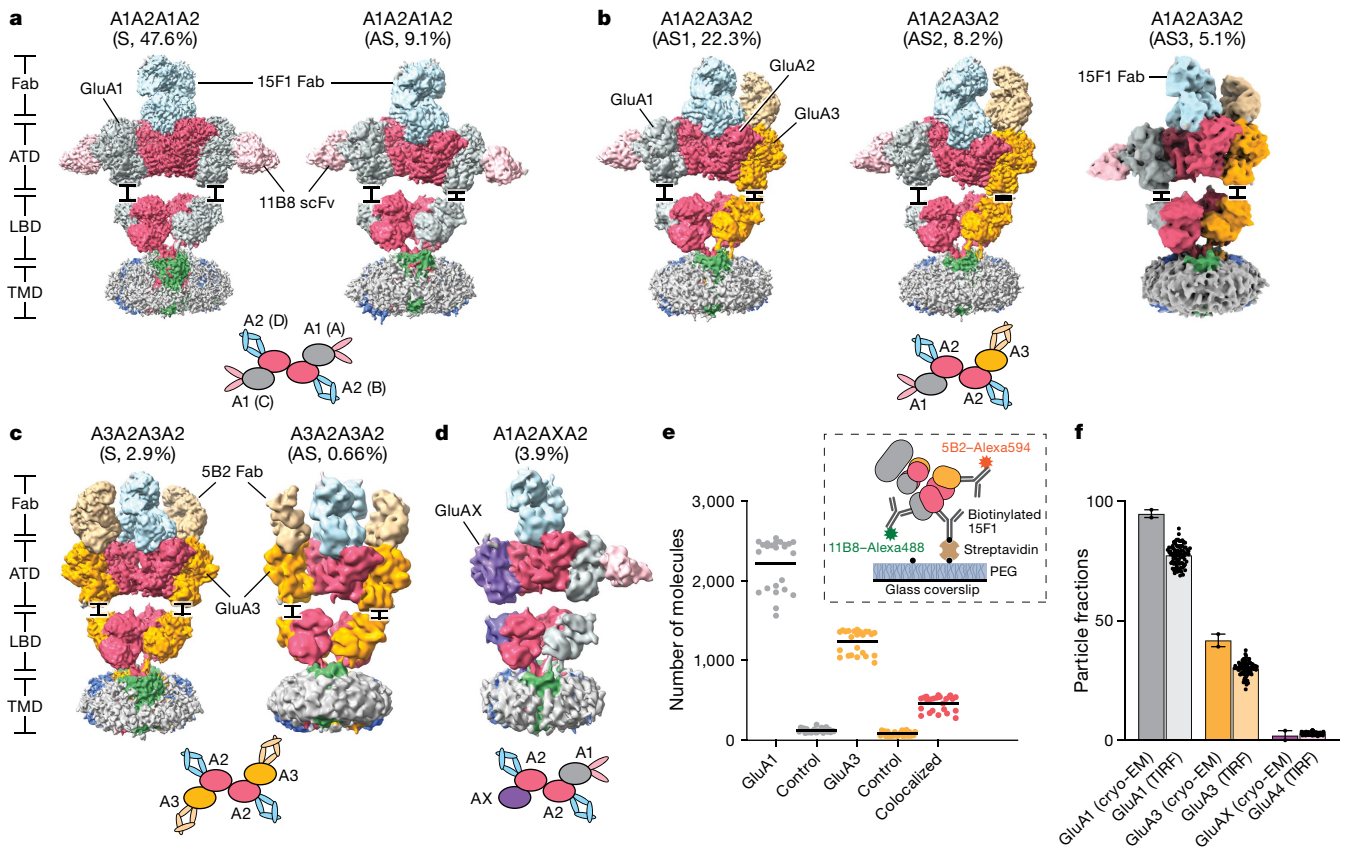


Fig. 1 | Cryo-EM and single-molecule fluorescence analysis of hpAMPA complexes. **a–d**, Cryo-EM maps of the four resolved complexes, viewed parallel to the membrane. Symmetric (S) and asymmetric (AS) conformations within one complex are indicated. GluA1 (A1), GluA2 (A2), GluA3 (A3), GluAX (AX, where 'X' represents an unidentified subunit) and potential auxiliary proteins are shown in grey, red, orange, purple and blue or green, respectively. The anti-GluA1 11B8 scFv, the anti-GluA2 15F1 Fab and the anti-GluA3 5B2 Fab are shown in pink, light blue and light yellow, respectively. Insets are cartoons showing the subunit arrangement and antibody fragment labelling of the ATD layer. **e**, The total number of GluA1, GluA3 and colocalized GluA1–GluA3 subunit-containing molecules detected by SiMPull are shown. See Methods for a description of the control experiments. We observed 37% colocalization of

GluA3 spots with GluA1 spots. $n = 25$ images examined over two independent experiments. The inset shows a schematic of AMPAR SiMPull. PEG, polyethylene glycol. **f**, Distribution of hpAMPA subunits from cryo-EM and SiMPull (TIRF) experiments. The number of each subunit in the single-particle cryo-EM dataset was counted based on the presence of an identifying scFv or Fab fragment. Particle fractions were averaged across two cryo-EM datasets obtained with different data-processing strategies (see Methods). 'GluAX (cryo-EM)' particles are untagged subunits observed by cryo-EM. The subunit fractions from SiMPull experiments were calculated by probing immobilized hpAMPARs with a fluorescently labelled, subunit-specific monoclonal antibody. For SiMPull experiments, $n = 120$ images examined over two independent experiments. Data are mean \pm s.e.m.

(Extended Data Fig. 1d). Multiple rounds of amino-terminal domain (ATD)-focused classification and refinement revealed four distinct hpAMPA complexes that adopted 'Y-shaped' symmetric or asymmetric conformations⁵ (Fig. 1a–d and Extended Data Figs. 3–6).

The hpAMPA complexes composed of GluA1 and GluA2 subunits are the predominant subtypes and were present in around 90% of our structures (Fig. 1a–d), which is consistent with previous studies showing that GluA1 and GluA2 constitute around 80% of the expression of AMPAR subunits in the hippocampus^{9,20,21}. In comparison to the distribution in the whole brain, in which the largest population of receptors is composed of the GluA1–GluA2–GluA3 triheteromeric assembly, with subunits arranged in an A1A2A3A2 manner¹⁸, our dataset analysis revealed that the diheteromeric GluA1–GluA2, with a subunit arrangement of A1A2A1A2, accounts for the largest population in the hippocampus (around 56%) (Fig. 1a). The second major population is the GluA1–GluA2–GluA3 receptor, which accounts for around 36% of the total population, with the GluA1, GluA3 and GluA2 subunits in the A, C and B/D positions, respectively (Fig. 1b). The GluA1–GluA2–GluAX and GluA2–GluA3 receptor complexes comprise around 4% of the population (Fig. 1c, d). The triheteromeric GluA1–GluA2–GluAX receptor includes an 'AX' subunit, which we define as a subunit unlabelled by an antibody fragment either because a Fab or scFv did not

bind or because it is the GluA4 subunit. The GluA2–GluA3 receptor, with a subunit arrangement of A3A2A3A2, is the only complex without the GluA1 subunit and, similar to the subunit composition of the whole population of the receptors in the brain¹⁸, GluA3 subunits reside in the A/C positions.

To independently assess the relative abundance of each subunit in the hippocampus, we performed single-molecule pull-down (SiMPull) experiments¹⁷ by applying the supernatant of mouse hippocampi to imaging chambers coated with the 15F1 monoclonal antibody (Fig. 1e). Fluorescently labelled antibodies specific to the GluA1, GluA3 or GluA4 subunits were then applied to the chamber to enable visualization of the AMPAR subunits. We observed 60% more GluA1 molecules compared with GluA3 molecules, further demonstrating the prevalence of the GluA1 subunit in the hippocampus (Fig. 1e and Extended Data Fig. 7a). When fluorescently labelled anti-GluA1 and anti-GluA3 antibodies were simultaneously added to the imaging chamber, we found that 37% of GluA3 molecules colocalized with GluA1 (Fig. 1e). By comparing the number of spots for each subunit to the total number of observed complexes, we determined that 77% of complexes contained GluA1, 30% contained GluA3 and 3% contained GluA4 using SiMPull (Fig. 1f and Extended Data Fig. 7b). A similar distribution of hpAMPA subunits is observed in the cryo-EM dataset, in which 95% of complexes contained

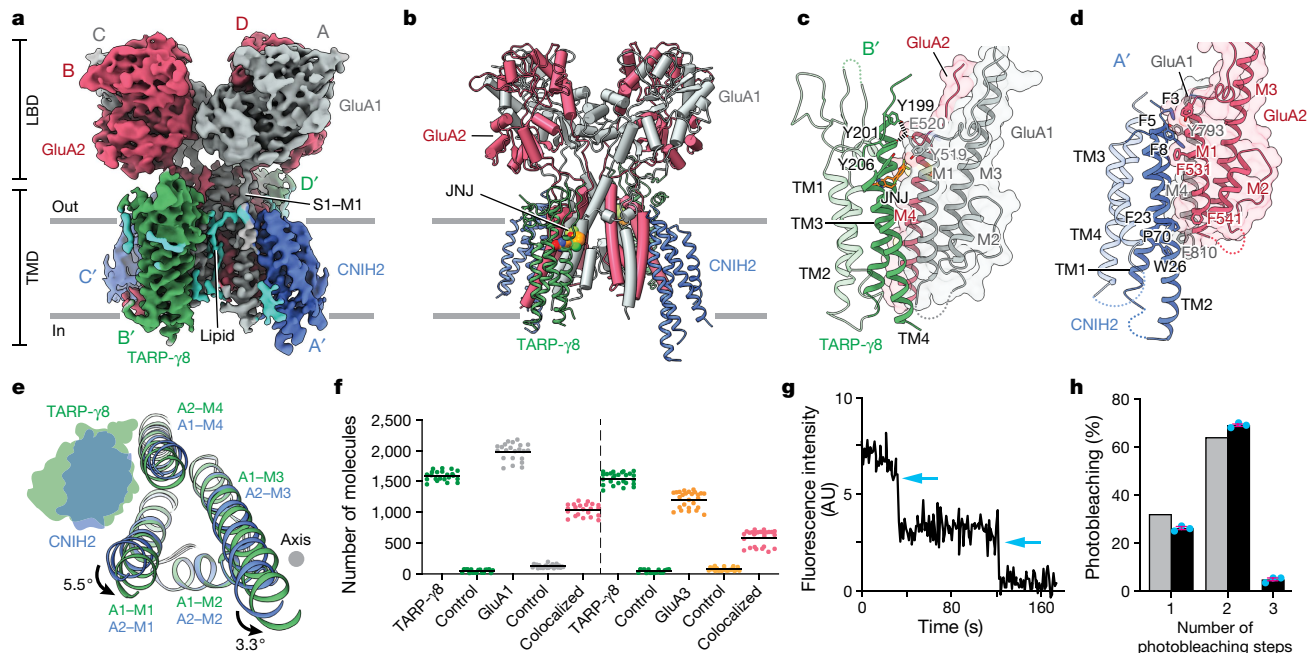


Fig. 2 | Architecture and subunit arrangement of LBD–TMD_{A1/A2} complexes. **a**, Three-dimensional reconstruction of the LBD–TMD_{A1/A2} complex viewed parallel to the membrane. GluA1, GluA2, TARP-γ8 and CNIH2 are shown in grey, red, green and blue, respectively. Lipid-like densities are shown in cyan. **b**, The structures of LBD–TMD_{A1/A2} complexes viewed parallel to the membrane. The JNJ molecule is shown as spheres. **c**, Interface between TARP-γ8 and the receptor. Selected residues along the interface are shown as sticks. Possible hydrogen bonds are indicated by black dashed lines. **d**, Interface between CNIH2 and the receptor, highlighting key residues. **e**, Superposition of the TARP-γ8 interface (**c**) and CNIH2 interface (**d**) to show the conformational differences in the A' and B' positions, viewed perpendicular to the membrane. For clarity, the solvent-accessible surfaces of TARP-γ8 and CNIH2 are shown.

f, Observed colocalization of TARP-γ8 with GluA1 (65%) and colocalization of GluA3 with TARP-γ8 (38%) from SiMPull experiments. See Methods for a description of the control experiments. *n* = 25 images examined over two independent experiments. **g**, Representative trace showing two-step photobleaching (blue arrows) of the 13A8 GFP-tagged anti-TARP-γ8 Fab. AU, arbitrary units. **h**, Summary of distribution of the photobleaching steps for the 13A8 GFP-tagged anti-TARP-γ8 Fab. The distribution of the photobleaching steps for anti-TARP-γ8 Fab (black bars) is consistent with a binomial distribution (grey bars) that assumes a dimeric protein and 80% GFP maturation. *n* = 600 spots were analysed from three photobleaching videos (200 spots per video) collected from two independent experiments. Each video is represented by a blue dot. Data are mean ± s.e.m.

GluA1, 42% contained GluA3 and 4% contained GluAX (Fig. 1f). The percentage of untagged subunits observed in cryo-EM (4%) is close to the number of GluA4 subunits detected by SiMPull (3%), which is consistent with the hypothesis that the subunit that is unlabelled by an antibody fragment in the cryo-EM studies is the GluA4 subunit.

The GluA1–GluA2 and GluA2–GluA3 complexes adopt symmetric and asymmetric conformations and the GluA1–GluA2–GluA3 complex adopts three different conformations¹⁶ (Fig. 1a–c and Extended Data Figs. 5, 6, 8). Inspection of the ATD–LBD interfaces shows that the closest contact regions between the ATD and LBD are conserved across these three complexes and involve a Tyr residue on the LBD, with a glycosylation site, a Lys and a Gln or Glu from the ATD. Tyr465 of GluA1 and Tyr469 of GluA3 may act as a ‘pivot’, transducing conformational signals from the ATD to the LBD. The observation that the ATD glycosylation site densities nearly extend to the LBD may relate to the role of glycosylation in AMPAR physiology²².

Constellation of auxiliary proteins

The hpAMPA reconstructions revealed a partial density for auxiliary proteins surrounding the receptor TMD. To improve the map quality, we performed focused classification and refinement of the GluA1–GluA2, GluA1–GluA2–GluA3 and GluA2–GluA3 receptor subtypes by masking the LBD–TMD layers (Extended Data Fig. 9). We conducted three-dimensional classification individually for the three receptor subtypes and found that all of the subtypes exhibited density features that are consistent with an arrangement of two distinct pairs of auxiliary proteins (Extended Data Figs. 5, 6). Refinement of the LBD–TMD

layers for the GluA1–GluA2 subtype yielded a 3.63 Å resolution map (LBD–TMD_{A1/A2}) that permitted us to assign CNIH2 and TARP-γ8 to the identities of the auxiliary proteins at the A'/C' and B'/D' positions, respectively (Fig. 2a, b). Refinements of the GluA1–GluA2–GluA3 and GluA2–GluA3 subtypes resulted in reconstructions at lower resolution, but they nevertheless exhibited similar auxiliary subunit densities to those seen for the GluA1–GluA2 complexes (Extended Data Figs. 5, 6).

To independently assess the identity and stoichiometry of the hpAMPA auxiliary subunits, we performed SiMPull experiments using fluorescently labelled antibodies and the supernatant of mouse hippocampi. The hpAMPARs were immobilized with the 15F1 monoclonal antibody and probed for TARP-γ8 using a fluorescently labelled anti-TARP-γ8 13A8 monoclonal antibody in conjunction with anti-GluA1 and anti-GluA3 monoclonal antibodies (Extended Data Fig. 7c). The resulting signal for TARP-γ8 colocalized with GluA1 (65%) and GluA3 (38%), which is consistent with the conclusion that TARP-γ8 resides in the hpAMPA complex (Fig. 2f). To measure the stoichiometry of TARP-γ8 in the hpAMPA complex, we generated a GFP-tagged 13A8 Fab for use in single-molecule photobleaching experiments (Extended Data Fig. 7d). Approximately 69% of TARP-γ8 molecules bleached in two steps, 26% bleached in one step and 5% bleached in three steps (Fig. 2g, h), which is consistent with the conclusion that most of the hpAMPA complexes contain two TARP-γ8 subunits. Although we have not yet developed a CNIH2 antibody that is suitable for SiMPull experiments, the density is consistent with CNIH2 occupying the A'/C' auxiliary subunit positions.

TARP-γ8 is the most abundant auxiliary protein in the hippocampus^{9,21,23}, and has key roles in AMPAR gating, trafficking, basal

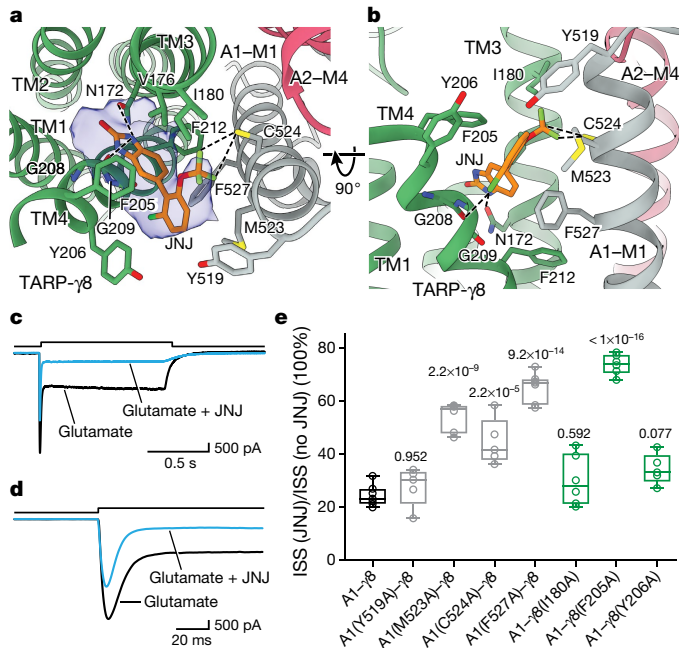


Fig. 3 | JNJ-binding site and mechanism of inhibition. **a, b**, JNJ density and binding site viewed from the extracellular side (**a**) and parallel to the membrane (**b**). JNJ density is shown as a partially transparent blue surface. Possible hydrogen bonds are indicated by black dashed lines. **c, d**, Current responses of GluA1-TARP- γ 8 complexes evoked by glutamate and glutamate plus JNJ (cyan trace) at a timescale of 500 ms (**c**) and 20 ms (**d**), taken after steady-state responses reached a plateau. **e**, Box plot showing the extent of the reduction in the JNJ-induced steady-state (ISS) current from wild-type and mutant proteins. $n = 7$ (wild type (A1- γ 8), GluA1(F527A)-TARP- γ 8), $n = 6$ (GluA1(M523A)-TARP- γ 8, GluA1-TARP- γ 8(I180A), GluA1-TARP- γ 8(F205A)) and $n = 5$ (GluA1(Y19A)-TARP- γ 8, GluA1(C524A)-TARP- γ 8, GluA1-TARP- γ 8(Y206A)). Boxes show the 25th and 75th percentiles; whiskers range from the minimum to the maximum values; and the horizontal line in each box shows the median value. A one-way analysis of variance with Sidak's multiple-comparison test was used to determine the significance and P values are indicated above the boxes.

expression and long-term potentiation of hippocampal neurons^{24–26}. TARP- γ 8 occupies the two-fold-related, gating-dominant B'/D' positions (Fig. 2b), participating in extensive interactions with the M1 helix of the GluA1 subunit and the M4 helix of the GluA2 subunit¹⁵. The transmembrane (TM)3 and TM4 helices of TARP- γ 8 mediate the majority of interactions with the receptor TMD, with Tyr199 and Tyr201 forming hydrogen bonds with Glu520 of the GluA1 subunit (Fig. 2c). The TARP- γ 8 extracellular domain is poised near the lower lobes (D2) of receptor-LBD interdimer interfaces between subunits A/B and C/D, regions of the receptor that are involved in receptor gating and desensitization^{27,28}.

CNIH2 is abundant in the hippocampus, increases the surface expression of AMPAR^{13,29,30}, regulates AMPAR pharmacology^{25,31} and slows the time course of excitatory postsynaptic currents^{30,32}. We observe that CNIH2 occupies the A'/C' positions within the receptor TMD, at the second pair of auxiliary protein 'slots' that flank the M1 and M4 receptor helices, with TM1 and TM2 extending 25 Å into the cytosol (Fig. 2d). Interactions between CNIH2 and the receptor TMD primarily involve two sites that are located at the extracellular and cytosolic boundaries of the TMD. At the extracellular boundary Phe3, Phe5 and Phe8 of CNIH2 form hydrophobic contacts with residues on the GluA2 M1 helix and on the GluA1 M4 helix (Fig. 2d). At the cytosolic interface, Phe22 and Trp26 of CNIH2 make contacts with Leu807 and Phe810 on the GluA1 M4 helix (Fig. 2d). We observe additional points of contact at the cytoplasmic boundary, where a lipid molecule bridges residues Val69 and Ser73 from TM2 to Ile573 on the pore-forming GluA2 M2 helix.

We next sought to compare our LBD-TMD_{A1/A2} structure with the recently reported, recombinant GluA2-CNIH3 structure¹⁶. Analysis of the LBD layer shows that although each LBD dimer is similar, the two dimers are displaced relative to one another by about 3.2 Å (Extended Data Fig. 10). Superimposing the TMD layers revealed larger differences, with an overall root mean square deviation (r.m.s.d.) of 3.3 Å (see Methods). Not only are the M1, M3 and M4 helices of the GluA2-CNIH3 structure rotated by 7–9° relative to the equivalent helices in the LBD-TMD_{A1/A2} structure, but the helices are also 'compressed' and shifted towards the central axis (Extended Data Fig. 10). Accordingly, the auxiliary subunits are also rotated and compressed towards the central axis (Extended Data Fig. 10). These differences suggest that the GluA2-CNIH3 structure may represent a non-native or immature conformation.

The stoichiometry of CNIH2 and TARP- γ 8 offers an opportunity to examine how their positional arrangement is associated with the functional properties of hpAMPA receptors. CNIH2 and TARP- γ 8 occupy the A'/C' and B'/D' positions, respectively. Because both pairs of positions permit direct interaction with the receptor M1 and M4 helices, we superimposed the A' and B' positions. As opposed to the TARP- γ 8-receptor interface, inspection of the upper portion of the M1 helices revealed a 5.5° rotation away from the ion channel at the CNIH2-receptor interface (Fig. 2e). In addition, there is a 3.3° rotation of the M3 helix that results in the expansion of the gating-proximal region of the M3 helix (Fig. 2e). Thus, CNIH2 occupancy of the A'/C' positions promotes a local expansion of the receptor TMD and defines one structural mechanism by which auxiliary protein occupancy may influence channel gating. Furthermore, superposition of the recombinant GluA1-GluA2-TARP- γ 8 structure with our LBD-TMD_{A1/A2} structure shows how the CNIH2 subunits, at the A'/C' positions, are shifted 'inward' towards the central axis relative to the equivalent TARP- γ 8 subunits (Extended Data Fig. 10).

Interactions between the receptor and auxiliary subunit TMDs may also influence the conserved arrangement of auxiliary subunits around the receptor TMD. From our LBD-TMD_{A1/A2} structure, we determined that CNIH2 and TARP- γ 8 both participate in extensive interactions with the receptor M1 and M4 helices. Therefore, we explored the possibility that subunit specificity from the GluA1-GluA2 receptor directly influences the arrangement of auxiliary proteins. Even though the sequences of the M1 and M4 helices are highly conserved between the GluA1 and GluA2 subunits, there is a single difference located in the middle of the M4 helix: Ile796 of GluA1 and its equivalent in GluA2, Val800. At the A'/C' positions, Ile796 is poised to interact with residues Met11, Leu12 and Val15 of TM1 from CNIH2. Conversely, the residues surrounding Val800 are Leu170, Ile173 and Ile174 from TM3 of TARP- γ 8. Notably, we resolved the same two-fold stoichiometry of the auxiliary proteins for the GluA1-GluA2-GluA3 subtype (Extended Data Fig. 6), in which the equivalent residue from the M4 helix of GluA3 is a Val. Thus, the sequence differences in the M4 helix may not be the only mechanism that defines which auxiliary protein occupies a specific position in the receptor complex.

The resolution of the LBD-TMD_{A1/A2} map enabled us to visualize the native lipid densities and the side-chain orientations at the amino acid positions that were dependent on RNA editing. Lipid densities (Fig. 2a) are predominantly located between TARP- γ 8 and CNIH2, near the M1 and M2 helices and do not occlude the ion permeation pathway, which is different from the locations of lipids in recombinant structures¹⁶. The lipid locations suggest they may have a role in the assembly or function of the receptor. At the apex of the selectivity filter, there is a clear density for Gln582 and Arg586 at the Gln/Arg (Q/R) sites of the GluA1 and GluA2 subunits, respectively (Extended Data Fig. 11a, b). Visualization of Arg586³³, which projects 'upward' into the central vestibule, illustrates how charged repulsion dictates ion selectivity³⁴, single-channel conductance³⁵ and resistance to cytoplasmic polyamines³⁶. Within the LBD, RNA editing at the Arg/Gly (R/G) sites³⁷ modulates the kinetic properties of AMPARs. We assigned Arg739 and Arg743 to the R/G sites

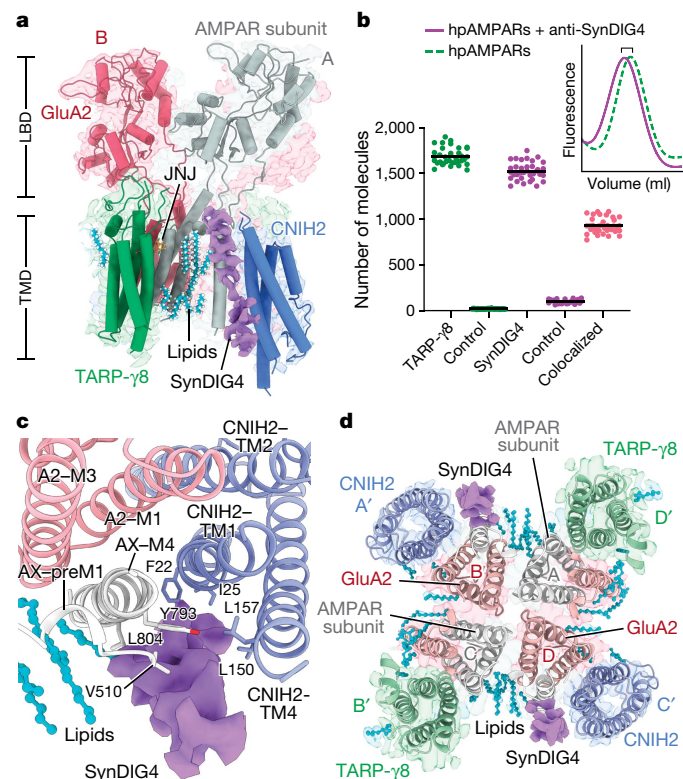


Fig. 4 | Elucidation of putative SynDIG4 density and interaction sites. **a**, The LBD–TMD_{mix} reconstruction viewed parallel to the membrane. For clarity, only two AMPAR subunits are displayed in each panel. Cryo-EM density for SynDIG4 is shown in purple. Lipids are displayed in cyan. GluA2, TARP-γ8 and CNIH2 are shown in red, green and blue, respectively. AMPAR subunits in positions A (grey) and C (not shown) are undetermined. **b**, Observed colocalization of SynDIG4 with TARP-γ8 (61%) from SiMPull experiments. See Methods for a description of the control experiments. Inset: the dotted line represents the chromatography profile of hpAMPARs incubated with the anti-TARP-γ8 Alexa647-labelled 13A8 monoclonal antibody. The solid line represents the profile of the hpAMPARs incubated with the Alexa647-labelled 13A8 monoclonal antibody and the anti-SynDIG4 monoclonal antibody. A shift in size represents the detection of SynDIG4 bound to the hpAMPARs. **c**, Putative interaction sites of SynDIG4 with CNIH2 and an undetermined AMPAR subunit(s). View is perpendicular to the membrane. Red model, GluA2; grey model, an undetermined AMPAR subunit (AX). **d**, Top-down view perpendicular to the membrane displaying the overall stoichiometry and arrangement of the TMD layer. Cryo-EM density for putative SynDIG4 is opaque, density for all other proteins is transparent.

for GluA1 and GluA2, respectively, based on density of the side chains (Extended Data Fig. 11a, b), which suggests that the majority of the isolated GluA1–GluA2 receptors that contributed to our LBD–TMD_{A1/A2} map would exhibit the fast kinetics associated with the R variants.

Mechanism of JNJ antagonism

JNJ, a brain-region-specific TARP-γ8-dependent AMPAR antagonist¹⁹, incompletely inhibits the steady-state current that is evoked by saturating glutamate (Fig. 3c, d). We discovered two-fold-related densities of JNJ poised at each side of the interfaces between TARP-γ8 and GluA1 (Figs. 2b, c, 3a). The benzimidazolinone group of JNJ is wedged in between TM3 and TM4 of TARP-γ8 whereas the fluoro group points towards the M1 helix of GluA1, which is consistent with the predicted binding pose¹⁹. Extensive interactions are formed between JNJ and the surrounding residues, including possible hydrogen bonds and polar interactions between the benzimidazolinone group and the backbone carbonyl groups of Gly208 and Asn172 of TARP-γ8, and between the fluoro group

and Cys524 of GluA1. In addition, the benzene group of the JNJ molecule is sandwiched between Phe205 of TARP-γ8 and Phe527 of GluA1 (Fig. 3a, b). Binding of JNJ expands a cavity at the interface of TARP-γ8 and GluA1, inducing an ‘inward’ rotation of the M1 helix and increasing distances between the surrounding residues to prevent clashes with TM3–TM4 of TARP-γ8 and M1 of GluA1, in agreement with studies that proposed that the unoccupied binding pocket is too small to allow the binding of drugs that target TARP-γ8¹⁵. We speculate that JNJ antagonizes receptor gating by precluding the expansion of the M3 gating helices and the ‘outward’ movement of the M1 helices, thereby negatively modulating receptor function. Moreover, because there are only two binding sites, the GluA2 M3 helices are less constrained by JNJ binding and may be able to expand the ‘gating ring’, thus enabling partial opening of the ion channel gate, leading to incomplete receptor inhibition.

Previous studies have determined that mutations of several TARP-γ8 residues that surround the JNJ-binding site reduce the potency of JNJ¹⁹. Nevertheless, several residues from GluA1 and TARP-γ8 also interact with or are near the JNJ molecule and yet have not been examined. We therefore mutated these residues to alanine and carried out electrophysiology studies, showing that the M523A, C524A and F527A mutants of GluA1 and the F205A mutant of TARP-γ8 substantially diminished the efficacy of JNJ-induced reduction of glutamate-induced currents. The effects were especially profound for the GluA1(F527A)–TARP-γ8 and GluA1–TARP-γ8(F205A) mutants (Fig. 3e and Extended Data Fig. 12) and are therefore in agreement with the idea that these residues have key roles in the binding and activity of JNJ.

Putative SynDIG4 interaction sites

The LBD–TMD_{A1/A2} map shows additional density features that surround the receptor and auxiliary proteins that could not be assigned to lipids or other small molecules. To increase the resolution of the density map, we rationalized that combining all of the receptor subtypes and using signal subtraction to remove the ATD layer and antibody fragments would yield a higher-resolution map, knowing that the amino acid sequences of the AMPAR subunit TMDs are highly conserved. Indeed, this image-processing strategy (see Methods, ‘Data-processing strategy 2’) yielded a map at 3.25 Å resolution, which we call the LBD–TMD_{mix} map (Extended Data Figs. 6, 11c, d, 13). The LBD–TMD_{mix} map displays the same subunit arrangement and auxiliary protein composition as observed in the LBD–TMD_{A1/A2} map, except that a mixture of GluA1, GluA3 and GluA4 (GluA_{mix}) subunits occupies the A and C positions (Fig. 4a). Notably, the observed density features associated with arginine residues at the R/G and Q/R sites of GluA2 and GluA_{mix} subunits remain consistent with extensive RNA editing (R in the GluA2–A4, R/G site) in the hippocampus. In addition, the LBD–TMD_{mix} map enabled us to augment the trace of the CNIH2 TM3–TM4 loop, which is proximal to the crucial M1–M2 linker of the receptor. We also observe prominent lipid-like densities that we modelled as lipid alkyl chains, and found that the lipid positions differ from those determined in the recombinant receptor–auxiliary protein complexes, in that they are poised to contact the M1 and M4 helices or reside near the pore-lining M2 helix (Fig. 4a, d). In addition, there are several lipids that surround the TMs of TARP-γ8 and CNIH2.

We also observe an unknown two-fold-related, helix-like density that is oriented nearly parallel to the M4 helix of GluA1 and located in a crevice at the interface of the GluA1 and CNIH2 subunits (Fig. 4d). The shape and location of the unknown density led us to hypothesize that it was an additional auxiliary hpAMPAR protein. SynDIG4, which is also known as proline-rich transmembrane protein 1 (PRRT1), is an AMPAR-associated protein that is enriched in the hippocampus⁹, associates with TARP-γ8 and CNIH2, colocalizes with GluA1 and is predicted to have at least one transmembrane domain^{38,39}. To determine whether SynDIG4 copurified with the hpAMPAR complex, we carried out SiMPull and fluorescence-detection, size-exclusion chromatography (FSEC)

experiments using a well-characterized anti-SynDIG4 monoclonal antibody³⁸. In the SiMPull experiments, we observed a signal when immobilized hpAMPA complexes were probed with a fluorescently labelled anti-SynDIG4 monoclonal antibody (Fig. 4b and Extended Data Fig. 7e). The spots that correspond to SynDIG4 exhibit 61% colocalization with TARP-γ8, which suggests that they are located in the same hpAMPA complexes (Fig. 4b). Furthermore, FSEC experiments using the same fluorescently labelled monoclonal antibodies demonstrate that the AMPAR–TARP-γ8 complex can be shifted by the anti-SynDIG4 monoclonal antibody, thus proving that SynDIG4 is associated with the hpAMPA complex (Fig. 4b). Our data suggest that the unknown density is SynDIG4, although further experiments are required to unambiguously show that it is not another auxiliary subunit. Nevertheless, we note that the putative SynDIG4 TMD is arranged approximately parallel to the TM helices of the receptor, making extensive contacts with the M4 helix of GluA1 and the TM1/4 helices of CNIH2 (Fig. 4a, c). The location of SynDIG4, on the periphery of the hpAMPA complex, is consistent with it having roles in receptor trafficking and localization and less of a role in receptor gating^{39,40}.

The molecular structures of hpAMPA complexes reveal rules for the assembly of receptor subunits and auxiliary proteins and the binding site of the clinically relevant TARP-γ8 antagonist, JNJ. GluA1 is the most prevalent subunit assembled in the GluA2-containing hpAMPA complex, highlighting the important roles of GluA1 and GluA2 in synaptic transmission. The GluA1–GluA2 complex and the recently discovered GluA1–GluA2–GluA3 receptor are the major assemblies that contain the GluA2 subunit exclusively at the B/D positions, whereas the A/C positions are more permissive, suggesting that differential insertion of GluA1 or GluA3 subunits at the A/C positions is a mechanism of synaptic tuning. We further show that the composition and assembly of auxiliary subunits is preserved for the GluA1–GluA2, GluA2–GluA3 and GluA1–GluA2–GluA3 complexes, in which TARP-γ8 and CNIH2 occupy the B'/D' and the A'/C' positions, respectively. The well-resolved density from the LBD–TMD_{A1/A2} structure defines the position of crucial residues that modulate the permeation and gating of the receptor, including RNA-editing-dependent amino acid variations. Notably, we further uncovered how JNJ binds to the TARP-γ8–receptor interface and stabilizes the receptor in a closed state, thus demonstrating that the structure-based design of small molecules is feasible using the bona fide native receptor target. SynDIG4 assembles on the periphery of the TMD, interacting extensively with CNIH2, consistent with its primary role in modulating receptor trafficking and localization. The native hpAMPA complexes do not have the bias of artificial, engineered complexes and show how the functional properties of AMPARs are sculpted by the non-stochastic assembly of receptor and auxiliary protein components.

Online content

Any methods, additional references, Nature Research reporting summaries, source data, extended data, supplementary information, acknowledgements, peer review information; details of author contributions and competing interests; and statements of data and code availability are available at <https://doi.org/10.1038/s41586-021-03540-0>.

- Diering, G. H. & Haganir, R. L. The AMPA receptor code of synaptic plasticity. *Neuron* **100**, 314–329 (2018).
- Jackson, A. C. & Nicoll, R. A. The expanding social network of ionotropic glutamate receptors: TARPs and other transmembrane auxiliary subunits. *Neuron* **70**, 178–199 (2011).
- Collingridge, G. L., Kehl, S. J. & McLennan, H. Excitatory amino acids in synaptic transmission in the Schaffer collateral-commissural pathway of the rat hippocampus. *J. Physiol.* **334**, 33–46 (1983).
- Bliss, T. V. & Lomo, T. Long-lasting potentiation of synaptic transmission in the dentate area of the anaesthetized rabbit following stimulation of the perforant path. *J. Physiol.* **232**, 331–356 (1973).
- Rosenmund, C., Stern-Bach, Y. & Stevens, C. F. The tetrameric structure of a glutamate receptor channel. *Science* **280**, 1596–1599 (1998).

- Sobolevsky, A. I., Rosconi, M. P. & Gouaux, E. X-ray structure, symmetry and mechanism of an AMPA-subtype glutamate receptor. *Nature* **462**, 745–756 (2009).
- Traynelis, S. F. et al. Glutamate receptor ion channels: structure, regulation, and function. *Pharmacol. Rev.* **62**, 405–496 (2010).
- Keinanen, K. et al. A family of AMPA-selective glutamate receptors. *Science* **249**, 556–560 (1990).
- Schwenk, J. et al. Regional diversity and developmental dynamics of the AMPA-receptor proteome in the mammalian brain. *Neuron* **84**, 41–54 (2014).
- Wenthold, R. J., Petralia, R. S., Blahos, J. I. & Niedzielski, A. S. Evidence for multiple AMPA receptor complexes in hippocampal CA1/CA2 neurons. *J. Neurosci.* **16**, 1982–1989 (1996).
- Kamalova, A. & Nakagawa, T. AMPA receptor structure and auxiliary subunits. *J. Physiol.* **599**, 453–469 (2021).
- Tomita, S. et al. Functional studies and distribution define a family of transmembrane AMPA receptor regulatory proteins. *J. Cell Biol.* **161**, 805–816 (2003).
- Schwenk, J. et al. Functional proteomics identify cornichon proteins as auxiliary subunits of AMPA receptors. *Science* **323**, 1313–1319 (2009).
- Chen, L. et al. Stargazin regulates synaptic targeting of AMPA receptors by two distinct mechanisms. *Nature* **408**, 936–943 (2000).
- Herguedas, B. et al. Architecture of the heteromeric GluA1/2 AMPA receptor in complex with the auxiliary subunit TARP γ8. *Science* **364**, eaav9011 (2019).
- Nakagawa, T. Structures of the AMPA receptor in complex with its auxiliary subunit cornichon. *Science* **366**, 1259–1263 (2019).
- Jain, A. et al. Probing cellular protein complexes using single-molecule pull-down. *Nature* **473**, 484–488 (2011).
- Zhao, Y., Chen, S., Swensen, A. C., Qian, W. J. & Gouaux, E. Architecture and subunit arrangement of native AMPA receptors elucidated by cryo-EM. *Science* **364**, 355–362 (2019).
- Maher, M. P. et al. Discovery and characterization of AMPA receptor modulators selective for TARP-γ8. *J. Pharmacol. Exp. Ther.* **357**, 394–414 (2016).
- Lu, W. et al. Subunit composition of synaptic AMPA receptors revealed by a single-cell genetic approach. *Neuron* **62**, 254–268 (2009).
- Jacobi, E. & von Engelhardt, J. Diversity in AMPA receptor complexes in the brain. *Curr. Opin. Neurobiol.* **45**, 32–38 (2017).
- Morise, J. et al. Distinct cell surface expression patterns of N-glycosylation site mutants of AMPA-type glutamate receptor under the homo-oligomeric expression conditions. *Int. J. Mol. Sci.* **21**, 5101 (2020).
- Fukaya, M. et al. Abundant distribution of TARP γ-8 in synaptic and extrasynaptic surface of hippocampal neurons and its major role in AMPA receptor expression on spines and dendrites. *Eur. J. Neurosci.* **24**, 2177–2190 (2006).
- Rouach, N. et al. TARP γ-8 controls hippocampal AMPA receptor number, distribution and synaptic plasticity. *Nat. Neurosci.* **8**, 1525–1533 (2005).
- Kato, A. S. et al. Hippocampal AMPA receptor gating controlled by both TARP and cornichon proteins. *Neuron* **68**, 1082–1096 (2010).
- Carrillo, E. et al. Mechanism of modulation of AMPA receptors by TARP-γ8. *J. Gen. Physiol.* **152**, jgp.201912451 (2020).
- Plested, A. J. & Mayer, M. L. AMPA receptor ligand binding domain mobility revealed by functional cross linking. *J. Neurosci.* **29**, 11912–11923 (2009).
- Baranovic, J. et al. Dynamics of the ligand binding domain layer during AMPA receptor activation. *Biophys. J.* **110**, 896–911 (2016).
- Harmel, N. et al. AMPA receptors commandeer an ancient cargo exporter for use as an auxiliary subunit for signaling. *PLoS ONE* **7**, e30681 (2012).
- Boudkazi, S., Brechet, A., Schwenk, J. & Fakler, B. Cornichon2 dictates the time course of excitatory transmission at individual hippocampal synapses. *Neuron* **82**, 848–858 (2014).
- Gill, M. B., Kato, A. S., Wang, H. & Brecht, D. S. AMPA receptor modulation by cornichon-2 dictated by transmembrane AMPA receptor regulatory protein isoform. *Eur. J. Neurosci.* **35**, 182–194 (2012).
- Herring, B. E. et al. Cornichon proteins determine the subunit composition of synaptic AMPA receptors. *Neuron* **77**, 1083–1096 (2013).
- Sommer, B., Köhler, M., Sprengel, R. & Seeburg, P. H. RNA editing in brain controls a determinant of ion flow in glutamate-gated channels. *Cell* **67**, 11–19 (1991).
- Burnashev, N., Villarroel, A. & Sakmann, B. Dimensions and ion selectivity of recombinant AMPA and kainate receptor channels and their dependence on Q/R site residues. *J. Physiol.* **496**, 165–173 (1996).
- Swanson, G. T., Kamboj, S. K. & Cull-Candy, S. G. Single-channel properties of recombinant AMPA receptors depend on RNA editing, splice variation, and subunit composition. *J. Neurosci.* **17**, 58–69 (1997).
- Bowie, D. & Mayer, M. L. Inward rectification of both AMPA and kainate subtype glutamate receptors generated by polyamine-mediated ion channel block. *Neuron* **15**, 453–462 (1995).
- Lomeli, H. et al. Control of kinetic properties of AMPA receptor channels by nuclear RNA editing. *Science* **266**, 1709–1713 (1994).
- Kirk, L. M. et al. Distribution of the SynDIG4/proline-rich transmembrane protein 1 in rat brain. *J. Comp. Neurol.* **524**, 2266–2280 (2016).
- Matt, L. et al. SynDIG4/Prprt1 is required for excitatory synapse development and plasticity underlying cognitive function. *Cell Rep.* **22**, 2246–2253 (2018).
- Troyano-Rodriguez, E., Mann, S., Ullah, R. & Ahmad, M. PRRT1 regulates basal and plasticity-induced AMPA receptor trafficking. *Mol. Cell. Neurosci.* **98**, 155–163 (2019).

Publisher's note Springer Nature remains neutral with regard to jurisdictional claims in published maps and institutional affiliations.

© The Author(s), under exclusive licence to Springer Nature Limited 2021

Methods

Expression and purification of anti-GluA1 11B8 scFv

The DNA sequences encoding the light and heavy chains of the variable domains of the GluA1-specific 11B8 monoclonal antibody, with the following modifications, were cloned into the pET-22b vector for expression in *Escherichia coli* BL21 cells. A hydrophilic linker, (SGGGG)₃, was used to connect the light chain (V_L) and heavy chain (V_H), and an N-terminal pelB signal peptide and a C-terminal Strep II tag were also introduced into the construct. Cells were grown at 37 °C in terrific broth containing 100 µg ml⁻¹ ampicillin. Expression of the 11B8 scFv was induced by addition of 0.1 mM isopropyl β-D-1-thiogalactopyranoside (IPTG) when the optical density at 600 nm (OD₆₀₀) reached 1.5–1.8. The temperature of the cultures was reduced to 25 °C and the cells were grown for another 20 h. Cells were collected by centrifugation and lysed by osmotic shock in a lysis buffer containing 200 mM Tris, pH 8.0, 20% sucrose and 1 mM EDTA for 30 min on ice. Centrifugation at 200,000g, for 1 h at 4 °C, was carried out to separate periplasmic proteins from cells and cell debris. The supernatant was dialysed three times against 2 l of TBS buffer (20 mM Tris, pH 8.0 and 150 mM NaCl) at 4 °C to remove sucrose. The 11B8 scFv was purified by Strep-Tactin affinity chromatography and the eluted protein was subjected to size-exclusion chromatography (SEC) using a Superdex 75 10/300 column equilibrated with TBS buffer. Peak fractions corresponding to monomeric 11B8 scFv were pooled and stored at –80 °C. Concentrated 11B8 scFv without any dilution was used for structural determination experiments.

Expression and purification of anti-GluA2 15F1 Fab

The DNA sequences encoding the Fab domains of the light and heavy chains from the GluA2-specific 15F1 monoclonal antibody were cloned into a bicistronic pFastBac1 vector for baculovirus expression in Sf9 insect cells, with the following modifications⁴¹. The GP64 signal peptide (MVSAILVYVLLAAAAHSAFA) was included at the N terminus of the heavy and light chains, whereas a Strep II tag was introduced at the C terminus of the heavy chain. Insect cells were transduced with baculovirus and cultured at 27 °C. After 96 h, the supernatant was collected and the pH was adjusted to 8.0, followed by clarification at 10,000g for 20 min at 4 °C. The supernatant was concentrated to around 200 ml by tangential flow filtration using a 30-kDa molecular-mass cut-off filter and dialysed three times against TBS buffer for 36 h. Strep-Tactin affinity chromatography was used to isolate the 15F1 Fab, which was further purified by SEC in the presence of TBS buffer. Peak fractions were pooled and stored at –80 °C. Concentrated 15F1 Fab without any dilution was used for structural determination experiments.

Purification of anti-GluA3 5B2 monoclonal antibody and Fab

The GluA3-specific monoclonal antibody (5B2) was purified from hybridoma supernatant by protein-A agarose chromatography. To produce the Fab fragment, the 5B2 monoclonal antibody was digested by papain (1:30 w/w ratio) along with 5 mM cysteine and 1 mM EDTA for 2.5 h at 37 °C. The reaction was stopped by 30 mM iodoacetamide for 20 min in the dark. Fc fragments were removed by protein-A agarose chromatography and the flow-through Fab fraction was collected and subjected to SEC in TBS buffer. Peak fractions were pooled, concentrated and stored at –80 °C. Concentrated 5B2 monoclonal antibody without any dilution was used for structural determination experiments.

Generation of anti-GluA4 antibody

A mouse GluA4 construct (Uniprot code: Q9Z2W8) was engineered by addition of a C-terminal Strep II tag and deletion of largely unstructured C-terminal residues after Lys848, and was cloned into a pEG BacMam vector for baculovirus-mediated expression in mammalian cells⁴². The receptor was expressed in virally transduced HEK293S GnT1⁻ cells and purified by Strep-Tactin affinity chromatography and SEC in TBS buffer supplemented with *n*-dodecyl-β-D-maltopyranoside (DDM).

As previously described⁴³, the purified GluA4 protein was reconstituted into lipid-A-containing liposomes for mouse immunization and antibody production. Subsequently, candidates were screened by FSEC⁴⁴ and western blot, and binding affinities were determined by biolayer interferometry using an OctetRED384 instrument. We identified one monoclonal antibody produced by the E3 hybridoma cell line that binds to a tertiary epitope of GluA4 with a dissociation constant (*K_d*) of 13 nM. To examine the cross-reactivity of the E3 monoclonal antibody with other AMPARs, we carried out FSEC experiments using GluA1–mKalama-, GluA2–GFP- and GluA3–GFP-tagged receptors, and determined that the E3 monoclonal antibody is specific to the GluA4 receptor.

Generation and expression of the anti-TARP-γ8 antibody

The mouse TARP-γ8 protein (Uniprot code: Q8VHW2) was modified by the addition of a C-terminal Strep II tag. DNA encoding this construct was cloned into a pEG BacMam vector for expression in HEK293S GnT1⁻ cells through baculovirus transduction⁴². Strep-Tactin affinity chromatography and SEC were carried out to purify TARP-γ8 in TBS buffer supplemented with 0.5 mM DDM. Purified TARP-γ8 was reconstituted into lipid-A-containing liposomes for mouse immunization and antibody production, as described previously⁴³. Secreted antibodies from the subsequent positive hybridoma clones were screened by FSEC⁴⁴ and western blot, and affinities were determined by Octet measurements. We identified a western-blot positive mouse monoclonal antibody produced by the 13A8 hybridoma cell line with a *K_d* of 1 nM. Cross-reactivity of the 13A8 monoclonal antibody with other members of the TARP family was investigated by FSEC using TARP-γ2–GFP-, TARP-γ3–GFP-, TARP-γ4–GFP- and TARP-γ7–GFP-tagged proteins. We observed no cross-reactivity and found that the 13A8 monoclonal antibody is specific for TARP-γ8.

The DNA sequences encoding the 13A8 Fab domains of the heavy and light chains were derived from hybridoma cell mRNA via PCR amplification and were cloned into a bicistronic pFastBac1 vector. GP64 signal peptides were included at the N terminus of the heavy and light chains, whereas a GFP tag was introduced to the C terminus of the heavy chain, followed by a twin Strep II tag. Expression and purification strategies were the same as those used for the 15F1 Fab (see 'Expression and purification of anti-GluA2 15F1 Fab').

Isolation of native hpAMPA receptors

Native hpAMPA receptors were isolated from 200 C57BL/6 male and female mice (Charles River), aged 28–42 days. Mouse brains were dissected and immediately placed in ice-cold TBS buffer before dissection. Before isolating hippocampi, a clean razor blade was used to remove cerebellum by cutting along the junction to the cerebral cortex, followed by hemisection of the left brain. The cortical hemisphere was peeled away⁴⁵ by placing two microspatula tips over the occipital cortex to expose the hippocampus. Subsequently, one spatula tip was used to anchor the brain and another spatula tip was positioned under the caudal tip of hippocampus. The hippocampus was then 'scooped out' by lateral movement of the second spatula tip. The collected hippocampi were immediately placed in ice-cold TBS buffer in the presence of 0.8 µM aprotinin, 2 µg ml⁻¹ leupeptin, 2 mM pepstatin A, 1 mM phenylmethylsulfonyl fluoride, 2 µM MPQX ([[3,4-dihydro-7-(4-morpholinyl)-2,3-dioxo-6-(trifluoromethyl)-1(2*H*)-quinoxaliny]methyl]phosphonic acid) and 2 µM JNJ-5511118 (5-[2-chloro-6-(trifluoromethoxy)phenyl]-1,3-dihydro-2*H*-benzimidazol-2-one), homogenized using a Teflon-glass grinder and further disrupted by brief sonication, using a sonicator equipped with a tip size of 1.27 cm, for 5 min with 3 s on and 6 s off, at medium power, on ice. The membrane fraction was collected by ultracentrifugation at 200,000g for 1 h at 4 °C. The crude membranes were solubilized in 2% (w/v) digitonin for 3 h with slow stirring at 4 °C. The resulting solution was clarified by ultracentrifugation, and the supernatant was collected and mixed with excess Strep-tagged 15F1

Fab before passing through a Strep-Tactin affinity column by gravity flow. After washing the column extensively using buffer A (20 mM Tris, pH 8.0, 150 mM NaCl, 0.075% (w/v) digitonin, 2 μ M MPQX and 2 μ M JNJ-55511118), the complex of 15F1-bound GluA2-containing receptor and excess 15F1 were eluted by buffer A supplemented with 5 mM D-desthiobiotin. The eluted sample was incubated with an excess of 11B8 scFv and 5B2 Fab on ice for 30 min, concentrated and further purified using a Superose 6 10/300 GL column in the presence of buffer A. Peak fractions were pooled and concentrated using a 100-kDa cut-off concentrator to an OD₂₈₀ of 5 mg ml⁻¹ for biochemical analysis and cryo-EM studies.

Cryo-EM sample preparation and data acquisition

A 2.5- μ l aliquot of purified native hpAMPA complexes was applied to glow-discharged Quantifoil 2/1 200-mesh gold holey carbon grids, which were blotted for 3 s under 100% humidity at 12 °C. The grids were flash-frozen in liquid ethane using a FEI Mark IV cryo-plunge instrument.

Cryo-EM data were collected on a 300 kV FEI Titan Krios microscope operated in correlated double sampling mode. Images were acquired on a K3 Summit direct detector (Gatan) at a magnification of 29,000 \times , corresponding to a pixel size of 0.4027 Å per pixel in super-resolution mode. Images were collected using 'multi-shot' and 'multi-hole' methods customized in SerialEM⁴⁶, permitting the acquisition of six videos per hole, from nine neighbouring holes (3 \times 3) per stage shift. Nominal defocus values ranged from -1.2 μ m to -2.0 μ m. Each raw video stack consists of 60 frames, collected at a dose rate of around 6.8 e⁻ per pixel per s, for a total exposure time of 4.7 s resulting in a total dose of 50 e⁻ Å⁻² (Supplementary Table 1).

Image processing

We collected 46,927 super-resolution videos that were binned to a pixel size of 0.8055 Å per pixel. Beam-induced motions were corrected by patch motion correction (multi), and contrast transfer function (CTF) parameters were estimated by patch CTF estimation (multi) using cryoSPARC v.2.14⁴⁷. Two image-distinct processing strategies, deemed 1 and 2, were conducted in parallel.

Data-processing strategy 1. Blob picker in cryoSPARC was used to pick particles from around 7,000 micrographs to generate two-dimensional class averages with clear receptor features. A subset of these class averages was then used as templates for template-based picking from all 46,927 micrographs. Particles were extracted and downsampled to a box size of 128 \times 128 pixels and subjected to several rounds of two-dimensional classification. Only classes showing clear receptor features were kept, which resulted in the retention of 2,893,667 particles. Next, three-dimensional classification was performed in RELION 3.0⁴⁸, using a sampling interval of 15° without masking or imposed symmetry, yielding three classes (1a, 1b and 1c) displaying canonical receptor features with two 15F1 Fabs in the B/D positions and two 11B8 scFvs in the A/C positions at the ATD layer. Particles from classes 1b and 1c were combined and refined, while particles from class 1a were flipped 180° along the x axis to correct for an 'upside down' orientation, before being refined separately. Particles from these two refinements (1b + 1c and 1a) were separately re-centred and re-extracted at a box size of 256 \times 256. The two re-centred particle sets were classified into 10 and 12 classes, respectively. Classes displaying receptors labelled with the same antibody fragment densities were combined into a single-particle stack and subjected to another round of classification. From this round of classification, we sorted receptors bound with the same Fab and scFv combination into two separate orientations of the ATD layer: symmetric (S) and asymmetric (AS). Particles from this round of classification were sorted into six groups based on the ATD labelling and orientations: A1A2A1A2 (S), A1A2A1A2 (AS), A1A2A3A2 (AS1), A1A2A3A2 (AS2), A1A2A3A2 (AS3), A3A2A3A2 (S) and A3A2A3A2 (AS).

We combined classes with the same ATD labelling and orientation and performed ATD-focused classification without any symmetry imposed on each group. For the A1A2A1A2 (S) class, the ATD layer was sub-classified into eight classes, of which one class occupying the largest population (55%) had the least well resolved secondary structure features. Another round of ATD focused classification was performed on this class, producing an A1A2AXA2 subtype, where 'X' represents the subunit that was not labelled by any of the antibody fragments. From the remaining classes, three classes showing the most well-defined secondary structure features were selected for final refinement with C2 symmetry using cryoSPARC⁴⁹, producing a map at a global resolution of 4 Å. To improve the map density in the ATD, we carried out ATD-focused refinement with C2 symmetry and obtained an ATD-A1A2A1A2 (S) map at a resolution of 3.4 Å. The same procedures were performed on classes corresponding to the other subtypes, with the exception that C2 symmetry refinement was imposed on only the A3A2A3A2 (S) group.

Data-processing strategy 2. All image processing was performed in cryoSPARC⁴⁷. Motion-corrected, dose-weighted micrographs were curated by eliminating micrographs that showed imaging defects including excessive drift, broken holes or CTF estimation worse than 10 Å, resulting in 44,419 micrographs for further processing. Blob picker was used on a small subset of the data to generate two-dimensional templates with distinguishable receptor features. These two-dimensional templates consisted of a range of orientations and were used for interactive and automated particle picking using template-based picking. This resulted in 6,002,517 putative particles, which were initially extracted in a 256 \times 256 box.

To remove images of ice, carbon support and other debris, two-dimensional and three-dimensional classifications were used to sort particles. First, three-dimensional classification without masking or symmetry was implemented to sort particles. Two rounds of three-dimensional classification were used to remove featureless particles by keeping only classes with discernible receptor features. This strategy was used to retain the maximum number of 'good' particles so that receptor subtypes with low populations could be resolved in subsequent processing steps. After sorting by three-dimensional classification, 4,523,669 particles remained. This particle stack was then subjected to two rounds of reference-free two-dimensional classification to eliminate poorly resolved particles, and resulted in a stack of 1,844,956 particles.

To resolve different receptor subtypes, the stack of 1,844,956 particles was subjected to multiple rounds of three-dimensional classification. First an initial three-dimensional reconstruction was performed in cryoSPARC⁴⁷ without symmetry imposed to generate maps of several different AMPAR subtypes. These maps were used as initial references to sort particles by subtype using heterogeneous refinement in cryoSPARC⁴⁷. Multiple rounds of three-dimensional classification were conducted, each time using maps from the previous run as new initial models. This enabled the separation of receptor subtypes, as well as sub-classification of symmetric and asymmetric receptors within these subtypes. Receptor subtypes were distinguished based on inspection of the ATD layer using the visualization and orientation of the 11B8 scFvs and the 15F1/5B2 Fabs. This strategy resulted in the elucidation of six different subtypes, A1A2A1A2 (S/AS), A3A2A3A2 (S/AS) and A1A2A3A2 (AS1/AS2). Notably, data-processing strategy 2 did not uncover the A1A2AXA2 or the A1A2A3A2 (AS3) subtype. This was because focused classification of the ATD layer was not used, and the strategy was therefore unlikely to separate and resolve these low-populated classes. We suspect that with data-processing strategy 2, particles corresponding to these two subtypes are mixed within the other classes. Nevertheless, the percentages of particles of all of the remaining three-dimensional classes and associated receptor subtypes were approximately the same for both processing strategies (Supplementary Table 2).

In all of the maps solved for the full receptor complexes, density in the LBD–TMD region was much weaker compared to the ATD layer. Therefore, using the maps solved from data-processing strategy 1, we used focused classification of the LBD–TMD layer for each AMPAR subtype to improve the resolution of this region. Examination of the A1A2A1A2 (S/AS) maps revealed the same LBD–TMD stoichiometry and secondary structure. We therefore performed focused three-dimensional classification on particles combined from both conformations. Using a soft mask around the LBD–TMD layer and imposing C2 symmetry, classification in RELION 3.0⁴⁸ resulted in three classes (classes 1, 7 and 8) that displayed continuous transmembrane helical densities. Classes 1 and 8 were selected for further classification focused on the LBD–TMD layer. Classes with strong density for the transmembrane domain and auxiliary proteins were combined for a final refinement in cryoSPARC⁴⁹, resulting in a map of the LBD–TMD layer at a resolution of 3.63 Å by the gold-standard Fourier shell correlation (FSC) (0.143). In this map, auxiliary protein densities in the B'/D' positions show prominent extracellular protrusions that were well fit by TARP-γ8 (PDB code: 6QKC) whereas densities in the A'/C' positions displaying minimal extracellular features were well fit by CNIH3 (PDB code: 6PEQ). We note that TARP-γ2, TARP-γ3 and TARP-γ4 are also present in the hippocampus and speculate that we did not isolate a substantial number of these complexes because the JNJ compound specifically stabilizes the TARP-γ8 complex. We then performed the same focused classification procedure on the LBD–TMD layers of the A1A2A3A2 and A3A2A3A2 maps from data-processing strategy 1. First, C1 symmetry was imposed on the LBD–TMD–A1A2A3A2 map, followed by refinement with either C1 or C2 symmetry, yielding two maps at a resolution of 4.8 Å and 4.0 Å, respectively. The refined LBD–TMD–A1A2A3A2 maps, with either C1 or C2 symmetry, displayed the same auxiliary protein stoichiometry as that of the LBD–TMD_{A1/A2} complex, with two TARP-γ8 proteins in the B'/D' positions and two CNIH2 proteins in the A'/C' positions. The final LBD–TMD map from the A3A2A3A2 subtype was refined to a resolution of 7.7 Å (C2 symmetry), and displayed discontinuous densities for the transmembrane helices of the receptor and weak densities of the auxiliary proteins. This lack of resolution is likely limited by the number of particles from the A3A2A3A2 subtype. Resolutions reported in Supplementary Table 1 are global estimated by gold standard FSC 0.143 criteria and local resolution estimations were calculated using ResMap⁴⁷. Because the only resolvable arrangement of auxiliary proteins from all of the AMPAR subtypes appeared to be the same, we used an additional strategy aimed at improving resolution of the LBD–TMD layer, as described below.

The stack of 1,844,956 particles from data-processing strategy 2 was first extracted to a box size of 548 × 548 pixels and then downsampled to 400 × 400 pixels. A consensus refinement was generated from these particles using homogenous refinement, followed by non-uniform refinement in cryoSPARC⁴⁹. Using this map, a mask was generated around the ATD layer, including all possible locations for the three antibodies. This mask was used to subtract the ATD layer and antibody features from the consensus refinement, using signal subtraction in cryoSPARC⁴⁷. This new dataset containing only the LBD–TMD layer underwent two iterations of reference-free two-dimensional classification, resulting in 954,539 particles. This stack of 954,539 particles was separated into 10 classes using three-dimensional heterogeneous refinement without imposition of symmetry. One class consisting of 151,141 particles was selected for refinement, as it displayed density for continuous helices within the micelle, including density for TARP-γ8 in the B'/D' positions and CNIH2 in the A'/C' positions, equivalent to the stoichiometry observed in the LBD–TMD maps solved using focused classification (Supplementary Table 1). Refinement of this single class was performed in cryoSPARC consisting of a four-step, iterative procedure described in Extended Data Fig. 13. This procedure was iterated twice, resulting in a map at 3.45 Å resolution. To further improve the map, *ab initio* three-dimensional classification was performed without

symmetry imposed to remove 'junk' particles. One class showed clear features of the LBD–TMD layer, whereas the other classes were uninterpretable. The best class consisting of 132,427 particles was then subjected to the four-step refinement procedure described above, resulting in a 3.26 Å map by the gold-standard FSC (0.143).

The metadata and particle stack from the 3.26 Å map were then imported into RELION 3.0⁴⁸ for further classification. Particles were sorted using three-dimensional classification without alignment (C1 symmetry, $T = 50$, loose mask) to remove junk particles. Of the eight classes, six displayed uninterpretable density (4%), one class showed clear secondary structure, but resolving only to around 8 Å resolution (8%), and the remaining class showed density for side chains and improved density features for the helical-like density that we surmise is SynDIG4 (88%). This class of 116,710 particles was re-imported into cryoSPARC for a final refinement that resulted in a final resolution of 3.25 Å (B -factor = 62.1) by the gold-standard FSC (0.143). The cryo-EM density from this map, called the LBD–TMD_{mix} map, was visualized in UCSF Chimera⁵⁰.

Model building

The ATD–Fab/scFv layers of the A1A2A1A2 (S) and A1A2A1A2 (AS) density maps were first rigid-body fitted with the structure of the ATD–Fab/scFv layers, including the carbohydrate groups, extracted from A1A2A1A2 (PDB code: 6NJL) using UCSF Chimera⁵⁰. The resulting structures were manually adjusted in Coot⁵¹, guided by well-resolved side-chain densities and further refined by real-space refinement using Coot⁵¹ and Phenix⁵², yielding map to model cross-correlation values for the ATD–Fab/scFv layers of A1A2A1A2 (S) and A1A2A1A2 (AS) of 0.74 and 0.77, respectively.

For the LBD–TMD_{A1/A2} map, we first rigid-body fitted the recombinant dimeric GluA1–GluA2–TARP-γ8 complex (PDB code: 6QKC) into the density. A homology model of CNIH2 was built using the CNIH3 subunit extracted from the homomeric GluA2–CNIH3 complex (PDB code: 6PEQ). This model was rigid-body fitted to the map in Phenix⁵². On the basis of inspection of the density, we assigned TARP-γ8 and CNIH2 to the density in the B'/D' and A'/C' positions, respectively. Notably, flip/flop splicing sites and the R/G editing sites are interpretable in our maps and we assigned the flip/R and flop/R sequences for these two sites to GluA1 and GluA2, respectively, and built glutamine and arginine in the Q/R sites for the GluA1 and GluA2 subunits, respectively. Coordinates for MPQX were extracted from a previously solved GluA2 crystal structure (PDB code: 3KG2) and placed into the well-defined densities as appropriate. The simplified molecular-input line-entry system (SMILES) string of JNJ-55511118 was imported into Coot⁵¹ to generate the structure of JNJ-55511118, followed by manual fitting into the corresponding densities. Because the prominent tube-shaped electron density surrounding the transmembrane domain of the receptor and the auxiliary proteins are probably from ordered lipid molecules, we fit these densities with alkane chains of complementary lengths. Notably, at the cytosolic boundary of the A'/C' positions, a single lipid molecule, denoted OCT906, bridges residues Val69 and Ser73 from TM2 with Ile573 from the M2 helix of GluA2. The resultant structure was manually adjusted in Coot⁵¹, guided by well-defined side-chain densities from both the receptor and auxiliary protein densities. Subsequently, the structure was refined by real-space refinement in Coot⁵¹ and by Phenix⁵², placing restraints on clearly defined secondary structure elements and the appropriate non-crystallographic symmetry, yielding a map to model cross-correlation of 0.77. This structure was used as the initial model for building the LBD–TMD_{mix} map. Comparisons of the LBD dimers between the LBD–TMD_{A1/A2} and the GluA2–CNIH3 structures were done by superimposing the B/C LBD dimers and calculating the r.m.s.d. of the Cα atoms between these two dimers, and the change in the centre of mass (COM) from the opposing A/D LBD dimers in PyMOL⁵³. Comparisons of the TMD layers between the LBD–TMD_{A1/A2} and the GluA2–CNIH3 structures were carried out by superimposing

the two models, followed by calculations of the r.m.s.d. between the C α atoms of the M1, M3 and M4 helices in PyMOL⁵³.

The LBD–TMD_{A1/A2} model was used as a starting point to generate coordinates for the LBD–TMD_{mix} model. In brief, the LBD–TMD_{A1/A2} model was first docked into the cryo-EM density of the LBD–TMD_{mix} map by rigid-body fitting using Chimera⁵⁰. Next, the auxiliary proteins were rigid-body fitted independently into the cryo-EM density. On the basis of four structures, the appearance of only GluA2 subunits in the B/D positions allowed us to define the occupancy of these positions by the GluA2 subunit. The A/C positions could be occupied by GluA1, GluA3 or GluA4, therefore, non-conserved side chains of these three subunits were modelled as alanines. The improved resolution of the LBD–TMD_{mix} map permitted the visualization of lipid densities and two prominent densities in the channel pore. Lipids were modelled as acyl chains unless the resolution permitted modelling of lipid head groups. The densities inside the channel are unmodelled, but we speculate that the density near the apex of the selectivity filter could be a Na⁺ ion. Ion–oxygen distances of around 2.6 Å from the carbonyl oxygen of R586 in the B and D positions are consistent with predicted distances of sodium-binding sites, as well as molecular dynamics simulations⁵⁴. The density toward the bottom of the pore could either be a Na⁺ ion or a water molecule, but is at insufficient resolution for speculation. The C-terminal domains of the AMPAR subunits and TARP- γ 8 are unmodelled. Automatic real-space refinement of the model was performed against one of the half-maps in Phenix with two-fold symmetry imposed⁵², with secondary structure and geometric restraints used to minimize overfitting. Manual rebuilding in Coot was alternated with automated refinement in Phenix. For cross-validation, FSC curves were calculated between the refined model and the LBD–TMD_{mix} half-map used for refinement. Regions that lacked sufficient resolution for accurate establishment of amino acids were modelled as polyalanines, such as the TM3–TM4 loop in CNIH2. Regions with weak or no density were not modelled and are indicated by dashed lines, which include the M1–M2 linker, the TMI–TM2 loop of CNIH2, and a considerable portion of the TARP- γ 8 extracellular region.

To generate the complete structures of the A1A2A1A2 (S) and A1A2A1A2 (AS) complexes, the refined models of the ATD–Fab/scFv–S/AS and LBD–TMD were fitted into their respective whole maps in Chimera⁵⁰ and manually adjusted in Coot⁵¹. All of the final models have good stereochemistry as evaluated by MolProbity score⁵⁵ (Supplementary Table 1). Figures were prepared using UCSF Chimera⁵⁰, UCSF ChimeraX⁵⁶ and PyMOL⁵³.

Patch-clamp recording

The DNA sequences encoding C-terminal GFP-tagged full-length rat GluA1 (flip, Q in the Q/R site) and C-terminal mCherry-tagged full-length rat TARP- γ 8 were cloned into a bicistronic BacMam vector for baculovirus transduction. Whole-cell recording was carried out in HEK293S GnTI⁻ cells 18–24 h after transduction with virus generated from the bicistronic GluA1–TARP- γ 8 construct. To minimize cell death, 30 μ M NBQX (2,3-dioxo-6-nitro-1,2,3,4-tetrahydrobenzo[*f*]quinoxaline-7-sulfonamide, Tocris) was added 5–6 h after infection. Pipettes were pulled to 2–4 M Ω resistance and were filled with an internal solution containing (in mM): 75 CsCl, 75 CsF, 5 EGTA and 10 HEPES, pH 7.3. The external solution contained (in mM): 160 NaCl, 2.4 KCl, 4 CaCl₂, 4 MgCl₂ and 10 HEPES, pH 7.3. Membrane voltage was held at –60 mV. The Axopatch 200B amplifier was used for data acquisition and pClamp 10 software was used for trace analysis. We chose 10 mM glutamate as a saturating concentration for the peak responses. As the receptor complex with TARP- γ 8 confers a slow augmentation of steady-state current during the application of glutamate, to reach a plateau of the steady-state current, we repeatedly applied glutamate for 1 s for a total of 10 times at an interval of 2 s. Only the steady-state current of the last application was used for data analysis. A concentration of 10 μ M JNJ-55511118 was applied before and during glutamate application for 1 s to measure the inhibition of glutamate-induced currents. Individual

cells were used only once for recording; no repeated measurements were taken from the same cell.

SiMPull

Coverslips and glass slides were extensively cleaned, passivated and coated with methoxy polyethylene glycol (mPEG) and 2% biotinylated PEG⁵⁷. A flow chamber was created by drilling 0.75-mm holes in the quartz slide and by placing double-sided tape between the holes. A coverslip was placed on top of the slide and the edges were sealed with epoxy, creating small flow chambers. A concentration of 0.25 mg ml⁻¹ streptavidin was then applied to the slide, allowed to incubate for 5 min, and washed off with T50 BSA buffer consisting of 50 mM Tris, 50 mM NaCl and 0.25 mg ml⁻¹ BSA, pH 8.0. Biotinylated anti-GluA2 15F1 monoclonal antibody at 10 μ g ml⁻¹ was applied to the slide, allowed to incubate for 10 min, and washed off with 30 μ l buffer A (20 mM Tris, pH 8.0, 150 mM NaCl, 0.075% (w/v) digitonin, 2 μ M MPQX and 2 μ M JNJ-55511118) supplemented with 0.2 mg ml⁻¹ BSA. Mouse brain supernatant, prepared as described in the ‘Isolation of native hpAMPA receptors’ section, was diluted either 1:600 to visualize GluA1-, GluA3-, TARP- γ 8- and SynDIG4-containing complexes, or 1:100 to visualize the less-abundant complexes with the GluA4 subunit. The supernatant was applied to the chamber, incubated for 5 min, and washed off with 30 μ l of buffer A. Detection antibodies were generated by labelling subunit- or auxiliary-protein-specific antibodies with NHS ester Alexa Fluor dyes. The labelling efficiency of all detection monoclonal antibodies was at least one dye per monoclonal antibody, as judged by comparison of the dye and antibody concentration after removal of unreacted dye. Fluorophore-labelled detection monoclonal antibodies were applied to the chamber for 5 min at a concentration of 1–3 μ g ml⁻¹, washed off with 30 μ l of buffer A, and the chamber was immediately imaged using a Leica DMi8 TIRF microscope with an oil-immersion 100 \times objective. Images were captured using a back-illuminated EMCCD camera (Andor iXon Ultra 888) with a 133 \times 133 μ m imaging area and a 13 μ m pixel size. This 13 μ m pixel size corresponds to 130 nm on the sample due to the 100 \times objective. To count GluA1, GluA3 and GluA4 subunits, the mean spot count per image and standard deviation were calculated from 90 total images collected from three separate chambers. The total number of complexes was calculated by adding the number of GluA1, GluA3 and GluA4 spots, and subtracting the number of colocalized GluA1 and GluA3 spots. Each SiMPull experiment included a negative control in a separate chamber in which the anti-GluA2 capture antibody was not applied but the other steps remained identical. The observed spot count from this chamber was used to estimate background fluorescence. The results of each SiMPull experiment are averaged across at least three independent samples from experiments conducted on at least two different days.

For single-molecule colocalization, two images were acquired in the same region of interest and the position of each molecule was calculated using a custom Python script. Molecules located within a four-pixel radius were considered to be colocalized. At least 12 images were averaged for each experiment. The colocalization of GluA4 with other subunits and auxiliary proteins was not calculated because of the low abundance of GluA4-containing receptors. To visualize complexes containing the GluA4 subunit, it was necessary to apply a high concentration of mouse brain supernatant, resulting in such a high spot density for other complexes so as to render counting individual complexes not possible.

Photobleaching videos were acquired by exposing the imaging area for 160 s. To count the number of TARP- γ 8 subunits, single-molecule fluorescence time traces of GFP-tagged anti-TARP- γ 8 Fab were generated using a custom Python script. Each trace was manually scored as having one to four bleaching steps or was discarded if no clean bleaching steps could be identified. This distribution of bleaching steps fits a binomial distribution for a dimeric protein on the basis of an estimated GFP maturation of 80%. A total of 600 molecules were evaluated from three separate videos. Scoring was verified by assessing the intensity

of the spot; on average, the molecules that bleach in two steps were twice as bright as those that bleach in one step.

Western blot analysis

Purified hippocampal AMPARs were loaded onto SDS–PAGE gels and transferred to a nitrocellulose membrane. Antibodies used for detection were anti-GluA1 (Millipore 04-823, 1:1,000), anti-GluA2 (Thermo Fisher PA5-19496, 1:1,000), anti-GluA3 (Invitrogen 32-0400, 1:1,000), anti-GluA4 (Millipore ab1508, 1:1,000), anti-PSD95 (Abcam ab-18258, 1:1,000) and anti-TARP- γ 8 and anti-CNIH2 (monoclonal antibodies generated in our laboratory (see ‘Generation and expression of the anti-TARP- γ 8 antibody’), 1:1,000). IRDye 800 CW anti-mouse/rabbit secondary antibodies were used for visualization. Blots were developed by adding secondary antibodies at a ratio of 1:10,000.

Animal use statement

For these experiments, 200 adult (6–8 weeks) C57BL/6 mice (both male and female) were ordered from Charles River Laboratories for hippocampal dissection. Previous experiments enabled us to determine the minimum number of mice sufficient for our study. No randomization, blinding or experimental manipulations were performed on these animals. All mice were euthanized under Institutional Animal Care and Use Committee (IACUC) protocols, consistent with the recommendations of the Panel on Euthanasia of the American Veterinary Medical Association (AVMA) and carried out only by members of the E.G. laboratory approved on IACUC protocol TRO1_IP00000905.

Cell line statement

Sf9 cells for expression of baculovirus are from Thermo Fisher (12659017, lot 421973). HEK293S GnT1⁻ cells (Ric15) for protein expression and electrophysiology studies are from a previously published study⁵⁸. The cells were not authenticated experimentally for these studies and tested negative for *Mycoplasma* contamination.

Reporting summary

Further information on research design is available in the Nature Research Reporting Summary linked to this paper.

Data availability

The cryo-EM maps and coordinates for overall, the ATD layer and the LBD–TMD layer of the A1A2A1A2 symmetric (S) and A1A2A1A2 asymmetric (AS) complexes have been deposited in the Electron Microscopy Data Bank (EMDB) under accession numbers EMD-23283 and EMD-23284 and in the Protein Data Bank (PDB) under accession codes 7LDD and 7LDE, respectively. The cryo-EM maps for overall, the ATD layer and the LBD–TMD layer of the A1A2A3A2 (AS1), A1A2A3A2 (AS2), A3A2A3A2 (S) and A3A2A3A2 (AS) complexes have been deposited in the EMDB under accession numbers EMD-23285, EMD-23286, EMD-23287 and EMD-23288, respectively. The cryo-EM maps of A1A2A3A2 (AS3) and A1A2AXA2 have been deposited in the EMDB under accession numbers EMD-23289 and EMD-23290, respectively. The cryo-EM map and coordinates for the LBD–TMD_{mix} complex have been deposited in the EMDB and PDB under accession codes EMD-23292 and 7LEP, respectively.

41. Penn, A. C. et al. Hippocampal LTP and contextual learning require surface diffusion of AMPA receptors. *Nature* **549**, 384–388 (2017).
42. Goehring, A. et al. Screening and large-scale expression of membrane proteins in mammalian cells for structural studies. *Nat. Protocols* **9**, 2574–2585 (2014).
43. Coleman, J. A., Green, E. M. & Gouaux, E. X-ray structures and mechanism of the human serotonin transporter. *Nature* **532**, 334–339 (2016).
44. Kawate, T. & Gouaux, E. Fluorescence-detection size-exclusion chromatography for precrySTALLIZATION screening of integral membrane proteins. *Structure* **14**, 673–681 (2006).
45. Sultan, F. A. Dissection of different areas from mouse hippocampus. *Bio-Protocol* **3**, e955 (2013).
46. Mastronarde, D. N. Automated electron microscope tomography using robust prediction of specimen movements. *J. Struct. Biol.* **152**, 36–51 (2005).
47. Punjani, A., Rubinstein, J. L., Fleet, D. J. & Brubaker, M. A. cryoSPARC: algorithms for rapid unsupervised cryo-EM structure determination. *Nat. Methods* **14**, 290–296 (2017).
48. Zivanov, J. et al. New tools for automated high-resolution cryo-EM structure determination in RELION-3. *eLife* **7**, e42166 (2018).
49. Punjani, A., Zhang, H. & Fleet, D. J. Non-uniform refinement: adaptive regularization improves single-particle cryo-EM reconstruction. *Nat. Methods* **17**, 1214–1221 (2020).
50. Pettersen, E. F. et al. UCSF Chimera—a visualization system for exploratory research and analysis. *J. Comput. Chem.* **25**, 1605–1612 (2004).
51. Emsley, P. & Cowtan, K. Coot: model-building tools for molecular graphics. *Acta Crystallogr. D* **60**, 2126–2132 (2004).
52. Afonine, P. V. et al. Real-space refinement in PHENIX for cryo-EM and crystallography. *Acta Crystallogr. D* **74**, 531–544 (2018).
53. The PyMOL Molecular Graphics System v.2.1 (Schrödinger, 2020).
54. Biedermann, J., Braunbeck, S., Plested, A. J. & Sun, H. Non-selective cation permeation in an AMPA-type glutamate receptor. *Proc. Natl Acad. Sci. USA* **118**, e2012843118 (2021).
55. Chen, V. B. et al. MolProbity: all-atom structure validation for macromolecular crystallography. *Acta Crystallogr. D* **66**, 12–21 (2010).
56. Goddard, T. D. et al. UCSF ChimeraX: meeting modern challenges in visualization and analysis. *Protein Sci.* **27**, 14–25 (2018).
57. Jain, A., Liu, R., Xiang, Y. K. & Ha, T. Single-molecule pull-down for studying protein interactions. *Nat. Protocols* **7**, 445–452 (2012).
58. Reeves, P. J., Callewaert, N., Contreras, R. & Khorana, H. G. Structure and function in rhodopsin: high-level expression of rhodopsin with restricted and homogeneous N-glycosylation by a tetracycline-inducible N-acetylglucosaminyltransferase I-negative HEK293S stable mammalian cell line. *Proc. Natl Acad. Sci. USA* **99**, 13419–13424 (2002).

Acknowledgements We thank the Pacific Northwest Cryo-EM Center (PNCC) and OHSU MMC for microscope use, D. Cawley, P. Streeter, Y. Zhong and N. Sheldon for generating antibodies, A. Goehring for mouse dissections, M. Mayer for his guidance and advice on electrophysiology experiments, J. Elferich for help writing SiMPull processing scripts, S. Chen for help initiating the project, L. Vaskalis for assistance with figures, F. Jalali-Yazdi and H. Owen for help with manuscript preparation and R. Nicoll and members of the Gouaux laboratory for discussions. PNCC is supported by NIH grant U24GM129547 and accessed through EMSL (grid.436923.9), a DOE Office of Science User Facility sponsored by the Office of Biological and Environmental Research. T.H. and J.M. were supported by the NIGMS grant R35GM122569. This work was supported by the NINDS grant R01NS038631 to E.G. T.H. and E.G. are investigators of the Howard Hughes Medical Institute. The content is solely the responsibility of the authors and does not necessarily represent the official views of National Institutes of Health.

Author contributions J.Y., P.R. and E.G. designed the project. J.Y. and P.R. performed the sample preparation for cryo-EM and biochemistry studies. J.Y. and P.R. performed the cryo-EM data collection, data analysis and model building. J.Y. performed the patch-clamp recording experiments. S.C. performed all of the SiMPull experiments with T.H. and J.M. providing training and comments. E.G., J.Y., P.R. and S.C. wrote the manuscript with input from T.H. and J.M.

Competing interests The authors declare no competing interests.

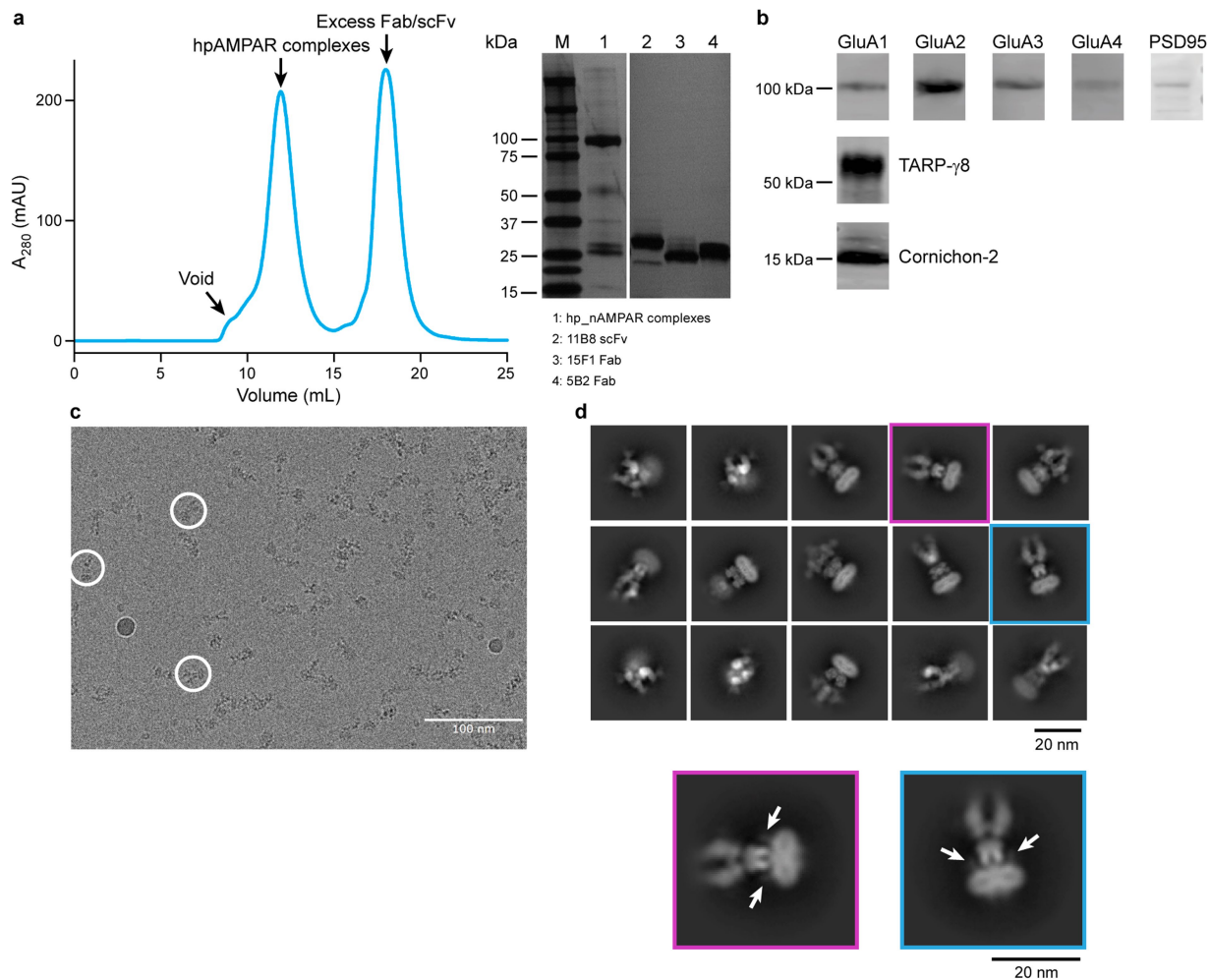
Additional information

Supplementary information The online version contains supplementary material available at <https://doi.org/10.1038/s41586-021-03540-0>.

Correspondence and requests for materials should be addressed to E.G.

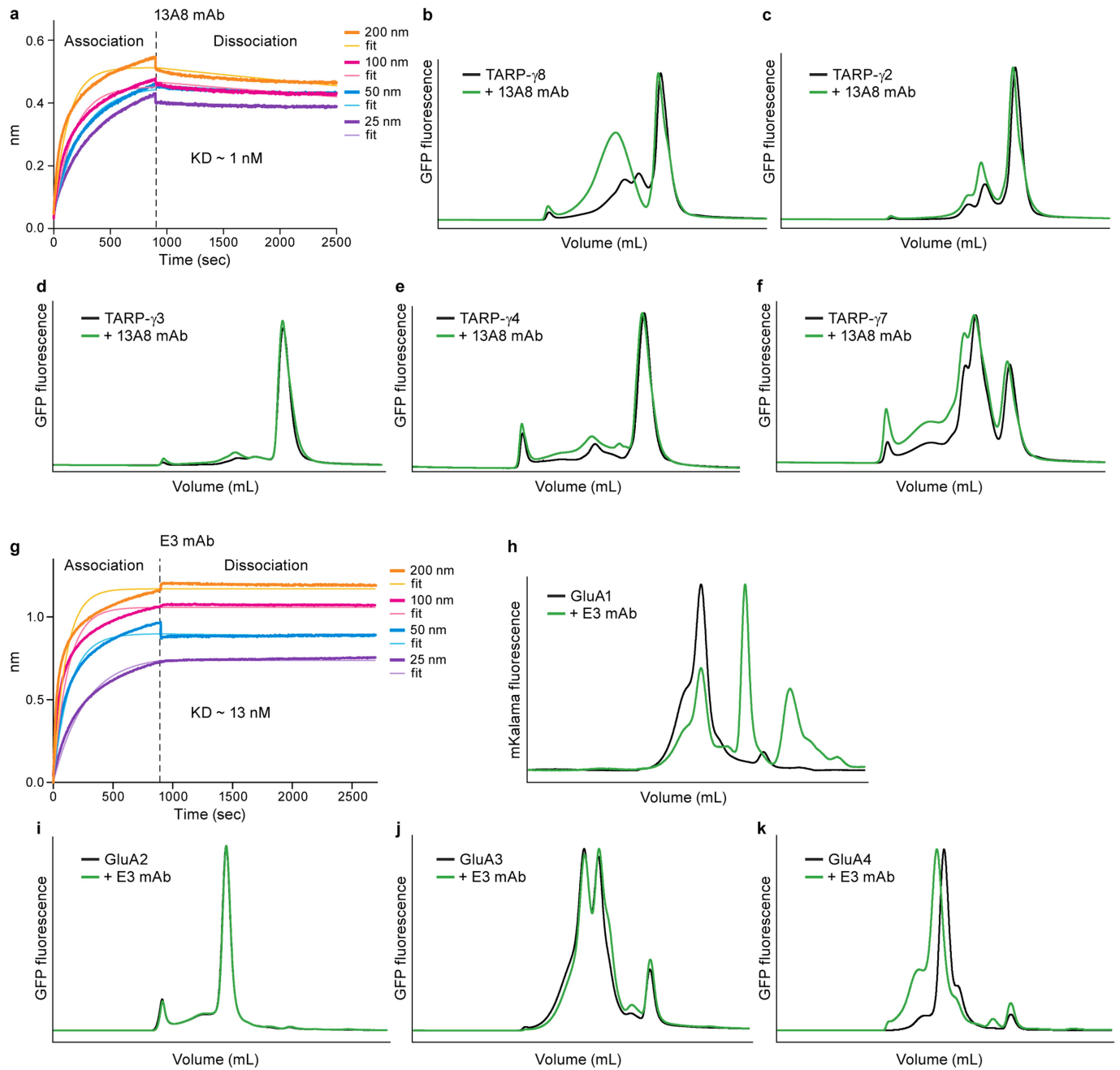
Peer review information Nature thanks Sudha Chakrapani, Vasanthi Jayaraman and Andrew Plested for their contribution to the peer review of this work. Peer reviewer reports are available.

Reprints and permissions information is available at <http://www.nature.com/reprints>.



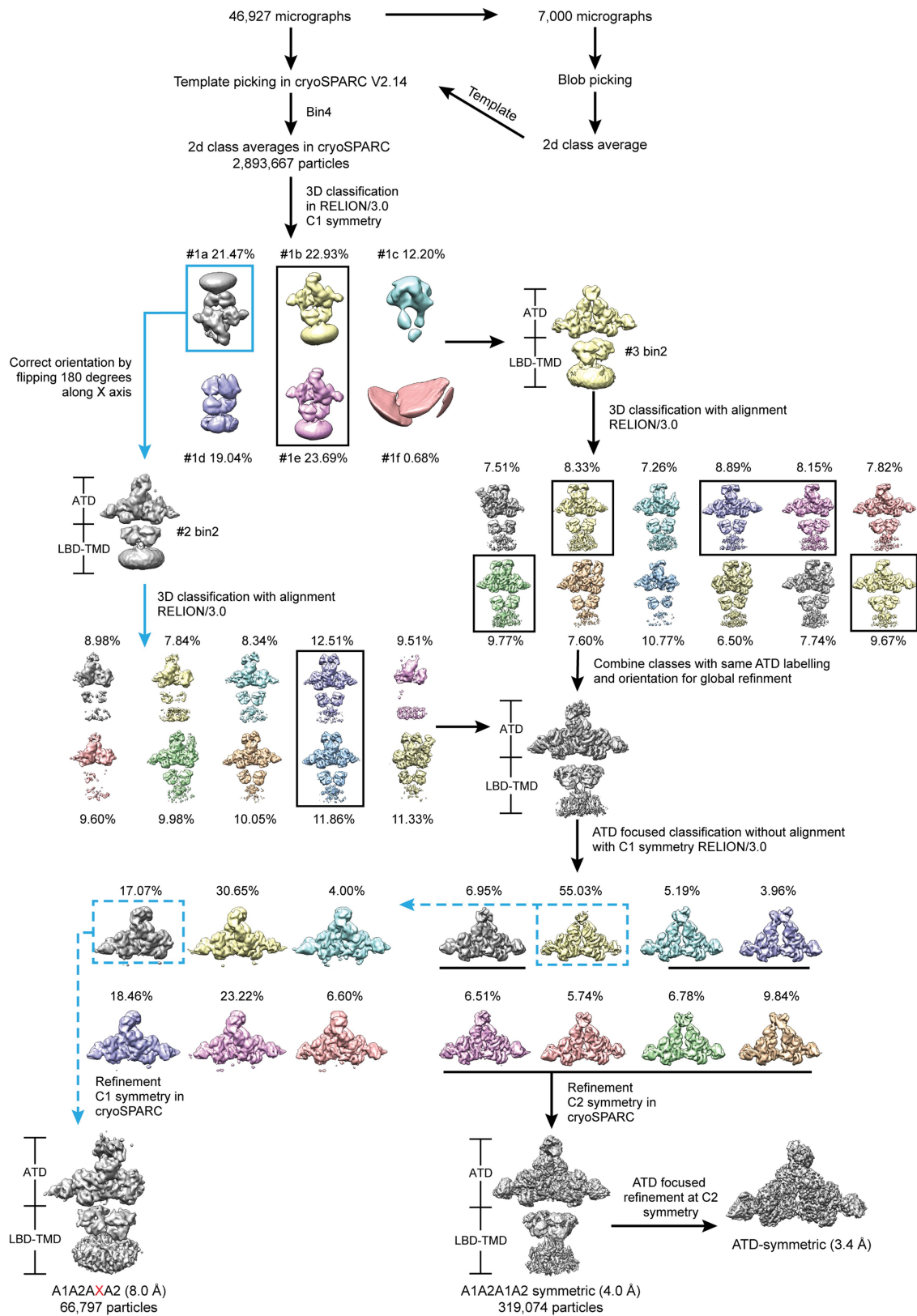
Extended Data Fig. 1 | Biochemical characterization and cryo-EM analysis of hpAMPA complexes. **a**, Representative SEC profile of hippocampal AMPAR complexes. Inset shows an SDS-PAGE gel of AMPAR complexes and antibody fragments used for cryo-EM grid preparation, visualized by silver staining. The gel was repeated three times from different batches of purification with similar results. **b**, Western blot analysis of isolated AMPAR complexes using antibodies against GluA1, GluA2, GluA3, GluA4, PSD95,

TARP-γ8 and CNIH2. The uncropped blot can be found in Supplementary Fig. 1 and blotting was repeated three times with similar results. **c**, A representative cryo-EM micrograph of hpAMPA complexes. The experiments were repeated four times with similar results. **d**, Selected two-dimensional class averages. Protrusions extending out of the detergent micelle are indicated by arrows, corresponding to the extracellular domain of TARP-γ8. Similar results were obtained from experiments repeated four times.



Extended Data Fig. 2 | Characterization of monoclonal antibodies 13A8 and E3. **a**, Octet measurements of the 13A8 monoclonal antibody binding to TARP- γ 8. Concentrations of the 13A8 monoclonal antibody ranging from 25 nM to 200 nM were applied. **b-f**, FSEC profiles of recombinant GFP-tagged TARP- γ 8 (b), TARP- γ 2 (c), TARP- γ 3 (d), TARP- γ 4 (e) and TARP- γ 7 (f) with 13A8 monoclonal antibody (green traces) and without 13A8 monoclonal antibody (black traces), detecting GFP fluorescence. Only the TARP- γ 8 trace is shifted by

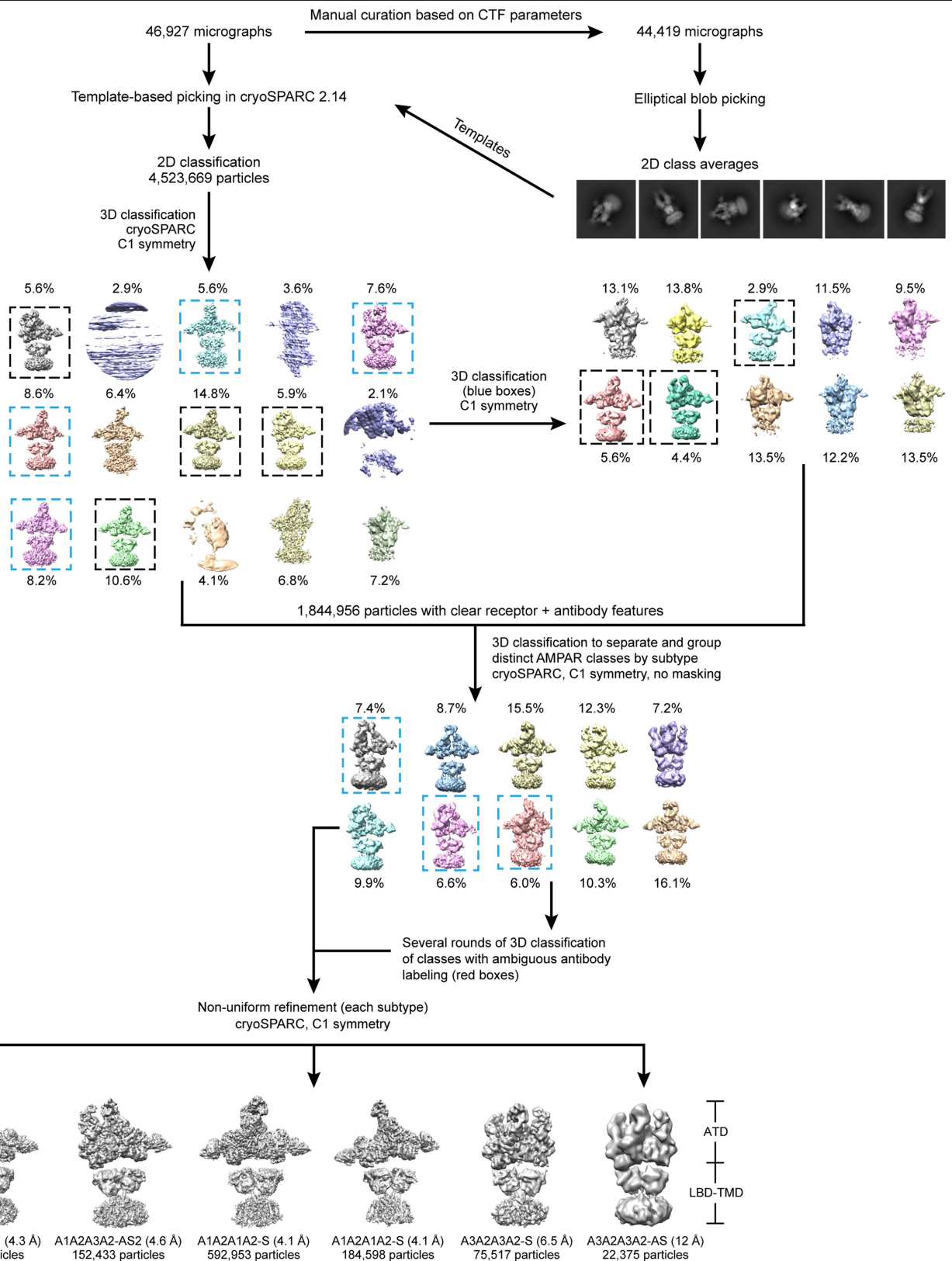
the 13A8 monoclonal antibody. **g**, Octet measurements of the E3 monoclonal antibody binding to GluA4. **h-k**, FSEC profiles of recombinant mKalamal-tagged GluA1 (h), GFP-tagged GluA2 (i), GFP-tagged GluA3 (j) and GFP-tagged GluA4 (k) with E3 monoclonal antibody (green traces) and without E3 monoclonal antibody (black traces), detecting mKalamal or GFP fluorescence. Only GluA4 receptors are shifted by the E3 monoclonal antibody.



Extended Data Fig. 3 | See next page for caption.

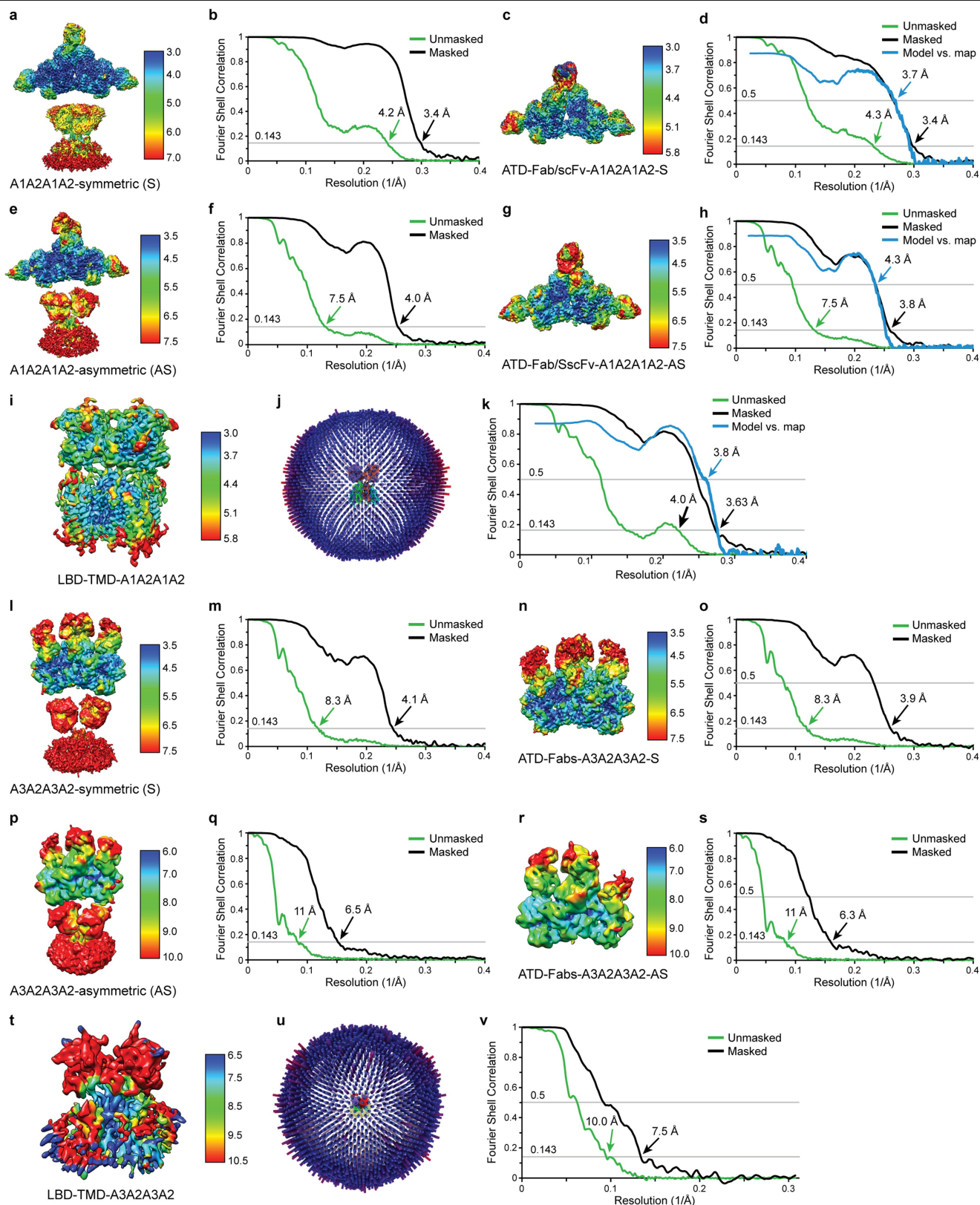
Extended Data Fig. 3 | A representative flow chart of data processing focused on the whole receptor and ATD layer using data-processing strategy 1. A total of 2,893,667 particles was picked from 46,927 motion-corrected micrographs in cryoSPARC v.2.14. Classes showing clear receptor features were kept after several rounds of two-dimensional classification, resulting in the retention of 2,893,667 particles. Next, three-dimensional classification with a large sampling degree was performed to further remove junk classes in RELION 3.0. Another round of three-dimensional classification was carried out to sort receptors with the same Fab and scFv combination. Classes with the same ATD labelling and orientation were combined and subjected to ATD-focused classification without alignment. For the A1A2A1A2

symmetric subtype, the ATD layer was classified into eight classes, of which one class, which occupied the largest population (55%), had the least well-resolved secondary structure features. Another round of ATD-focused classification was performed on this class, producing a subtype with one unlabelled subunit, denoted as A1A2AXA2. The three remaining classes showing the most well-defined secondary structure features were selected for final refinement with C2 symmetry, producing a map at a resolution of 4 Å. ATD-focused refinement with C2 symmetry was carried out to improve map density in the ATD, yielding an ATD–A1A2A1A2 symmetric map at a resolution of 3.4 Å.



Extended Data Fig. 4 | Data-processing workflow to determine AMPAR subtypes using data-processing strategy 2. Motion-corrected micrographs were first curated on the basis of ice thickness, motion correction, CTF fit and astigmatism. Template-based picking was used to autopick 6,002,517 particles in cryoSPARC v.2.14. To remove junk particles and false positives, multiple rounds of two-dimensional and three-dimensional classification were performed, selecting only classes that showed discernible receptor features,

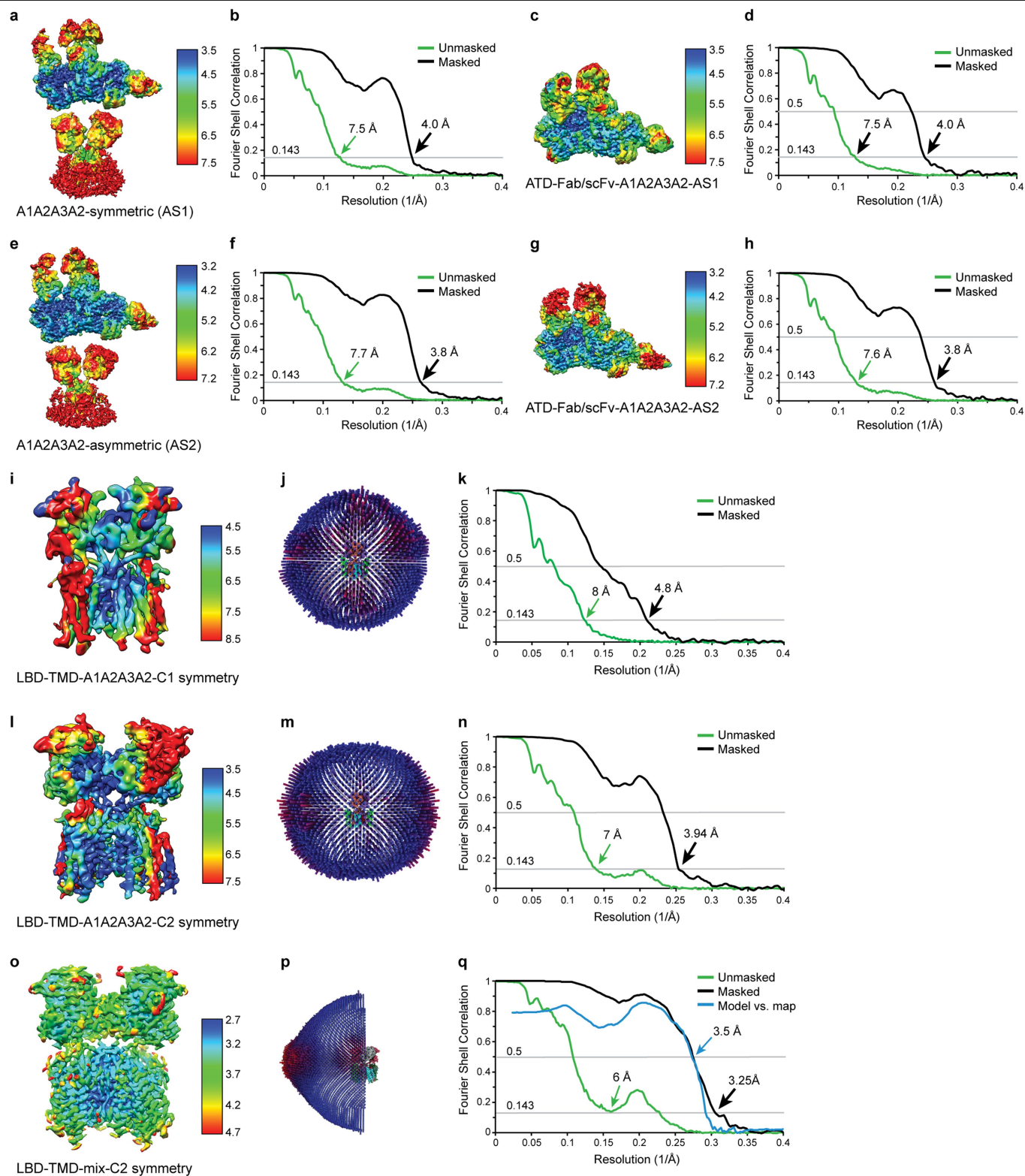
resulting in a particle stack of 1,844,956 particles. To sort receptors based on subtype (AMPA subunit stoichiometry and tilting), multiple rounds of three-dimensional classification were performed without symmetry imposed or masking. Particles from classes showing clear labelling with antibodies were grouped into distinct subtypes. Each of the AMPAR subtypes were refined separately. This strategy elucidated three different heteromeric AMPAR subtypes comprising both symmetric and asymmetric conformations.



Extended Data Fig. 5 | See next page for caption.

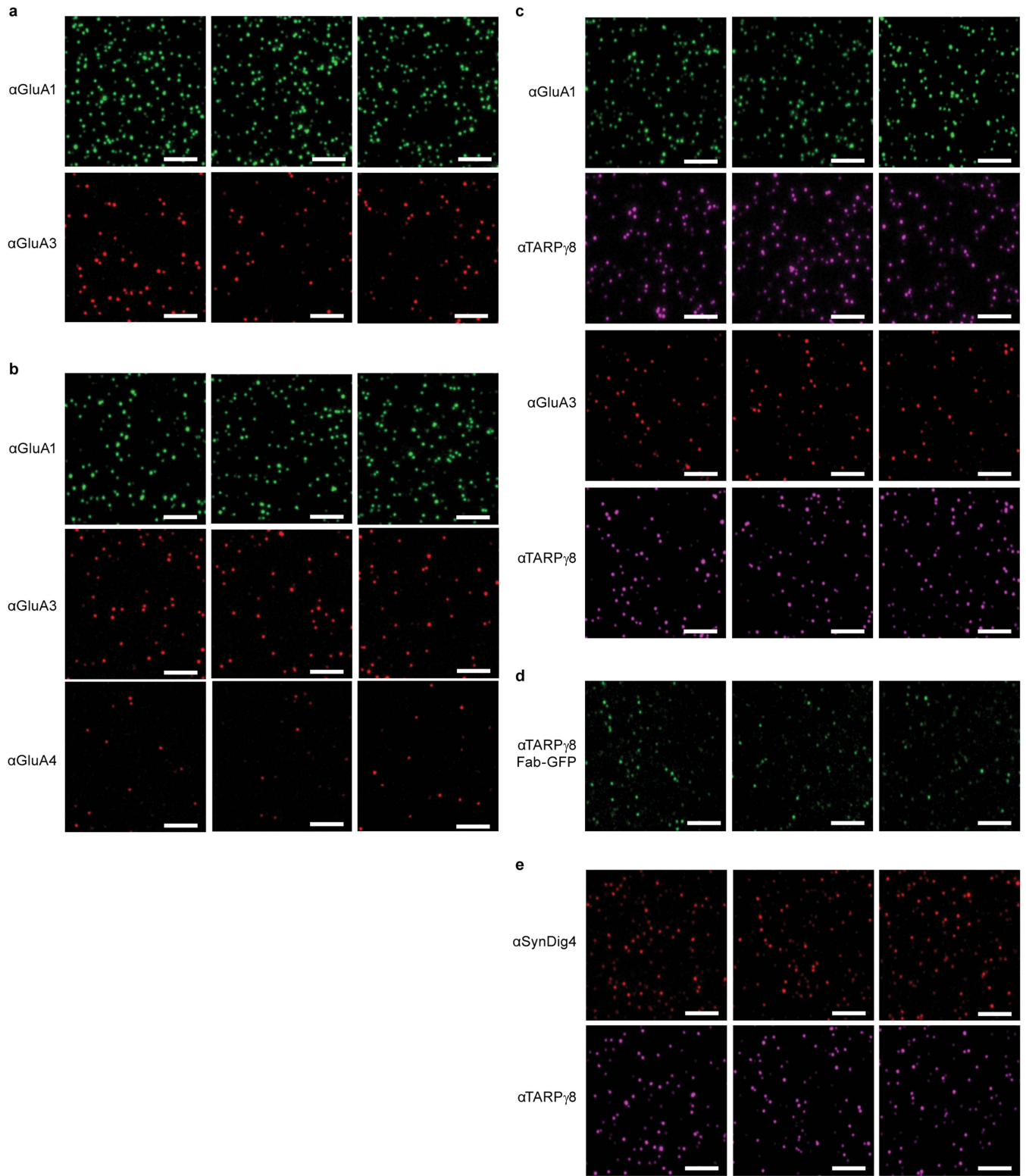
Extended Data Fig. 5 | Three-dimensional reconstructions of dimeric GluA1–GluA2 and dimeric GluA2–GluA3 complexes. **a, c, e, g, i,** Local resolution estimates of the entire GluA1–GluA2 symmetric map (**a**), ATD layer of the GluA1–GluA2 symmetric map (**c**), entire GluA1–GluA2 asymmetric map (**e**), the ATD layer of GluA1–GluA2 asymmetric map (**g**) and the LBD–TMD layers of the GluA1–GluA2 map (**i**). **d, h, k,** FSC curves before and after masking and between the model and the final maps of the ATD layer of the GluA1–GluA2 symmetric map (**d**), the ATD layer of the GluA1–GluA2 asymmetric map (**h**) and the LBD–TMD layers of the GluA1–GluA2 map (**k**). **j,** Angular distribution of the LBD–TMD layers of the GluA1–GluA2 map. **l, n, p, r, t,** Local resolution estimates

of the entire GluA2–GluA3 symmetric map (**l**), the ATD layer of the GluA2–GluA3 symmetric map (**n**), the entire GluA2–GluA3 asymmetric map (**p**), the ATD layers of the GluA2–GluA3 asymmetric map (**r**) and LBD–TMD layers of the GluA2–GluA3 map (**t**). **b, f, m, o, q, s, v,** FSC curves before and after masking of the whole GluA1–GluA2 symmetric map (**b**), the entire GluA1–GluA2 asymmetric map (**f**), the entire GluA2–GluA3 symmetric map (**m**), the ATD layer of GluA2–GluA3 symmetric map (**o**), the entire GluA2–GluA3 asymmetric map (**q**), the ATD layer of the GluA2–GluA3 asymmetric map (**s**) and the LBD–TMD layers of the GluA2–GluA3 map (**v**). **u,** Angular distribution of the LBD–TMD layers of the GluA2–GluA3 map.



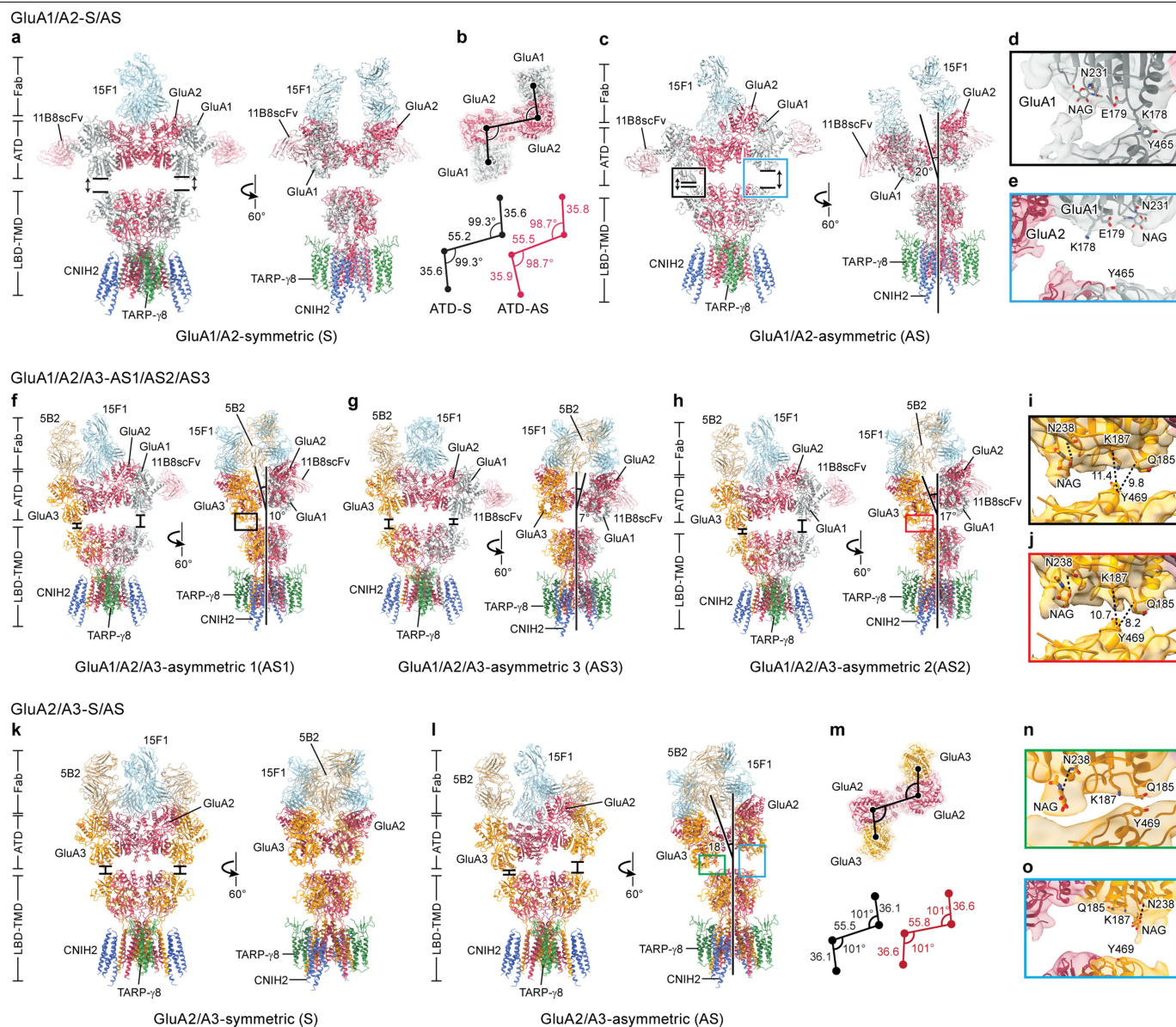
Extended Data Fig. 6 | Three-dimensional reconstructions of trimeric GluA1-GluA2-GluA3 complexes and the LBD-TMD_{mix} map. a, c, e, g, i, l, o. Local resolution estimates of the entire GluA1-GluA2-GluA3 asymmetric 1 map (a), the ATD layer of the GluA1-GluA2-GluA3 asymmetric 1 map (c), the entire GluA1-GluA2-GluA3 asymmetric 2 map (e), the ATD layer of the GluA1-GluA2-GluA3 asymmetric 2 map (g), the LBD-TMD layers of GluA1-GluA2-GluA3 without symmetry (i), the LBD-TMD layers of GluA1-GluA2-GluA3 with C2 symmetry imposed (l), and the LBD-TMD_{mix} map (o). **b, d, f, h, k, n, q.** FSC curves before and after masking the entire GluA1-GluA2-GluA3 asymmetric 1

receptor map (b), the ATD layer of the GluA1-GluA2-GluA3 asymmetric 1 map (d), the entire GluA1-GluA2-GluA3 asymmetric 1 map (f), the ATD layer of the GluA1-GluA2-GluA3 asymmetric 2 map (h), the LBD-TMD layers of GluA1-GluA2-GluA3 map without symmetry (k) and with C2 symmetry (n). **j, m, p.** Angular distribution of the LBD-TMD layers of the GluA1-GluA2-GluA3 maps with C1 symmetry (j) or C2 symmetry (m), and the LBD-TMD_{mix} map (p). **q.** FSC curves before and after masking and between the model and the final maps of the LBD-TMD_{mix} map.



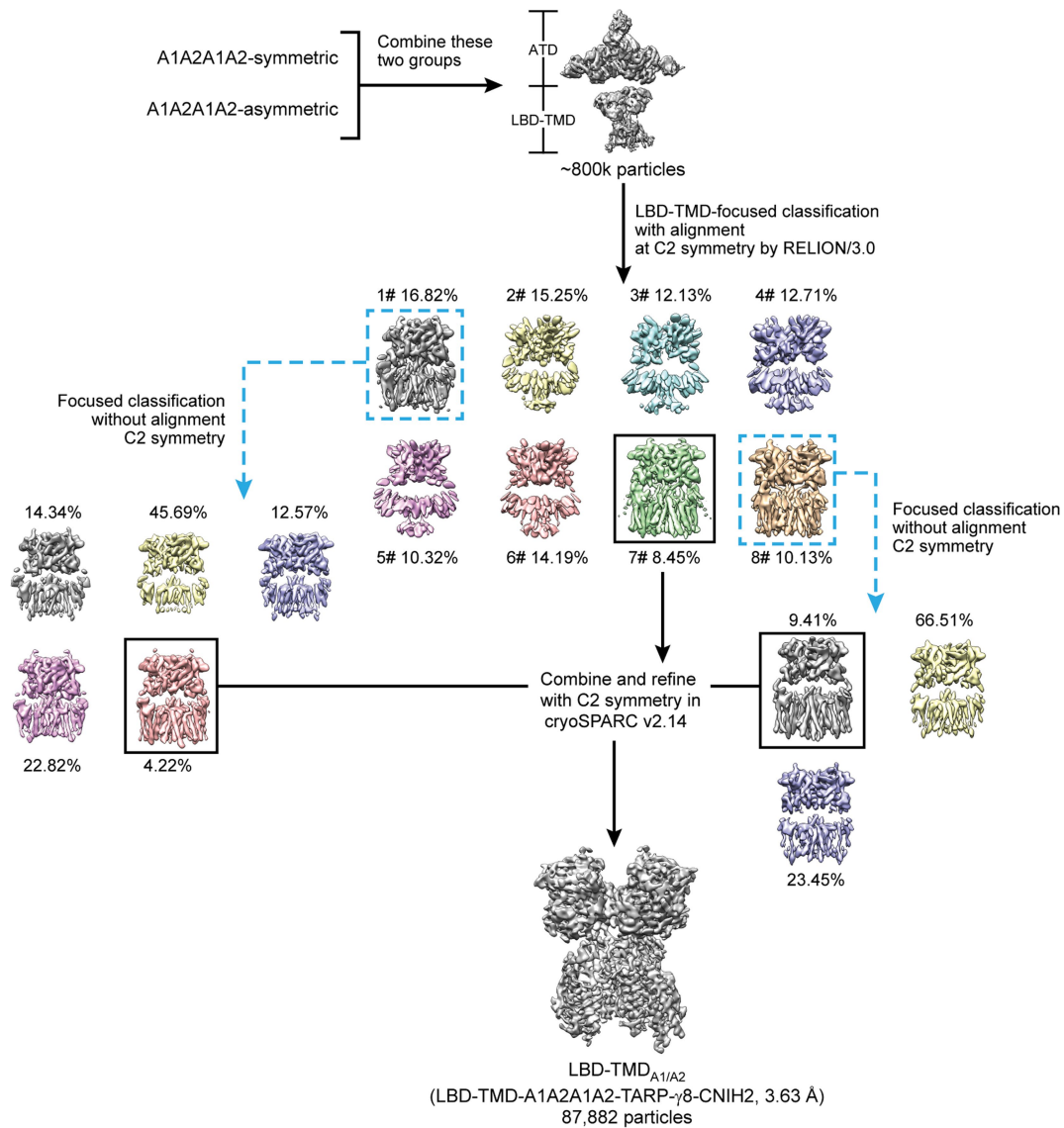
Extended Data Fig. 7 | Representative TIRF images for native AMPAR complexes captured with the 15F1 monoclonal antibody. a–e, Fluorescence detection with the anti-GluA1-Alexa488 monoclonal antibody (α GluA1) and anti-GluA3-Alexa594 monoclonal antibody (α GluA3) (a), the anti-GluA1-Alexa488 monoclonal antibody, anti-GluA3-Alexa594 monoclonal antibody and anti-GluA4-Alexa594 monoclonal antibody (α GluA4) (b), the anti-GluA1-Alexa488 monoclonal antibody, anti-GluA3-Alexa594 monoclonal

antibody and anti-TARP- γ 8 monoclonal antibody (α TARP- γ 8) (for each colocalization experiment) (c), anti-TARP- γ 8 (α TARP- γ 8) Fab-GFP (d) and the anti-SynDIG4-Alexa594 monoclonal antibody (α SynDIG4) and anti-TARP- γ 8-Alexa647 monoclonal antibody (α TARP- γ 8) (e). Scale bars, 5 μ m. For each SiMPull experiment, images were acquired from two independent samples on different days.



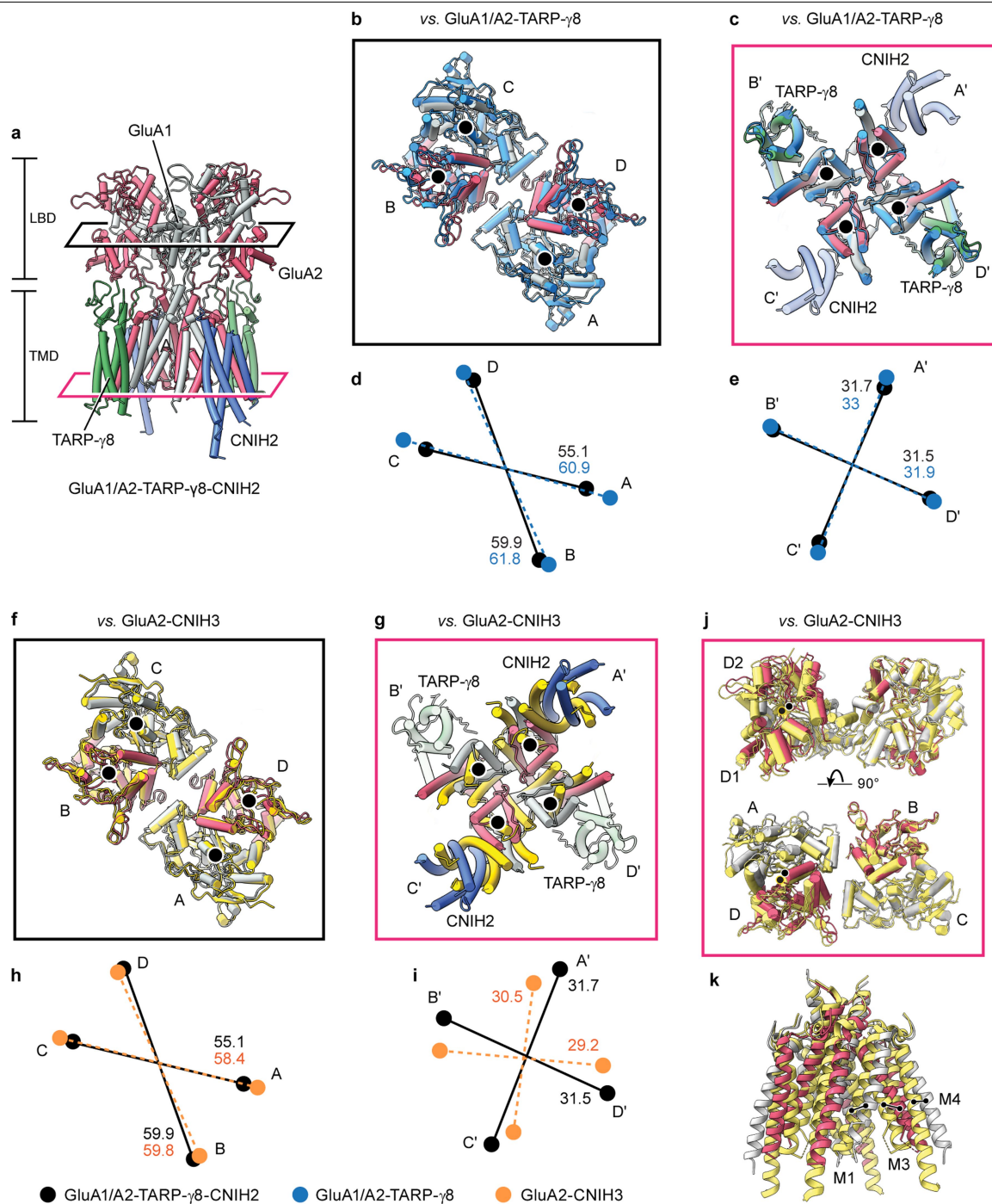
Extended Data Fig. 8 | Structures of the dimeric GluA1-Glu2 receptor, trimeric GluA1-Glu2-Glu3 receptor and dimeric GluA2-Glu3 receptor complexes in symmetric and asymmetric conformations. a, c, Cryo-EM structures of the GluA1-GluA2 subtype in symmetric (a) and asymmetric (c) conformations viewed parallel to the membrane. GluA1, GluA2, TARP- γ 8 and CNIH2 are shown in grey, red, green and blue, respectively. Antibody fragments 11B8 scFv and 15F1 Fab are shown in pink and cyan, respectively. **b,** ATD layer analysis of symmetric and asymmetric conformations. Top, the ATD model of the symmetric state, in which the centre of mass (COM) of each subunit is indicated by a black circle. Bottom, the distances (in Å) and angles determined by the COMs of the symmetric (left) and asymmetric (right) conformations. **d, e,** Close contacts between the ATD layer and LBD layer in the asymmetric conformations. Magnified views of the 'left' side (d) and 'right' side (e) of the ATD-LBD interfaces as indicated in the black and cyan rectangles. **f-h,** Cryo-EM structures of the trimeric GluA1-GluA2-GluA3 subtype in asymmetric conformations with different tilted angles and orientations

viewed parallel to the membrane. GluA1, GluA2, GluA3, TARP- γ 8 and CNIH2 are coloured in grey, red, orange, green and blue, respectively. Antibody fragments 11B8 scFv, 15F1 Fab, 5B2 Fab are shown in pink, cyan and light yellow colours, respectively. **i, j,** Magnified views of ATD-LBD interfaces in the asymmetric states (f, h) as indicated in the black and red rectangles. The distances are defined by the C α atoms of the indicated residues. **k, l,** Cryo-EM structures of the dimeric GluA2-GluA3 subtype in symmetric (k) and asymmetric (l) conformations viewed parallel to the membrane. **m,** The ATD layer analysis of the symmetric and asymmetric conformations. Top, the ATD model of the symmetric state. The COM of each subunit is shown as a black circle. Bottom, the distances (in Å) and angles determined by the COMs of the symmetric (left) and asymmetric (right) conformations. **n, o,** Close contacts between the ATD layer and LBD layer in the asymmetric conformations. Magnified views of the left side (n) and right side (o) of the ATD-LBD interfaces as indicated in the green and cyan rectangles.



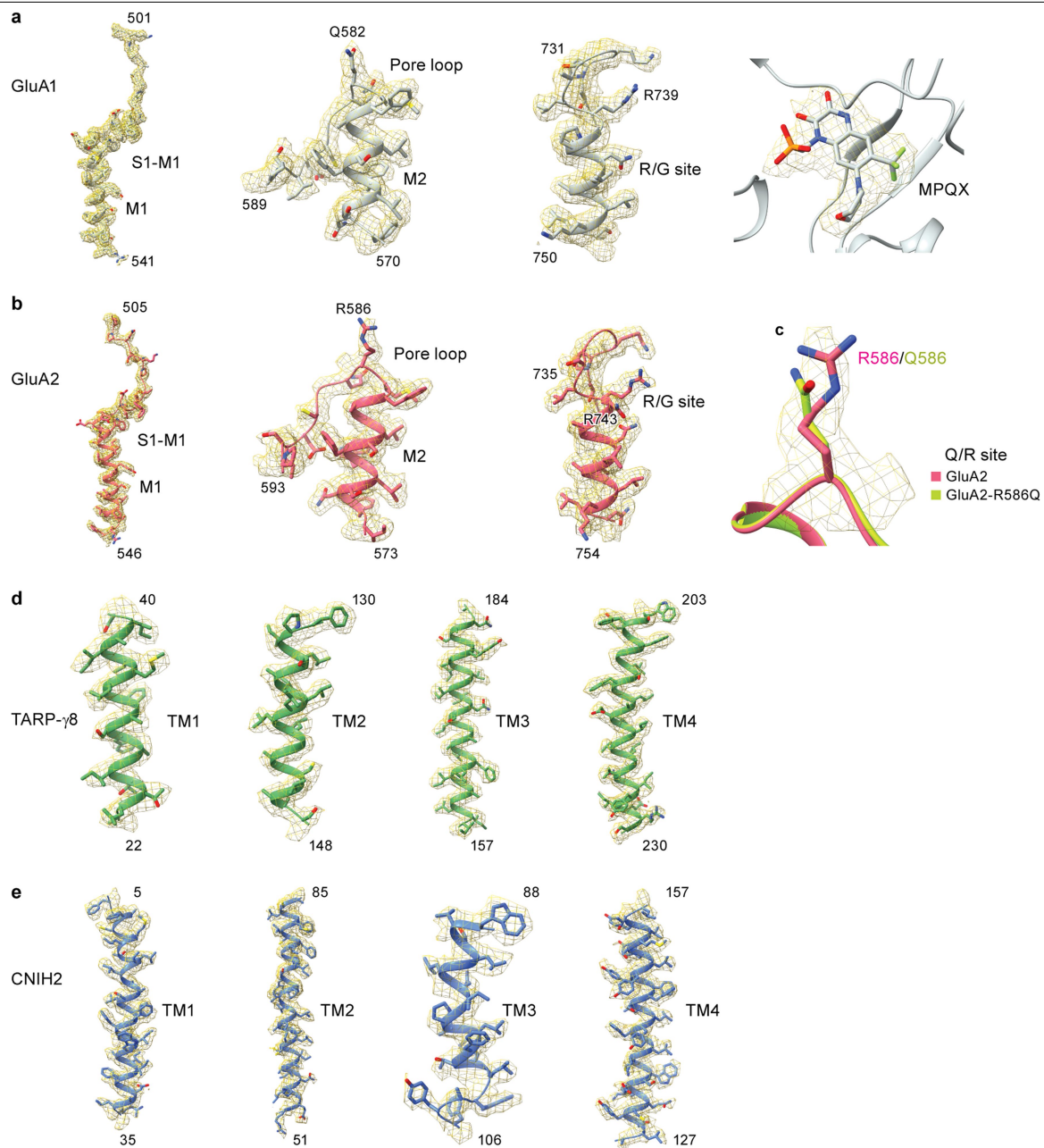
Extended Data Fig. 9 | Flow chart of data processing for hpAMPA complexes focused on the LBD-TMD layers. Particles corresponding to both the symmetric and the asymmetric GluA1-GluA2 subtypes were combined and subjected to LBD-TMD focused three-dimensional classification with alignment in RELION 3.0, resulting in three good classes with continuous

transmembrane helical densities. Another round of classification without alignment was carried out for classes 1 and 8. Classes displaying strong density for TMD and auxiliary proteins were combined for refinement in cryoSPARC v.2.14, yielding the LBD-TMD_{A1/A2} map at a resolution of 3.63 Å.



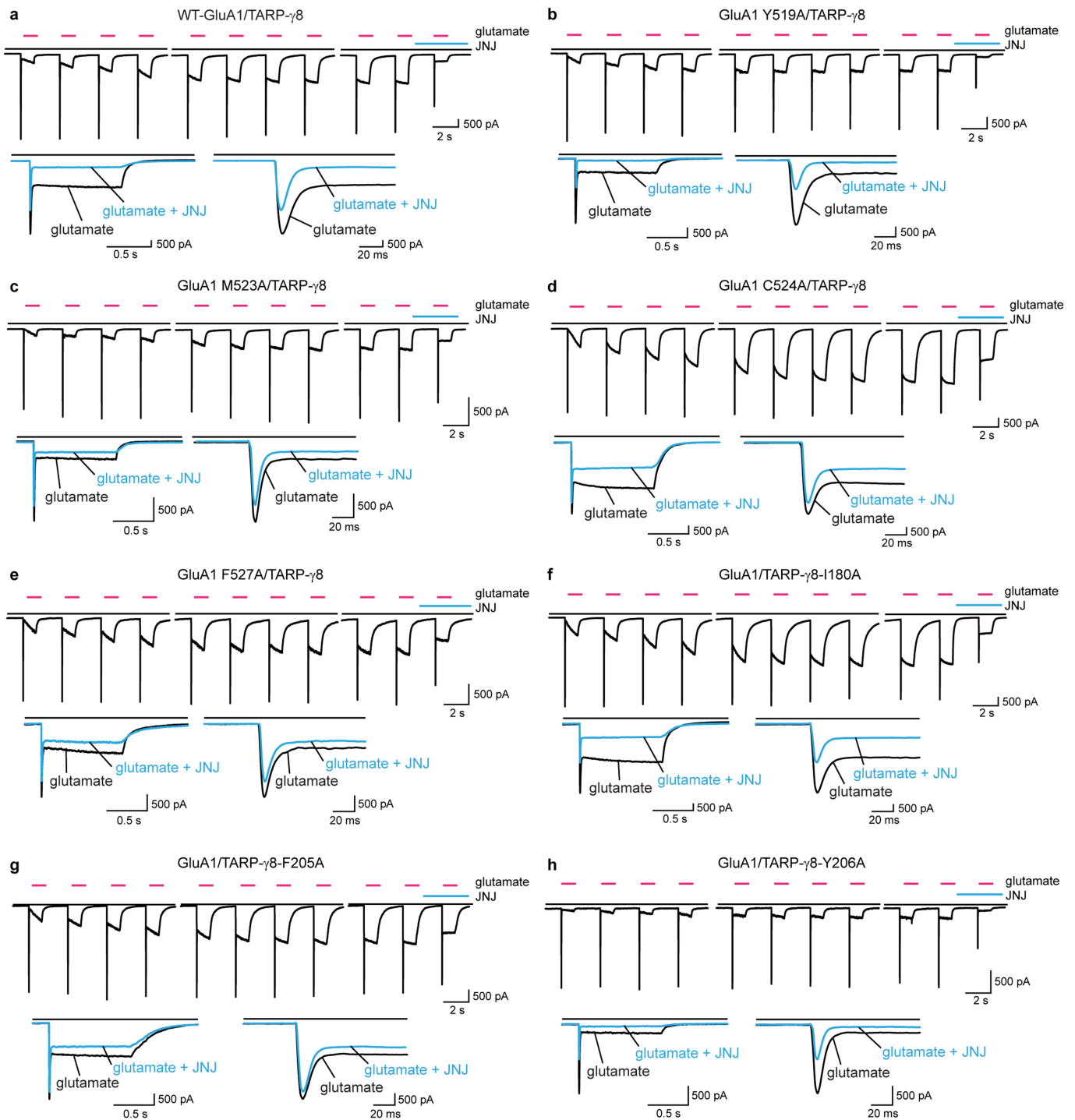
Extended Data Fig. 10 | Conformational differences in the LBD and TMD layers between native and recombinant AMPAR-auxiliary protein complexes. **a**, Reference model and orientation of the hippocampal LBD-TMD_{A1/A2} complex. GluA1, GluA2, TARP- γ 8 and CNIH2 are shown in grey, red, green and blue, respectively. **b–e**, Superposition of hippocampal LBD-TMD_{A1/A2} with recombinant GluA1-GluA2-TARP- γ 8 complexes (PDB code: 6QKC) to show the differences in the LBD (**b**, **d**) and TMD (**c**, **e**) layers. Recombinant GluA1-GluA2-TARP- γ 8 is shown in blue. COMs of LBD and TMD layers of each subunit are shown in coloured circles. The schematic diagrams illustrate the subunit arrangement differences in the distance (Ångstrom) of the LBD (**d**) and TMD (**e**) layers of these two complexes. **f–i**, Superposition of the hippocampal LBD-TMD_{A1/A2} structure with the recombinant GluA2-CNIH3 complex (PDB code: 6PEQ) to show the differences in the LBD (**f**, **h**) and TMD (**g**, **i**) layers.

Recombinant GluA2-CNIH3 is shown in yellow. COMs of the LBD and TMD layers of each subunit are shown in coloured circles. The schematic diagrams illustrate the subunit arrangement differences in the distance (Ångstrom) of the LBD (**h**) and TMD (**i**) layers of these two complexes. **j**, The B/C LBD dimers from the hippocampal LBD-TMD_{A1/A2} structure and the GluA2-CNIH3 complex (PDB code: 6PEQ) were superimposed, exhibiting a 3.2 Å shift in the COM (black circles) between the opposing A/D LBD dimers. **k**, Superposition of the M1, M3 and M4 helices of the hippocampal LBD-TMD_{A1/A2} structure with the recombinant GluA2-CNIH3 complex (PDB code: 6PEQ), highlighting the rotation and compression of the GluA2-CNIH3 TMD layer. Equivalent positions of the C α atoms from the M1 (Val538), M3 (Ile600) and M4 (Leu805) helices of the GluA2-CNIH3 structure are shifted by 4.5 Å, 5.7 Å and 4.7 Å, respectively.



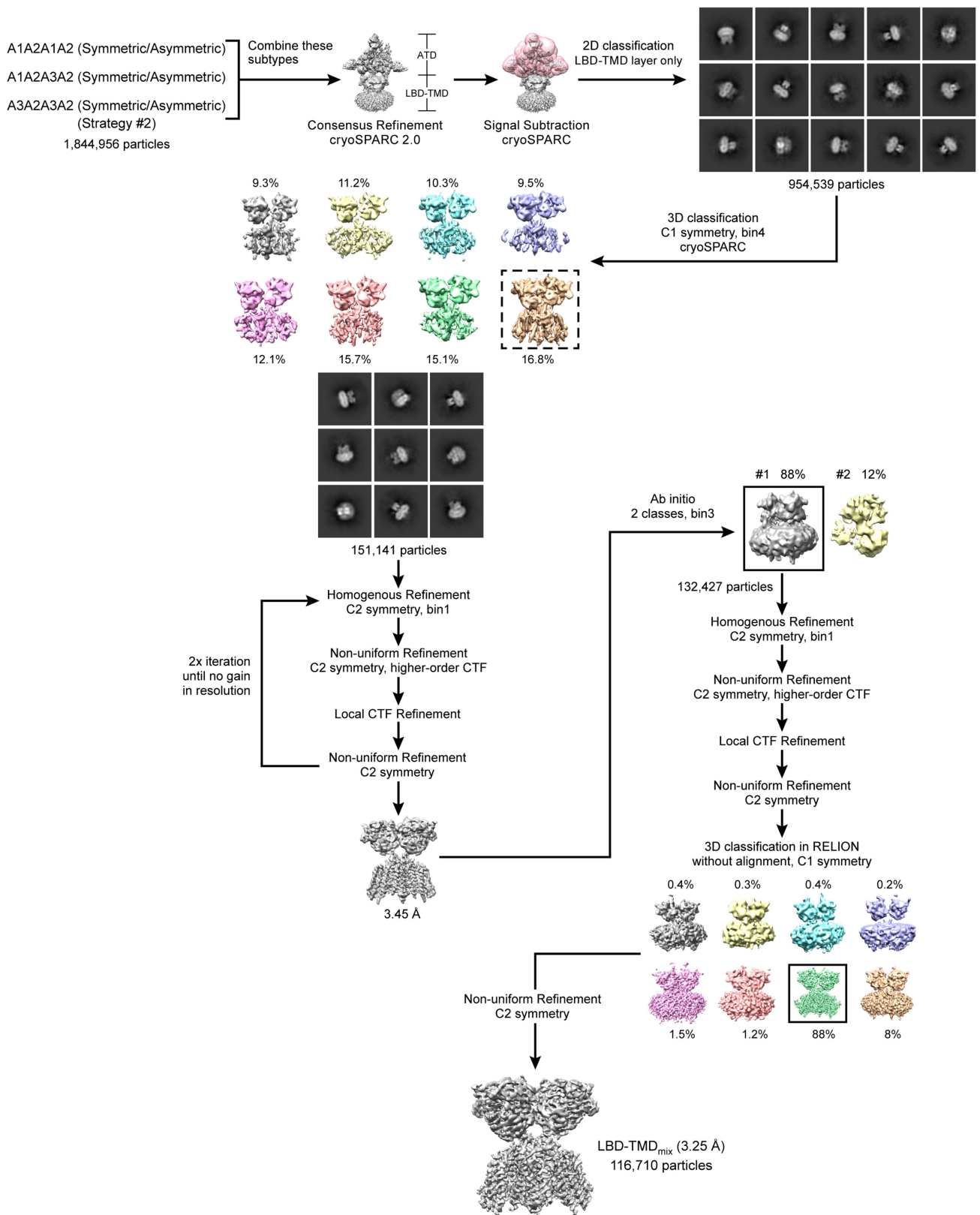
Extended Data Fig. 11 | Representative densities of the maps of the LBD-TMD_{A1/A2} or LBD-TMD_{mix} complexes. **a**, The S1-M1, M2-pore loop, R/G site and MPQX from GluA1 are isolated from LBD-TMD_{A1/A2}, contoured at 0.085 σ . **b**, S1-M1, M2-pore loop and R/G site from GluA2 are isolated from LBD-TMD_{A1/A2}, contoured at 0.085 σ . **c**, Comparison of the differences by fitting Arg and Gln

into the GluA2 Q/R site density. **d**, Four transmembrane helices (TM1-TM4) in TARP- γ 8 are isolated from LBD-TMD_{mix}, contoured at 0.15 σ . **e**, Four transmembrane helices (TM1-TM4) in CNIH2 are isolated from LBD-TMD_{mix}, contoured at 0.13 σ .



Extended Data Fig. 12 | Electrophysiological recordings of GluA1-TARP- γ 8 mutant proteins. **a**, Current responses of wild-type GluA1-TARP- γ 8 complexes evoked by repeated application of 10 mM glutamate with 10 pulses, each for a duration time of 1 s to reach a plateau of the steady-state current. To measure the inhibition of glutamate-induced currents, 10 μ M JNJ-55511118 was applied before and during glutamate application for 1 s. Bottom insets illustrate the

inhibition effect of JNJ-55511118 on the steady-state current by overlaying the currents without (the last application) and with JNJ-55511118 at timescales of 500 ms (left) and 20 ms (right). **b-h**, Representative recordings for the indicated GluA1 (**b-e**) and TARP- γ 8 (**f-h**) mutant proteins with the same recording conditions as for the wild-type proteins.



Extended Data Fig. 13 | See next page for caption.

Extended Data Fig. 13 | LBD-TMD_{mix} data-processing strategy 2. Particles after two-dimensional and three-dimensional classification clean-up using data-processing strategy 2 were combined into a single stack and refined, and unless otherwise specified, all subsequent processing was performed in cryoSPARC v.2.14. Signal subtraction was implemented using the consensus refinement and a soft mask created around the ATD layer and all possible binding sites of the antibodies. Several rounds of two-dimensional classification were used to remove false positives and particles that still contained the ATD layer. This cleaned stack of particles underwent three-dimensional classification (C1 symmetry), which resulted in a single class displaying continuous transmembrane density features. Particles from this class were subject to two-dimensional classification to remove a small subset

of junk particles. An iterative, sequential, refinement procedure consisting of (1) homogenous refinement, (2) non-uniform refinement, (3) local CTF refinement and (4) non-uniform refinement, was used to improve the resolution of the stack of 151,141 particles. This procedure was iterated twice until no resolution improvement was obtained, resulting in a 3.45 Å map. Particles from this map were then subjected to ab initio classification permitting the removal of junk particles. A new stack of 132,427 particles was then subjected to the previously described four-step refinement procedure for one iteration, before three-dimensional classification was performed in RELION 3.0 to remove junk particles. This final particle stack was subjected to non-uniform refinement in cryoSPARC to obtain the LBD-TMD_{mix} map at 3.25 Å.

Chapter 4

ARCHITECTURE AND CONFORMATIONAL MOBILITY OF CALCIUM-PERMEABLE
CEREBELLAR AMPA RECEPTORS

Abstract

The majority of fast excitatory synaptic transmission in the central nervous system is mediated by α -amino-3-hydroxy-5-methyl-4-isoxazolepropionic acid receptors (AMPARs)²². AMPARs are glutamate-activated ion channels that can be categorized as GluA2-*containing* Ca²⁺-impermeable (CI-) or GluA2-*lacking* Ca²⁺-permeable (CP-) subtypes. Although the majority of AMPARs are calcium-impermeable^{117,205}, CP-AMPARs play pivotal roles at many central synapses, including those that mediate motor control and coordination in the cerebellum^{125,128,151}. CP-AMPARs have functionally distinct properties compared to CI-AMPARs, including faster kinetics¹¹⁵, higher single channel conductance⁶⁹, and inward rectification^{119,120}. Despite these profound differences in functional properties, architectural information of CP-AMPARs is fundamentally lacking. Therefore, to shed light on the subunit composition, physiological architecture, and the gating mechanisms of CP-AMPARs, we immunoaffinity purified CP-AMPARs directly from mouse cerebella. Using single-particle cryo-EM analysis, we identified five putative tetrameric assemblies, with GluA1 accessible at each of the four subunit positions, A-D. Strikingly, in all of the receptor assemblies, we observed displacement of the two ATD dimers in “outward” directions away from the central axis, markedly distinct compared to CI-AMPARs. Furthermore, we observed asymmetrical arrangement of the M3 helices, crucial elements of the gating machinery, emphasizing the relationship between the structural assembly of AMPARs and their complex gating and kinetic properties.

Introduction

At chemical synapses in the central nervous system (CNS), excitatory neurotransmission is largely governed by AMPARs that translate chemical signals to electrical impulses²². The extent of glutamatergic synaptic transmission varies across the CNS, partially dependent on the assembly of AMPARs, which is a critical determinant of receptor localization^{85,149,207}, gating properties^{147,208,209}, and ion permeability^{116,119,121,137,142}. The majority of AMPARs are heteromeric GluA2-containing assemblies¹¹⁷, while those lacking GluA2 constitute a separate population of distinct receptors. RNA editing of GluA2 at codon 607 results in the substitution of a genetically encoded glutamine (Q) with an arginine (R)⁶⁹. This switch from a neutral to a positively charged residue at the apex of the pore-forming selectivity filter causes receptors containing Q/R-edited GluA2 to have a substantially reduced Ca²⁺ permeability compared to those lacking GluA2. As mRNA editing is nearly 100% for the GluA2 subunit, AMPARs are divided into GluA2-containing Ca²⁺-impermeable (CI-) and GluA2-lacking Ca²⁺-permeable (CP-) AMPAR subtypes²¹⁰. Although their global abundance is low under basal conditions, CP-AMPARs are essential to many central synapses, and play pivotal roles in several important forms of synaptic plasticity. Additionally, the upregulation or dysfunction of CP-AMPARs is involved in the pathogenesis of several neurological diseases including Alzheimer's disease^{116,211}, glioblastomas²¹², and chronic pain²¹³.

In the CNS, the region which harbors the greatest abundance of CP-AMPARs is the cerebellum¹¹⁷. In the cerebellum, stellate cells¹⁴⁰, basket cells¹²³, Bergmann glia^{124,125}, and oligodendrocyte precursor cells¹²⁰ are known to express CP-AMPARs, which play essential roles in the learning and execution of coordinated movements. Quantitative proteomics identified GluA4 as the most abundant receptor subunit in the cerebellum¹¹⁷, with multiple studies detecting GluA1/GluA4 heteromers in the cerebellum^{117,119,123}. Furthermore, two transmembrane auxiliary proteins – TARP- γ 7 and TARP- γ 2 (transmembrane AMPA receptor regulatory protein gamma 7 and 2), are predicted to co-assemble with a fraction of cerebellar AMPARs at postsynaptic membranes and influence receptor trafficking, kinetics, and conductance^{121,123,136}.

Despite how well-characterized the abundance, localization, and functional properties of cerebellar CP-AMPARs are, information about their physiological architecture and assembly is fundamentally unknown. In all of the previously reported structures of recombinant and native AMPARs, the GluA2 subunit exclusively occupies the gating-critical B/D positions, which play a prominent role in translating structural rearrangements to channel opening^{150,159,163}. Because cerebellar CP-AMPARs do not harbor the GluA2 subunit, there exists a gap in understanding of which subunits occupy the B/D positions, and how this may alter the canonical gating model.

Therefore, to elucidate the physiological architecture and subunit arrangement of CP-AMPARs, we employed antibody fragments covalently engineered with affinity tags to immunoaffinity purify CP-AMPARs directly from mouse cerebellar tissue. We carried out single-particle cryo-EM studies on these native receptor complexes and discovered the disruption of the ATD dimer-dimer interface, revealing that the ATD dimers adopt a wide range of conformations which “splay outward” from the central axis, strikingly distinct compared to CI-AMPARs^{145,203}. The heterogeneity associated with the mobile ATDs prevented accurate receptor subunit assignment, but nevertheless, we exploited distinct features for the anti-GluA1 11b8 antibody fragment in our 2D class averages to propose the five distinct GluA1-containing receptor assemblies. We found GluA1 able to access all four tetrameric positions, including the gating-critical B/D positions. Additionally, while the resolution of the maps was insufficient to model auxiliary proteins, we observed extracellular protrusions from the detergent micelle at the B'/D' positions, extending towards the lower lobe of the proximal LBD, reminiscent of TARPs. Finally, we noticed distinct changes in the M3 helices and M3-S2 linkers between our CP-AMPARs and previously solved CI-AMPARs^{144,145}, which are crucial elements of the receptor gating machinery linking agonist binding to channel gating. Whereas CI-AMPARs formed a symmetrical gate, we observed a compact, asymmetric gate, underscoring a potential structural basis for faster kinetics and higher single channel conductance, endemic to CP-AMPARs.

Material and Methods

Purification of 3x-FLAG-tagged 11b8 scFv: The 11b8scFv pET-22b E.coli (BL21) expression vector was modified to include a C-terminal 3xFLAG tag sequence (DYKDHDGDYKDHDIDYKDDDDK). Cells were grown at 37 °C in TB containing 100 µg/mL ampicillin. Expression of the 11B8 scFv was induced by addition of 0.1 mM IPTG when the OD₆₀₀ reached 1.5. The temperature of the cultures was reduced to 20 °C and the cells were grown for another 24 h. Cells were collected by centrifugation and lysed by osmotic shock in a lysis buffer containing 200 mM Tris pH 8.0, 20% sucrose and 1 mM EDTA for 30 min on ice. Centrifugation at 200,000g, for 1 h at 4 °C, was carried out to separate periplasmic proteins from cells and cell debris. The supernatant was dialyzed (10 kDa bag) over 48 hrs against 2L (3-4x) of TBS buffer (20 mM Tris, pH 8.0 and 150 mM NaCl) at 4 °C to remove sucrose. The 11b8 scFv was purified by FLAG affinity-chromatography and the eluted protein was subjected to size-exclusion chromatography (SEC). Peak fractions corresponding to monomeric 11b8 scFv were pooled and stored at -80 °C.

Preparation of mouse cerebella: Cerebella were dissected from mice and immediately washed in ice cold PBS buffer. Cerebella were then dounce-homogenized 30-35 times in buffer + PIs until the solution exhibited a uniform consistency. This crude material was then sonicated 0.04*70 with the following parameters: 3sec ON, 5 sec OFF, power = 4.0 for a total of 1.5 min. A low speed spin pelleted the white matter, and the supernatant was saved. Membranes were pelleted following ultracentrifugation and resuspended in TBS.

Immunoaffinity purification of GluA1-containing CP-AMPArs: Mouse cerebellar membranes were solubilized in 2% Digitonin + 2.5µM MPQX, with MPQX included in all subsequent steps. After 3 hrs, ~80 µg of 15F1-Fab-GFP-TwinStrepII were added to the solubilized supernatant and incubated on ice for 30 min. Next, the material was passed through Streptactin XT resin (1 mL) to deplete GluA2-containing AMPARs and the flow-through was retained. The 11b8-3xFLAG-

scFv was added to the flow-through and incubated on ice for 20 min. Post-incubation, FLAG affinity chromatography separated GluA1-containing AMPARs and the 5B2 antibody fragments was added to the eluate. After 15 min incubation on ice, the material was subjected to SEC to separate GluA1-containing CP-AMPARs from unbound antibody. Peak fractions were pooled and concentrated for grid preparation.

Cryo-EM data acquisition: Peak fractions were concentrated to 0.04 mg/mL to a final volume of 70 μ L. Quantifoil R2/1, 300 mesh, + 2nm C (Au) grids were glow discharged (15 mA, 20 sec) just prior to grid vitrification. Grids were blotted with 2.6 μ L of sample, with a blot time of 3 sec, a blot force of 0, in 100% humidity at 14°C. A total of ~44k movies were collected on a Titan Krios with multi-shot collection at Janelia Research Campus equipped with a K3 detector and a BioQuantum energy filter tuned to a 20 keV slit width. Movies were collected in super-resolution mode at a nominal magnification of 105k (0.4155 $\text{\AA}/\text{px}$), with a defocus range from -1.2 – -2.2 μm , and dose-fractionated to 50 frames for a total dose of 50 $\text{e}/\text{\AA}^2$.

Cryo-EM data processing: Movies were motion-corrected by patch motion correction with an output Fourier cropping factor of 1/2 (0.83 $\text{\AA}/\text{pixel}$). Contrast transfer function (CTF) parameters were estimated by patch CTF estimation in cryoSPARC v3.3²¹⁴. A total of 41,228 movies were selected by curated based on ice thickness, CTF fit, and motion curvature. Particles were picked using blob-picker with minimum and maximum particle diameters of 140 \AA and 250 \AA , with a minimum separation distance of 0.8 (diameters). After several rounds of 2D classification, 'junk' particles were removed, resulting in 433,476 particles. Following initial classification, an ab-initio map was generated in cryoSPARC and all subsequent rounds of 3D classification and refinement were carried out in cryoSPARC.

Animal use statement: No experimental manipulations or euthanasia were performed on animals. Pig and cow brain tissue were obtained directly from commercial sources and sheep and rodent brain tissue was dissected from animal carcasses. Euthanasia was not performed by me or any members of Dr. Gouaux's lab.

Results

Immunoaffinity purification of cerebellar GluA1-containing CP-AMPARs

To isolate calcium-permeable AMPA receptor complexes from cerebella, we implemented a tandem, orthogonal purification strategy to selectively isolate GluA1-containing CP-AMPARs (Fig. 4.1). Through systematic screening of orthogonal tags and multi-step chromatographic approaches, we designed a three-step purification strategy relying on a Strep-affinity step to first deplete GluA2-containing AMPARs, followed by a FLAG purification step to capture GluA1-containing AMPARs, and finally, SEC to separate unbound antibodies from receptor complexes. I solubilized 50 mouse cerebellar

with 2% (w/v) digitonin detergent in the presence of 1 mM MPQX, previously shown to preserve the integrity of AMPA receptor complexes^{144,145,203}. We incubated excess 15F1 with this solubilized material, leveraging the C-terminal Twin-StrepII tag engineered to this antibody

fragment to deplete GluA2-containing AMPARs. Next, we added excess of the 11b8 scFv antibody fragment modified with a C-terminal 3xFLAG tag to affinity-purify GluA1-containing AMPARs from the flow-through. Post-SEC, isolated GluA1-containing cerebellar CP-AMPARs showed sufficient purity by SDS-PAGE analysis and were monodisperse by fluorescence size-exclusion chromatography²¹⁵ (FSEC) (Fig. 4.2a,b). Immunoblotting was unable to detect GluA2, indicating that the majority of the purified receptor complexes are calcium-permeable (Fig. 4.2c).

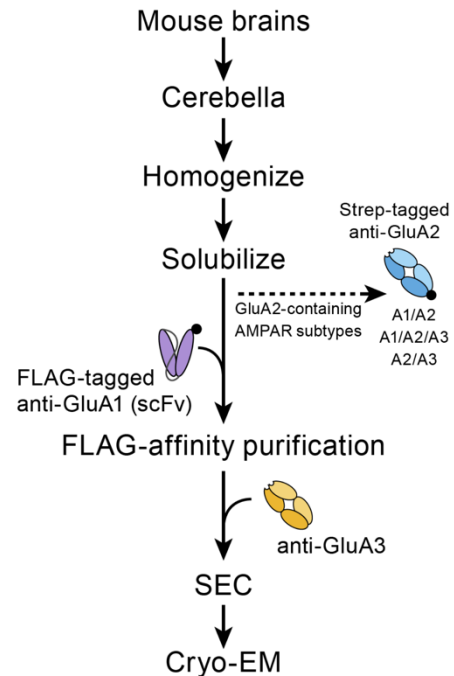


Figure 4.1. Immunoaffinity purification workflow to isolate cerebellar CP-AMPARs. Schematic outlining the purification strategy to isolate GluA1-containing AMPARs from mouse cerebella. Dashed arrow highlights the depletion step for biochemical removal of GluA2-containing AMPAR subtypes.

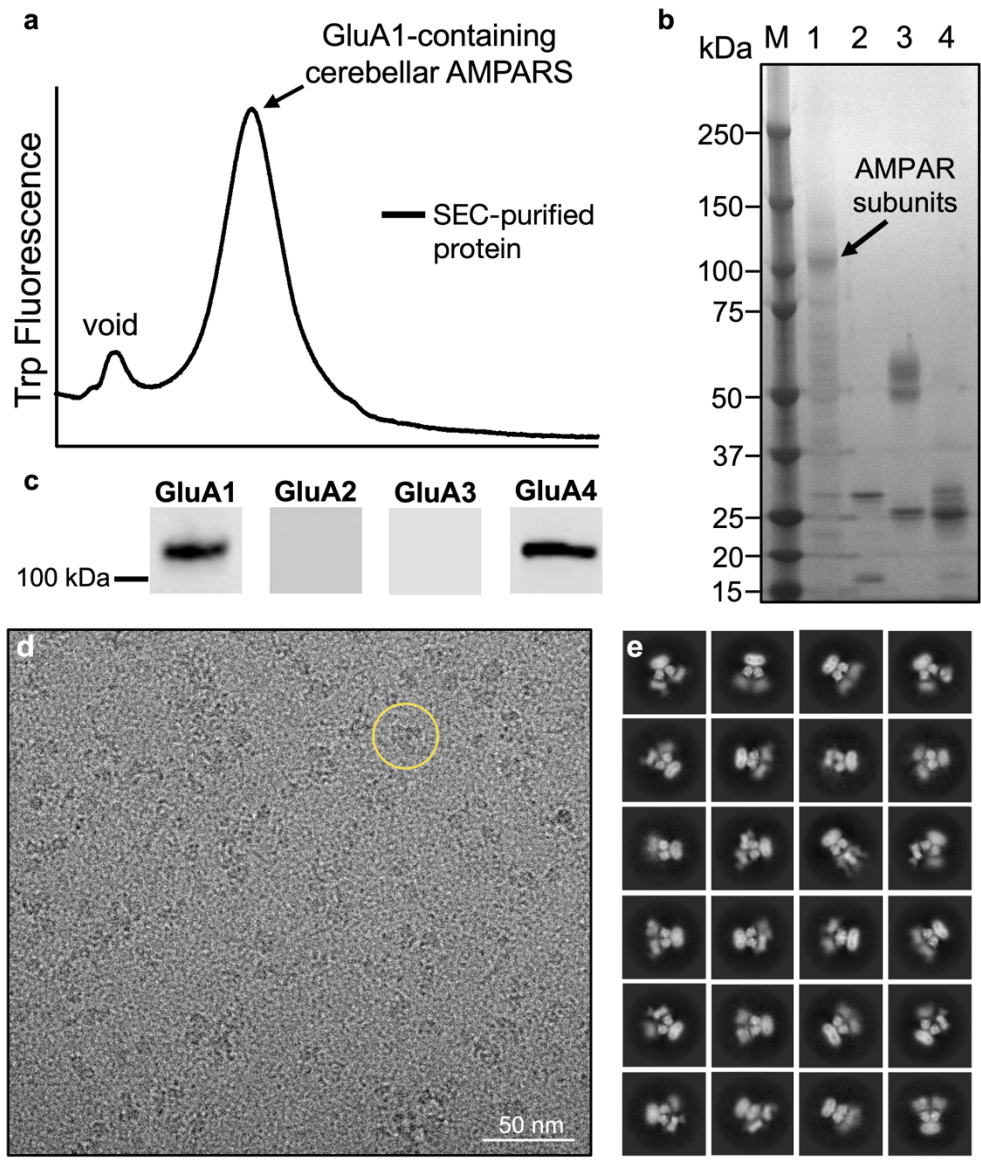


Figure 4.2. Biochemical and cryo-EM analysis of GluA1-containing cerebellar CP-AMPARs. (a) FSEC analysis of the final sample. (b) SDS-PAGE analysis of the final sample. Lanes 1, 2, 3, and 4 are the final sample, 11b8 scFv, 15F1 Fab, and the 5B2 Fab, respectively. (c) Western blotting to detect AMPAR subunits in the final sample. (d) Representative micrograph of particles on 2 nm C grids. Yellow circle outlines a putative particle. (e) A subset of the final 2D class averages.

While, detection of GluA1 and GluA4 was confirmed by Western blotting, interestingly, we were unable to detect GluA3, suggesting a preferential association of GluA3 with GluA2 assemblies in the cerebellum (Fig. 4.2c). The final yield of protein was 2.8 μg , sufficient for grid vitrification with 2 nm carbon support grids and cryo-EM analysis.

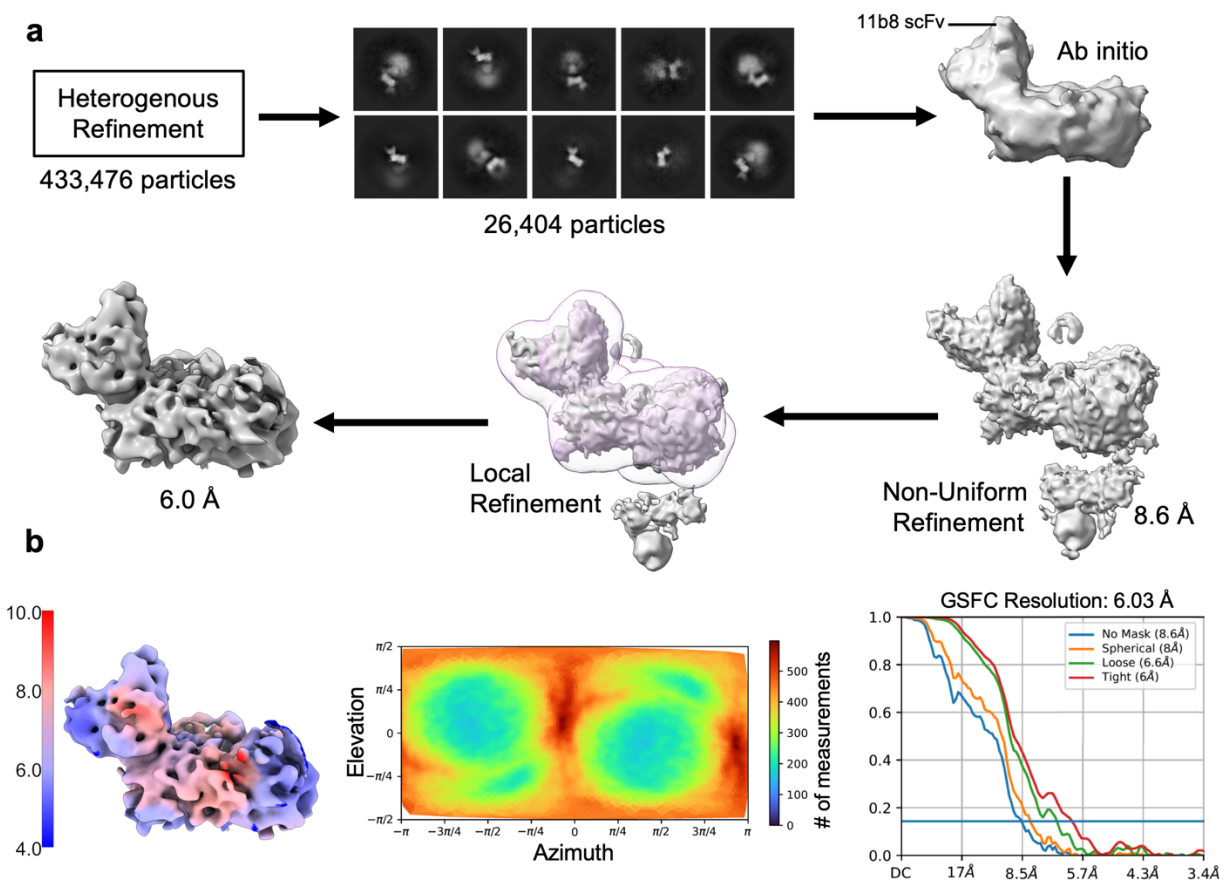


Figure 4.3. Data processing to resolve the structure of a single ATD dimer. (a) Data processing strategy leading to the final map. All steps were carried out in cryoSPARC. (b) Local resolution estimation (units are in Å), angular distribution plot, and gold standard FSC resolution estimation (from left to right).

Conformational mobility of ATD dimers

To define the molecular basis of assembly and gating for CP-AMPARs, we sought to elucidate the structures of cerebellar GluA1-containing CP-AMPARs using single-particle cryo-EM (Fig. 4.2d, Table 4.1). Strikingly, 2D classification revealed a highly conformationally mobile ATD layer, with the majority of the 2D class averages showing blurry ATD features (Fig. 4.2e). In all of the classes, each of the two ATD dimers are “splayed open” away from the global central axis. They adopt a wide range of conformations, precluding structural elucidation and unambiguous identification of receptor subunit occupancy of the A-D positions. However, iterative 3D heterogenous refinement revealed distinguishable secondary structural elements of a single

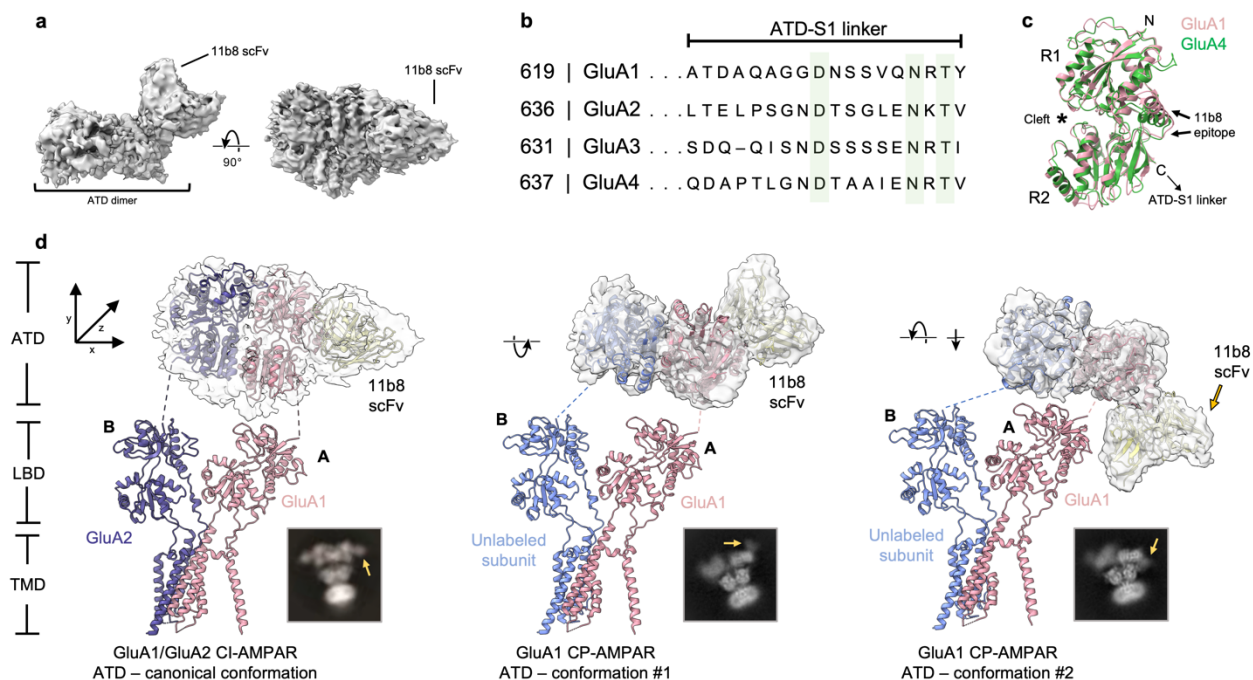


Figure 4.4. Defining two conformations of a GluA1-containing ATD dimer. (a) Cryo-EM structure of single ATD dimer. (b) Sequence comparison of all four receptor subunits for the linkers connecting each ATD protomer to its corresponding LBD. (c) Superposition of a GluA1 ATD protomer (PDB: 7LDD) and a GluA4 ATD protomer (PDB: 4GPA). (d) Modeling possible ATD conformations of a GluA1-containing ATD dimer based on the 2D class averages.

ATD dimer from a small subset of the particles. Using Local Refinement in cryoSPARC, we resolved a 6.0 Å map of an ATD dimer bound to a single 11b8 scFv fragment (Fig. 4.3a,b, Fig. 4.4a). Using an ATD dimer from the previously solved GluA1/GluA2 diheteromeric structure¹⁴⁵, we rigid body fit these coordinates into our map, relying on the quaternary structure of the 11b8 scFv for accurate fitting. Identification of GluA1 was predicated on visualization of the density attributed to 11b8. With insufficient resolution to provide the identification of the protomer coupled to GluA1 in this ATD dimer, we defined it as a subunit unlabeled by an antibody fragment (Fig. 4.4d). Interpreting the orientation of the 11b8 scFv from our 2D class averages enabled us to approximate two putative conformations. In the first orientation, we propose the ATD dimer rotates substantially “backward” into the z-plane (Fig. 4.4d). The second conformation is modeled as a “forward” rotation into the negative z-plane ~180 degrees, with an observed downward translation

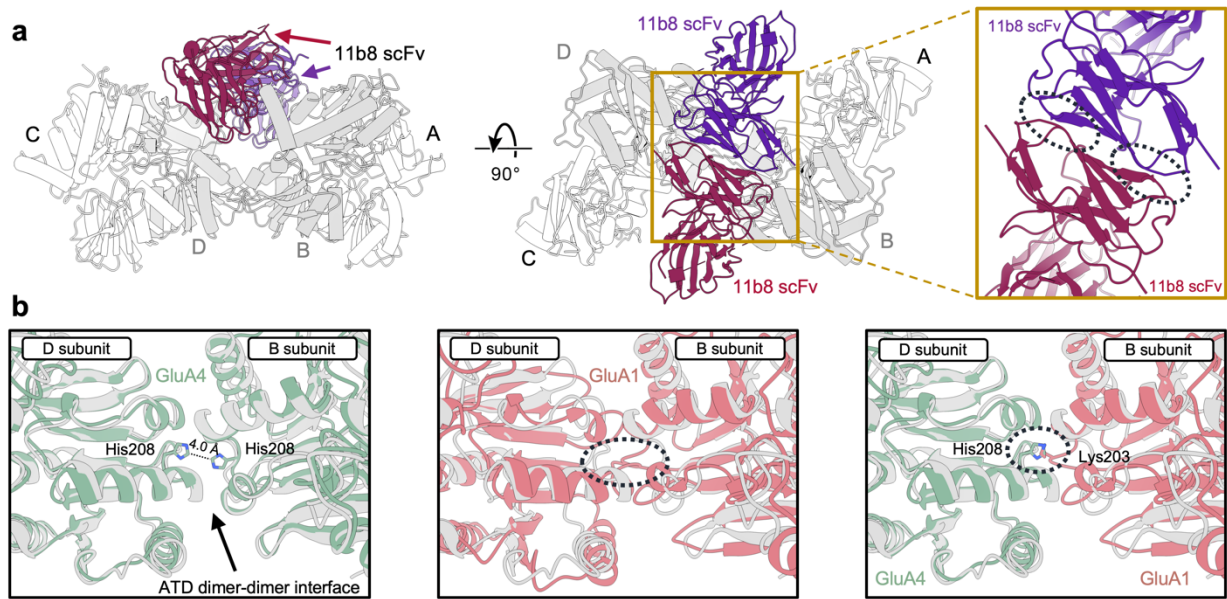


Figure 4.5. Structural modeling of the ATD layer (a) 11b8 scFv labeling of GluA1 at the B and D positions in the ATD. When both positions are occupied by GluA1, indicated clashes between the scFv's are highlighted. (b) The ATD structure of GluA4 (PDB: 4GPA) and GluA1 (PDB: 7LDD) are overlaid at the B/D positions of GluA2 (PDB: 7LDD). Clashes at the dimer-dimer interface are highlighted.

towards the LBDs (Fig. 4.4d). Based solely on the 2D class averages corresponding to this conformation, the ATD dimer appears poised to form interactions with its connected LBD dimer (Fig. 4.4d), but likely is an artefact of 11b8 interacting with the receptor.

Homology modeling of the ATD layer supports the possibility of exogenous stabilization of the ATD layer by presynaptic proteins. First, modeling of GluA1 at the B and D positions reveals two regions where significant steric clashes between the 11b8 scFv's would occur (Fig. 4.5a). These clashes could induce disruption of the ATD dimer-dimer assembly, causing them to separate and “splay open.” However, this case is specific only for occupancy of GluA1 at both the B/D positions, and yet we still observe ATD dimer-dimer disassembly for all particles. It has been previously proposed that stabilization of the ATD layer is contingent upon the formation of a charge-helix dipole interaction at the interface of the B/D positions¹⁴⁴. As seen in native GluA2-containing AMPARs, His208 at opposing B/D positions, close to the global axis of symmetry, is

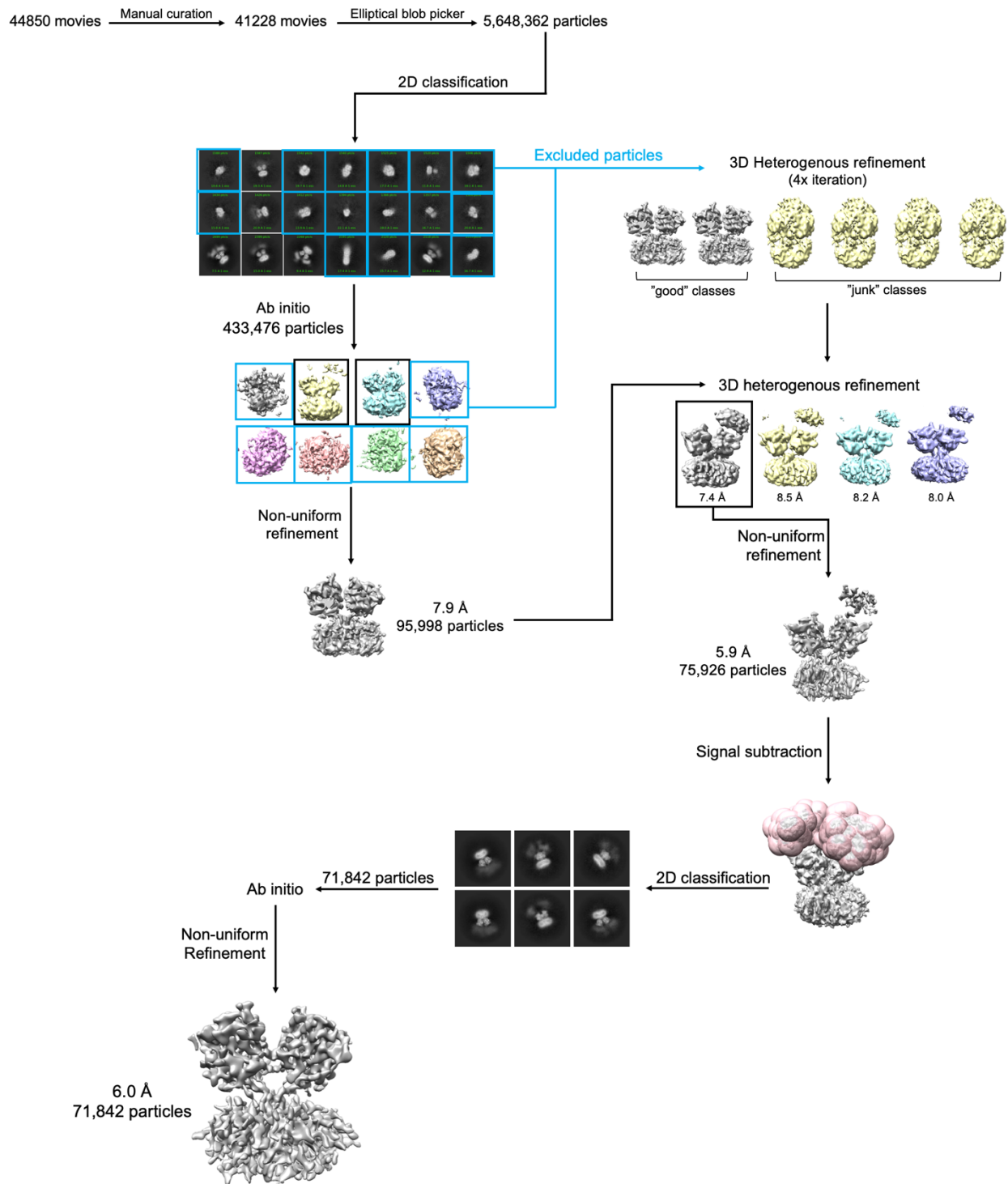


Figure 4.6. Data processing workflow to resolve the LBD-TMD layer. All data processing was carried out in cryoSPARC.

positioned near the negative dipole end of the $\alpha 7$ helix of the opposing subunit (Fig. 4.5b). Sequence comparison reveals that this Histidine residue is conserved in GluA3 and GluA4; however, at the equivalent position at GluA1, this residue is Lys203 which appears to clash with the opposing dimer, even in the case of GluA1/GluA4 heteromers (Fig. 4.5b). Therefore, loss of the conserved ATD dimer-dimer stabilization could induce the observed rotational and translational mobility in native GluA1-containing CP-AMPA receptors.

Structure determination of the LBD-TMD layer

While we observed significant heterogeneity of the ATD dimers, the TMD and LBD layers were more well-resolved in the 2D class averages (Fig. 4.2e). Therefore, we combined all particles together regardless of receptor subtype, knowing that the amino acid sequences of the TMD layer are highly conserved. We used 2D and 3D classification to sort particles, employing signal subtraction to remove the ATD layer and antibody fragments in order to yield a high-resolution map. Our final map resolved to 6.0 Å resolution based on the gold standard FSC criterion, exhibiting hallmark features of the LBD clamshells and the receptor TMD (Fig. 4.6, Fig. 4.7a-e). The local resolution varied across the map, with the lowest resolution for

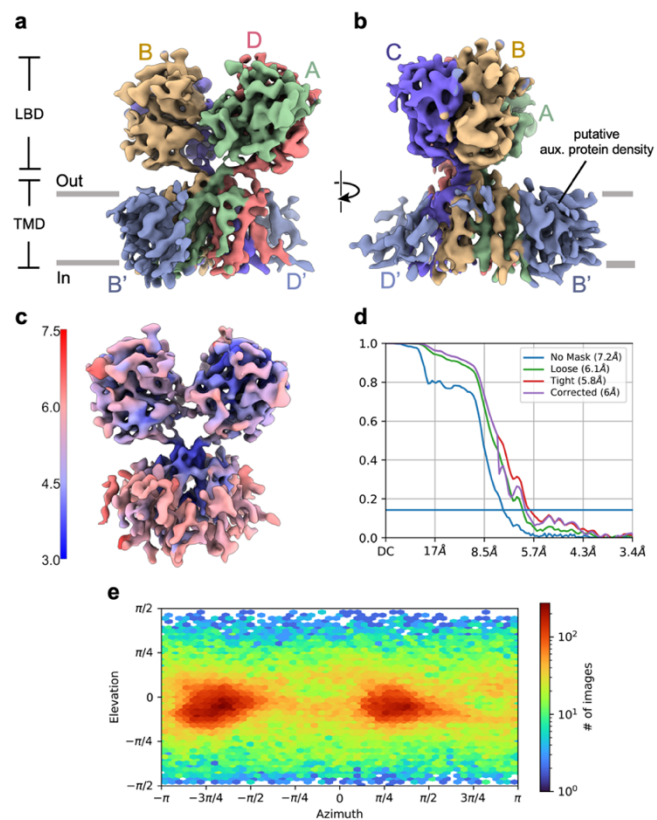


Figure 4.7. The cryo-EM structure of the LBD-TMD layers. (a,b) Representative views of the LBD-TMD map. The four subunit positions, A-D are colored in green, gold, purple, and red, respectively. Density within the micelle (blue) at the B'/D' positions may represent co-assembled auxiliary proteins. (c) Local resolution estimation, (d) gold standard FSC resolution estimation, and (e) angular distribution plot.

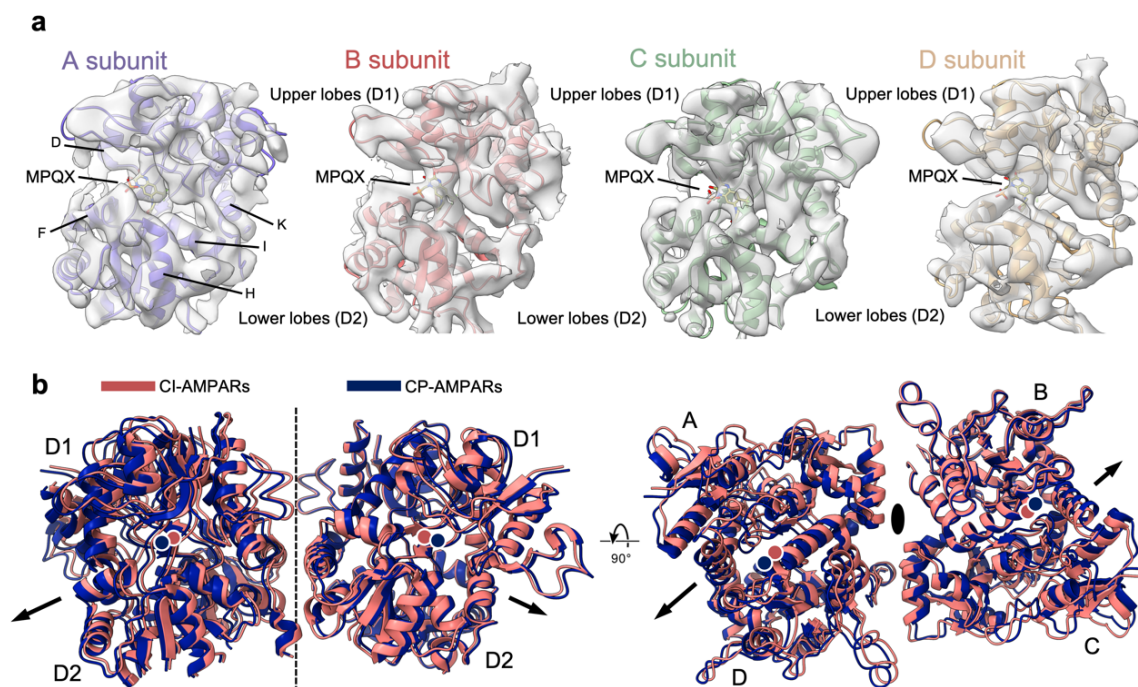


Figure 4.8. Architecture of the LBD layer. (a) Coordinates for the a GluA1 LBD protomer (PDB: 7LDD) were rigid-body fit into the cryo-EM density for each LBD protomer at the A-D positions. (b) Superposition of the hippocampal LBD layer (PDB: 7LDD) (orange) with our LBD structure (dark blue), exhibiting an “outward” expansion away from the two-fold axis (dashed line and black oval) based on the calculated COMs (colored circles).

the receptor TMD region and the strongest for the LBDs (Fig. 4.7c). The resolution of the map was insufficient for *de novo* model building; however, we were able to trace the C α carbon backbone for the LBDs, and elements of the TMD, including the gating-critical M3 helices.

Architecture of the LBD layer

To generate an initial model for the LBD layer, we extracted an individual GluA1 LBD protomer from the MPQX-bound native GluA1/GluA2 hippocampal structure¹⁴⁵ and fit each LBD into the EM density as a rigid-bodies (Fig. 4.8a). We note that the occupancy of receptor subunits in the A-D positions represents a mix of GluA1 and GluA4 preventing accurate subunit assignment; however, the degree of clamshell closure is in line with the LBD layer adopting the closed, resting conformation (Fig. 4.8a). We next sought to compare our LBD structure with the

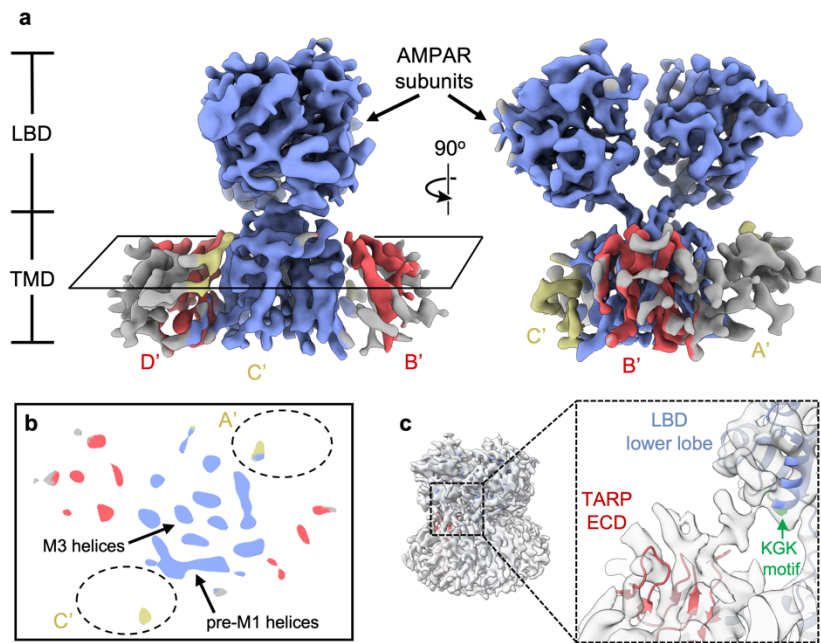


Figure 4.9. TARP-like density features at the B'/D' positions.

(a) Cryo-EM map of the LBD-TMD layer. (b) Cross-section of the EM map, contoured at a high threshold highlighting distinct features for the putative auxiliary protein densities at the B'/D' positions (red). (c) The cryo-EM map was contoured at a low threshold, revealing a protrusion from the detergent micelle, near the lower D2 LBD lobe, and poised to interact with the KGK motif.

coordinates from native hippocampal AMPARs. Superimposing both of the LBD structures shows that in the CP-AMPA structure, each of the LBD dimers are expanded “outward” away from the central axis (Fig. 4.8b), with a greater degree of separation for the A/D dimer compared to the opposing B/C dimer. By calculating the center of mass of each dimer, we highlight an “outward” displacement 2.5 Å for the A/D dimer, whereas in the B/C dimer, we measured this displacement to be only 1.9 Å. We note that resolution limitations may preclude exact measurements of these movements, nevertheless, we surmise this expansion, upon agonist binding, could lead to increased tension of the linkers connected to the channel gate.

Putative TARP-like densities at the B'/D' positions

Unlike the well-resolved LBD layer, we observed discontinuous density for the pre-M1, M1, M2, and M4 helices in the transmembrane domain (Fig. 4.7a,b, Fig. 4.9a). We inspected the map for the appearance of co-assembled auxiliary proteins, finding putative density at the B'/D' positions compared to the homologous A'/C' positions, where we observe almost no density (Fig. 4.9a,b). While the resolution at the B'/D' positions was insufficient for modeling an auxiliary

protein, several features of the EM density permit us to cautiously ascribe these features to auxiliary proteins. At the B'/D' positions, the presence of multiple tube-like densities, oriented orthogonal to the putative plasma membrane, suggest they may represent transmembrane helices. Furthermore, inspection of the map at low thresholds reveals extracellular density protruding out of the detergent micelle, positioned underneath the D2 lower lobes of the LBDs (Fig. 4.9c). We speculate that this density can be, in part, attributed to the conserved acidic spanning residues 85-95 (EDADYEADTAE) present on the extracellular loops of TARPs and poised to interact with the basic KGK motif on the lower lobe of the receptor, a conventionally-accepted interaction critical to how TARPs modulate receptor gating^{158,203,216}.

Interactions between the M3-S2 linkers

Although the overall resolution of the map is insufficient to precisely model side-chain interactions, remarkably, we found the strongest density features in the gating-critical M3 helices, which persisted even when contouring the map to high thresholds (Fig. 4.10a,d). It is likely these densities are well-resolved due to the fully conserved sequence of the M3 helix across all four receptor subunits (Fig. 4.10b). At opposing subunit pairs, A/D and B/C, the M3-S2 linkers are within close proximity of each other and remain visible even at high thresholds (Fig. 4.10c,d). The M3-S2 linkers have no secondary structure, requiring flexibility in order to exert the mechanical pulling force on the M3 helices to gate the channel. Notably, in previous CI-AMPARs maps, the EM density for these linkers rapidly disappears at high thresholds. To provide a molecular basis to explain how the linker interaction may be stabilized, we modeled a putative Arg poised to interact with the backbone carbonyl of the neighboring Glu (Fig. 4.10c). The distance between these two atoms is 2.3 Å, within sufficient distance to form a highly stable hydrogen bond. However, we remain cautious when interpreting this interaction, as the resolution of our map is insufficient for accurate side-chain assignment, and moreover, interactions of M3-S2 linkers with each other may have profound effects on channel gating.

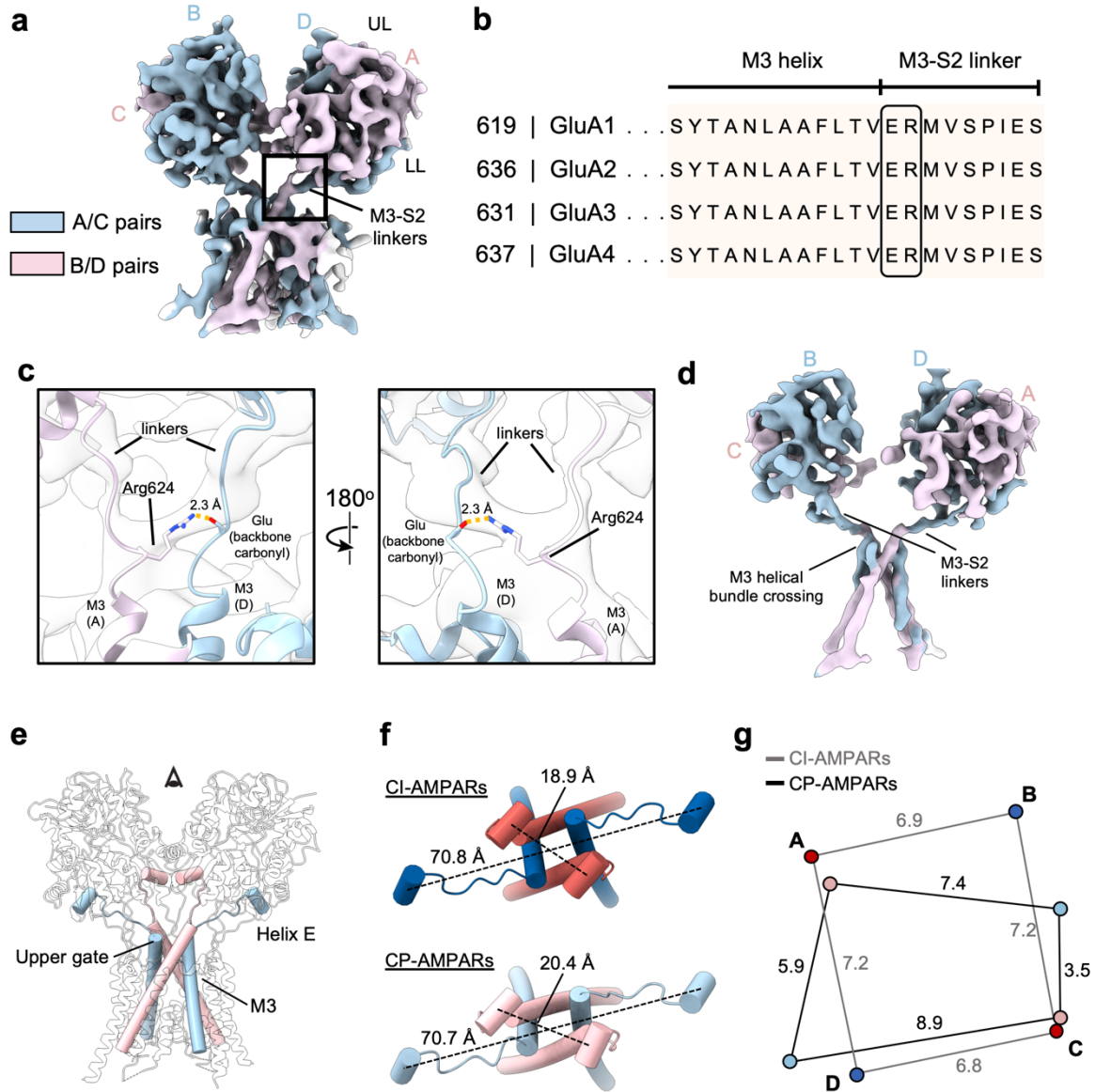


Figure 4.10. Structural and geometric analysis of the gating machinery. (a) Cryo-EM map of the LBD-TMD layer highlighting density for the M3-S2 linkers. (b) Complete sequence conservation of the M3 helix and M3-S2 linkers between all receptor subunits. (c) Magnified views of the putative interaction between neighboring pairs of A/D and B/C M3-S2 linkers with each other. (d) EM density for the LBDs, M3-S2 linkers, and M3 helices are visible in the LBD-TMD map even at a high threshold. (e) Helix E, M3 helices, and the M3-S2 linkers highlighted in the LBD-TMD structure viewed parallel to the membrane. (f) Top down view of the gating machinery, highlighting distances calculated between proximal and opposing helix E COM pairs for both CI-AMPA receptors (PDB: 7LDD) and our CI-AMPA receptor coordinates. Schematic illustrating changes in distances between the Ca-coordinates of Thr625 from each of the four M3 helices. Indicated values colored in grey and black represent CI-AMPA receptors (PDB: 7LDD) and our CP-AMPA receptors, respectively. All distances are in angstroms (Å).

The upper gate adopts a compact, asymmetric conformation

The putative interaction between neighboring M3-S2 linkers emboldened us to examine the structural arrangement of the M3 helical gating machinery. The extracellular ends of the M3 helices, referred to as the M3 helical bundle crossing, constitutes the upper gate, which dictates ion accessibility to the channel pore. The structures of the gating machinery – denoted as the M3 helices, the M3-S2 linkers, and Helix E were derived from the GluA1/GluA2 diheteromeric structure¹⁴⁵ and rigid body fit into the EM density. To describe the D2 lobe separation in these structures, we measured distances between the COMs of helix E, located on the LBD D2 lobe and directly connected to M3 through the M3-S2 linker, for both diagonally opposed positions – B/D and A/C (Fig. 4.10e). We confirmed no obvious changes in the B/D positions, however, the distances between helix E in the A/C positions are increased in our CP-AMPA structure by 1.5 Å (Fig. 4.10f). Geometrical analysis of the upper gate, using the C α carbons for Thr625 to measure distances between the four M3 helices, revealed a more tightly packed conformation of than CI-AMPA (Fig. 4.10g). The arrangement of the gate in our CP-AMPA structure is asymmetric, with an increase in distance between the A/B helices and the C/D helices by 0.5 and 2.1 Å, respectively. Interestingly, we noted a decrease in distances between the A/D and B/C M3 helices, by 1.3 and 3.7 Å, respectively, likely supported by the putative M3-S2 linker interaction between these subunit pairs. Therefore, we propose that the gating machinery for cerebellar CP-AMPA adopts a unique, compact asymmetric gate conformation, alluding to greater tension of the M3-S2 linkers upon agonist binding.

Defining subunit occupancy for cerebellar CP-AMPA

The data processing strategy to resolve our final map did not begin with separation of AMPA assemblies, rather, we combined all particles together throughout all classification and refinement steps. Therefore, to examine which tetrameric receptor subtypes comprise the LBD-TMD map, we re-extracted our particles and used 2D classification to examine the subunit

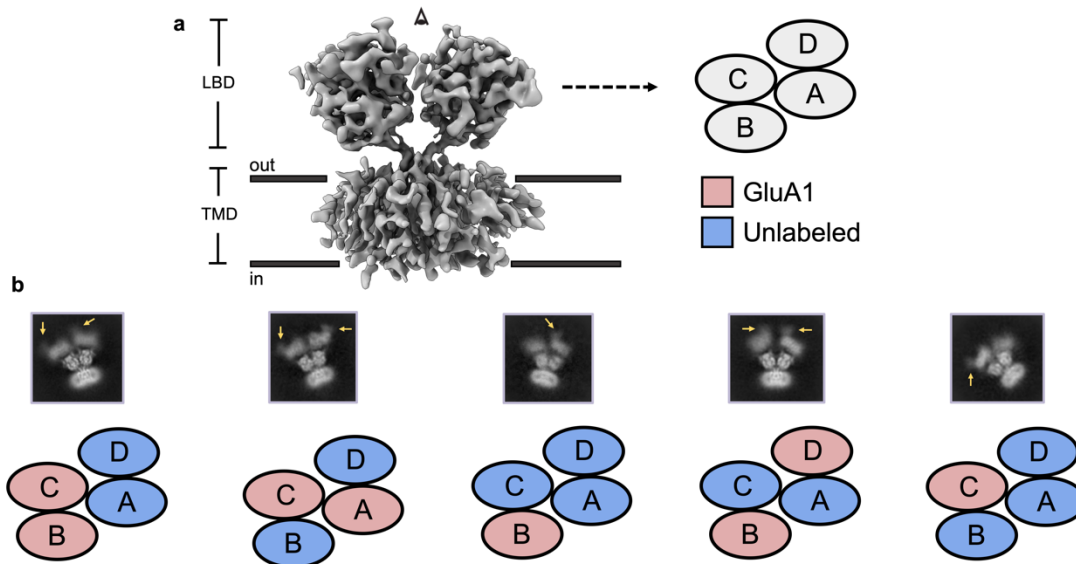


Figure 4.11. Positional occupancy of GluA1 in the LBD-TMD map. (a,b) 2D classification was used to group particles comprising the LBD-TMD map into five distinct assemblies based on density for 11b8 at the A-D positions. Yellow arrows indicate density for the 11b8 scFv.

arrangement of CP-AMPARs. Despite the mobility of the ATD layer, we observed apparent features for 11b8 in several 2D class averages, enabling us to define the arrangement of GluA1. We identified 5 distinct classes, observing GluA1 positions at each of the four positions within the receptor tetramer (Fig. 4.11a,b). Interestingly, at the gating-critical B/D positions, we observed a mix of unlabeled subunits and GluA1, including one assembly with GluA1 simultaneously residing at the B/D positions (Fig. 4.11b). These arrangements imply CP-AMPARs require a less systematic assembly compared to CI-AMPARs, which require GluA2 at both the B/D positions. We realize that modeling of GluA1 simultaneously at two positions within the same receptor based solely on 2D class averages is controversial. Clustering of misaligned particles containing a single GluA1 in the same class average may falsely result in incorrect tetrameric assemblies, and moreover distinguishing occupancy between the equivalent pairs A and C, and B and D, is not possible. Interestingly, no class averages in this map, or through all of data processing, revealed the existence of assemblies with three GluA1 subunits per receptor, nor a GluA1 homomer.

Discussion

Here we present structures of GluA1-containing CP-AMPARs isolated from mouse cerebella using a multistep immunoaffinity purification strategy. Unexpectedly, Western blotting post-purification was unable to detect GluA3 (Fig. 4.2b), and neither any of the 2D class averages or 3D reconstructions displayed density for the anti-GluA3 5B2 Fab. This apparent depletion of GluA3 indicates that the majority, if not all GluA3 subunits, exclusively assemble with CI-AMPARs. Although this does not preclude the existence of cerebellar GluA3 homomers, or GluA1/GluA3 or GluA3/GluA4 heteromeric assemblies, only minor populations of GluA1/GluA3 heteromers have been detected in CA1/2 hippocampal tissue²¹⁷, with no evidence for the assembly of GluA3/GluA4 heteromers in any brain region. Furthermore, recombinant expression studies of GluA3 homomers displays an energetically unfavorable assembly and the formation of intracellular aggregates, suggesting that native GluA3 homomers do not exist²¹⁸. Our results are in agreement with Co-IP¹³⁵ and GluA3 KO studies^{219–221} which have proposed that GluA3 preferentially assembles with GluA2, assembling as heteromers in Golgi cells and Purkinje neurons, and contributing to LTP through cAMP-dependent increase in the receptor P_o ²²².

The most dramatic rearrangements of the ATD layer have been observed in desensitized AMPARs¹⁷³; however, the degree of mobility we observe for our purified receptors is profoundly distinct. This striking difference may be a consequence of unintended disassembly of presynaptic protein complexes during our purification process. The ATDs have been shown to bind presynaptic proteins and play roles in synapse formation and synaptic anchoring^{37,223,224}. For example, the GluA4 ATD has been proposed to bind with neuronal pentraxin-1 (NP1) a lectin protein expressed on axons, which promotes postsynaptic localization of GluA4²²⁵. Perhaps NP1 participates in ATD stabilization, and happened to dissociate during our purification procedure. Furthermore, Lectins have previously been shown to modulate AMPAR function²²⁶, with galectins shown to slow desensitization kinetics²²⁷. Therefore, the possibility remains that the heterogeneity of the ATD layer is not benign, but rather, a functional mechanism distinct to CP-AMPARs.

It has been previously hypothesized that the ATD layer biases AMPAR assembly in favor of specific combinations. Indeed, thermostability and sedimentation experiments of isolated ATDs revealed that the K_d values of dimerization differ substantially between GluA1, GluA2, and GluA3, at ~100 nM, <10 nM, and >1 μ M, respectively^{181,228}. Interestingly, heterodimerization is reduced to nanomolar affinity for both GluA1/GluA2 and GluA2/GluA3 heteromers²²⁸, ostensibly providing a molecular basis supporting the high abundance of GluA1/GluA2 and GluA2/GluA3 heteromers. Our results show a less systematic assembly of CP-AMPARs, with seemingly no rules governing subunit occupancy. Based on our 2D class averages, we found GluA1 is able to access each of the A-D positions, in sharp contrast to hippocampal CI-AMPARs, where GluA1 exclusively resides at just the A/C positions¹⁴⁵. From quantitative mass spectrometry analysis, GluA4 was found to be the most abundance receptor subunit, amounting to an average of ~2.5 GluA4 subunits per tetramer¹¹⁷. Despite the absence of a suitable antibody for GluA4-specific labeling native receptors, the Western blots and reported high abundance of GluA4 supports the assumption that the unlabeled subunits we observed in our 2D classes and 3D reconstructions are GluA4, and thus, the majority of GluA1-containing CP-AMPARs in the cerebellum are GluA1-GluA4 heteromers.

Our purification strategy relied on preparing membranes prior to solubilization, leaving questions unanswered about which cell compartment the receptors were extracted from. Ostensibly, our isolated native receptors are comprised of a mixture of synaptic, extrasynaptic, and ER-localized receptor complexes. Defining which auxiliary proteins co-assemble with our receptor populations may shed light on their localization. The extracellular protrusions from the detergent micelle underscore the existence of co-assembled TARPs in our map. The most abundant auxiliary proteins in the cerebellum are TARP γ -7 and TARP γ -2¹¹⁷, which are likely associated with the putative auxiliary protein density we observe in our cryo-EM map. Previous studies have implicated TARP γ -7 to selectively enhance expression of CP-AMPARs¹²¹, further

supporting our assumption TARPs are present in our map. Interestingly, quantitative mass spectrometry propose that some receptor complexes in the cerebellum harbor only two co-assembled auxiliary proteins, which is also consistent with interpretation of our LBD-TMD map. Nevertheless, the lack of density at the A'/C' positions does not preclude occupancy of auxiliary proteins at these positions, with further examination required to define auxiliary protein co-assembly.

The prevailing model describing how AMPARs open their channels is defined by independent subunit gating^{229,230}. In saturating glutamate conditions (>1 mM), AMPAR conductance levels follow a binomial distribution^{231,232}, whereas in sub-saturating concentrations of glutamate, the relative occupancies deviate considerably from a binomial distribution, exhibiting a greater occupancy at higher conductance levels^{231,232}. This asymmetrical distribution underscores complex gating mechanisms, which only recently has been defined within a structural framework using sub-saturating concentrations of glutamate with GluA2-TARP- γ 2¹⁶⁴. In our best-resolved map, we find an asymmetric conformation of the M3 helical bundle crossing, constituting a striking deviation from the pseudo-symmetric conformation in CI-AMPAR structures^{32,145,203}. This asymmetric conformation is likely germane to heteromeric GluA1/GluA4 heteromers, as our final map is comprised from multiple assemblies. While an asymmetric gate is a hallmark of some ion channels^{233–236}, thus far, it has not been observed in any previous AMPAR structure. The M3 and M3-S2 linkers are fully conserved, leaving the question open as to why we observe an asymmetric conformation of the upper gate. Previous cryo-EM structures largely rely on imposition of C2 symmetry^{144,145}, which although may enhance resolution, may in fact, be selecting a subset of particles amenable for high-resolution structure determination and unintentionally screening out populations of receptors in asymmetric conformations. Perhaps this conformation of the gate enables the M3-S2 linkers to be poised for greater tension exerted upon them following agonist binding and clamshell closure. Conceivably, this gate conformation could also reside at a lower energy barrier, where upon agonist binding, the receptor can more easily

transition to the open state, and ostensibly, reside longer in high conductance levels. We acknowledge this could be a non-functional artefact and that further studies capturing CP-AMPAR structures in agonist-bound states will be important to probe the mechanism of channel gating. In particular, the extent of expansion of the gating ring, which consists of all four D2 lobes, and connected to the M3 helices through the M3-S2 linker, will be a critical component to examine channel gating of CP-AMPARs in future studies.

GluA1-containing cerebellar CP-AMPARs	
<i>Microscope parameters</i>	
Microscope	Titan Krios (Janelia Krios 3)
Camera	K3 + BioQuantum GIF
Magnification	105,000
High tension (keV)	300
Exposure time (s)	3.3 sec
Total dose (e/Å ²)	50
Frames	50
Pixel size (super-res, Å/px)	0.4155
Defocus range (um)	-1.2 – -2.2
Collection strategy	3 x 3 (7 shots per hole)
Slit width (ev)	20
Total movies	44,850
<i>Data processing parameters</i>	
Movies curated	41,228
Amplitude contrast	0.07
Spherical aberration (mm)	2.7
Particles picked	5,648,362
2D classification	cryoSPARC
2D/3D-cleaned particles	484,159
3D classification	cryoSPARC
3D refinement	cryoSPARC

Table 4.1: Cryo-EM data collection and processing statistics

Chapter 5

CONCLUDING REMARKS

Outlook and summary

The history of glutamate receptors has an exceptional and remarkable story. Beginning in the early 1960s, with debate surrounding the veracity of glutamate as a neurotransmitter⁶³ and the existence of excitatory amino acid receptors⁶⁵, to now, more than half a century later, the establishment of glutamate as the principal excitatory neurotransmitter in the CNS and the extensive characterization of ionotropic glutamate receptors; innovative experimental methods have played a significant role in this evolution.

It is not surprising that chemists made notable contributions during the story of glutamate receptors. Indeed, Povl Krogsgaard-Larsen, now a professor of medicinal chemistry, converted ibotenic acid, a neurotoxin found in mushrooms, into the synthetic amino acid, AMPA³¹, and is credited with the nomenclature of AMPA receptors. Many years later, beginning in 1989, molecular biologists etched their names into the glutamate receptor story using PCR-mediated screening to identify ionotropic glutamate receptor subunits^{67,98,101}. At the same time, recombinant and electrophysiology methods progressed the story of glutamate receptors forward, most notably by Peter Seeburg, Nail Burnashev, Bert Sakmann, and Michael Hollmann, who conducted elegant studies which defined the Q/R site⁶⁹, ion permeability¹³⁷, splice variants¹⁰⁵, and AMPAR ion channel kinetics⁹⁸. Building from these studies, Roger Nichol's group leveraged gene targeting to discover the existence of auxiliary proteins¹⁸⁵, finally providing the missing link connecting discrepancies between *in vivo* and *in vitro* electrophysiology recordings. Almost a decade later, Sasha Sobolevsky, Michael Rosconi, and Eric Gouaux employed X-ray crystallography to solve the first full-length structure of an AMPAR³², providing a complete view of the overall architectural organization of the ATD, LBD, and TMD layers. Finally, just a few years ago, Yan Zhao revealed the architecture of a spectrum of native AMPAR assemblies using single-particle cryo-EM¹⁴⁴. Collectively, this study, as well as the preceding research efforts, serve as the inspiration for my dissertation, which is aimed at determining the architecture and assembly of native AMPARs with region-specificity.

The hippocampus plays a central role in declarative or explicit memory⁸⁹, in acquisition of new spatial information²³⁷, as well as in episodic memory⁸⁶, because of its remarkable ability to rewire neuronal circuitry, resulting in synaptic plasticity and synaptic potentiation⁹¹ and depression⁹⁰. Early exploration of hippocampal neuronal circuitry provided evidence for both inhibitory and excitatory synapses²³⁸, and subsequent studies illuminated the central role played by AMPARs in the fast excitatory signaling throughout hippocampal neuronal circuits^{166,178,208}. The molecular structures of hippocampal AMPAR complexes reveal GluA1 and GluA2 are the most prevalent subunits assembled in the hippocampal AMPAR complex, highlighting the important roles of GluA1 and GluA2 in synaptic transmission. The GluA1/GluA2 and the GluA1/A2/A3 subtypes are the major assemblies harboring the GluA2 subunit exclusively at the B/D positions, while the A/C positions are more permissive, suggesting that differential insertion of GluA1 or GluA3 subunits at the A/C positions is a mechanism of synaptic tuning. I discovered the remarkable conservation of auxiliary protein composition and assembly, with TARP- γ 8 and CNIH2 occupying the B'/D' and the A'/C' positions, respectively, forming extensive interactions with the M1 and M4 helices of the receptor. The well-resolved density of the GluA1/A2 LBD-TMD structure defines the position of crucial residues that modulate the permeation and gating of the receptor, including two Arg residues, one at the ion channel Q/R site⁶⁹ and the second at the LBD R/G position¹¹¹. Finally, we propose that the auxiliary protein, SynDIG4, assembles on the periphery of the TMD, interacting extensively with CNIH2, consistent with its primary role in modulating receptor trafficking and kinetics.

The cerebellum coordinates voluntary movements²³⁹, maintains posture²⁴⁰, and regulates motor control⁸⁰. Underlying cerebellar synaptic circuitry are sensory and motor inputs from the cerebral cortex, mediated, in part, by calcium-permeable AMPARs²⁴¹. Evidence suggests cerebellar CP-AMPARs are important for fine-tuning complex motor behavior¹²⁵, involved in multiple synaptic plasticity paradigms, including long-term potentiation and depression⁸², and, furthermore, in circuit remodeling associated with chronic disorders, including fear-related

behaviors¹³³, drug addiction²⁴², and neuropathic pain²⁴³. Structure determination of cerebellar CP-AMPARs revealed stochastic occupancy of the B/D positions by GluA1 and GluA4, suggesting non-deterministic rules governing assembly of these receptors, and intimating that synaptic tuning is not constrained by receptor assembly. Accordingly, compared to the conserved two-fold arrangement of TARP- γ 8 and CNIH2 in the hippocampus, cerebellar CP-AMPARs have non-uniform auxiliary protein stoichiometry, suggesting that non-conserved arrangements underscore cerebellar synaptic signaling. Strikingly, the M3 helices are arranged in an asymmetric conformation, providing the first empirical evidence of an asymmetric gate in an antagonist-bound state. Moreover, the M3-S2 linkers exhibit a robust interaction, which may serve as a mechanism which elicits faster channel kinetics and higher single-channel conductance. Finally, the mobility of the ATD layer and disruption of the ATD dimer-dimer interface may also serve as a structural basis for regulating AMPAR gating, emphasizing the mysterious nature of the ATD layer, and collectively, challenge the requirements for conserved assembly and symmetry in canonical AMPAR functional properties.

Future directions

Despite attempts to improve the resolution of cerebellar CP-AMPARs, I was only able to obtain reconstructions of an ATD dimer and the LBD-TMD layers at ~ 6 Å resolution. The primary challenge remains computationally sorting the heterogeneity into discrete classes for high-resolution refinement. In the LBD-TMD reconstruction, imposition of symmetry resulted in a substantial decline in resolution, due to asymmetry of the LBD promoters and the M3 helices, as well as the heterogenous stoichiometry of auxiliary proteins. While I suspect there may be populations of two-fold symmetric LBD-TMD conformations, these likely represent a small population, and ultimately, I hope that future work will overcome these resolution limitations and result in improved reconstructions. Moreover, future studies capturing native receptors in open or

desensitized states will provide a beautiful glimpse into the gating cycle of native heteromeric AMPAR complexes.

Recent proteomic studies have identified a host of ER-associated proteins which regulate the biogenesis of AMPARs by selectively interacting with receptor assembly intermediates in the ER¹⁸⁰. A large body of evidence suggests receptor subunit monomers dimerize and subsequently tetramerize, driven by interactions of the ATD^{181,244,245} and assisted by proteins such as FRRS1L and CPT1c. Solving structures of immature receptor complexes during this assembly-line like process will shed light on the stoichiometry, binding positions, and assembly mechanisms these chaperones impart on AMPARs, answering long-standing questions of how AMPARs assemble. Therefore, native purification strategies which can selectively isolate these proteins for cryo-EM analysis is undoubtedly a direction worth pursuing. Furthermore, these strategies can also be applied to mouse models of drug addiction, such as cocaine-sensitized rodents²⁴⁶, which can also shed light into disease treatment and behavioral therapies. Finally, cryo-tomography of excitatory synapses, with sufficient resolution to model secondary structure, combined with antibody labeling could provide unprecedented insight into the geometric and spatial architecture of synapses, providing localization and contextual information towards understanding the dynamics of excitatory synaptic transmission.

REFERENCES

1. Diering, G. H. & Huganir, R. L. The AMPA receptor code of synaptic plasticity. *Neuron* **100**, 314–329 (2018).
2. Riedel, G., Platt, B. & Micheau, J. Glutamate receptor function in learning and memory. *Behavioural Brain Research* **140**, 1–47 (2003).
3. Barnes, C. A. Memory deficits associated with senescence: A neurophysiological and behavioral study in the rat. *J Comp Physiol Psychol* **93**, 74–104 (1979).
4. McCleskey, E. W. & Gold, M. S. Ion channels of nociception. *Annu. Rev. Physiol* **61**, 835–56 (1999).
5. Bernier, L. P., Ase, A. R. & Séguéla, P. P2X receptor channels in chronic pain pathways. *Br J Pharmacol* **175**, 2219 (2018).
6. Li, S., Wong, A. H. C. & Liu, F. Ligand-gated ion channel interacting proteins and their role in neuroprotection. *Front Cell Neurosci* **8**, 125 (2014).
7. Anderson, M. J., Cohen, M. W. & Zorychta, E. Effects of innervation on the distribution of acetylcholine receptors on cultured muscle cells. *J Physiol* **268**, 731 (1977).
8. Lindstrom, J., Einarson, B. & Merlie, J. Immunization of rats with polypeptide chains from torpedo acetylcholine receptor causes an autoimmune response to receptors in rat muscle. *PNAS* **75**, 769 (1978).
9. Kalamida, D. *et al.* Muscle and neuronal nicotinic acetylcholine receptors. Structure, function and pathogenicity. *FEBS J* **274**, 3799–3845 (2007).
10. Matsui, M. *et al.* Mice Lacking M2 and M3 muscarinic acetylcholine receptors are devoid of cholinergic smooth muscle contractions but still viable. *Journal of Neuroscience* **22**, 10627–10632 (2002).
11. Fagg, G. E. & Foster, A. C. Amino acid neurotransmitters and their pathways in the mammalian central nervous system. *Neuroscience* **9**, 701–719 (1983).
12. Lovinger, D. M. Communication networks in the brain: Neurons, receptors, neurotransmitters, and alcohol. *Alcohol Research & Health* **31**, 196 (2008).
13. Hyman, S. E. Neurotransmitters. *Current Biology* **15**, R154–R158 (2005).
14. Elliott, T. R. The action of adrenalin. *J Physiol* **32**, 401–467 (1905).
15. Lillie, R. S. The passive iron wire model of proto-plasmic and nervous transmission and its physiological analogues. *Biological Reviews* **11**, 181–209 (1936).
16. Del Castillo, J. & Katz, B. Interaction at end-plate receptors between different choline derivatives. *Proc R Soc Lond B Biol Sci* **146**, 369–381 (1957).

17. Neher, E. & Sakmann, B. Single-channel currents recorded from membrane of denervated frog muscle fibres. *Nature* **260**, 799–802 (1976).
18. Noda, M. *et al.* Primary structure of α -subunit precursor of Torpedo californica acetylcholine receptor deduced from cDNA sequence. *Nature* **299**, 793–797 (1982).
19. Giraudat, J., Devillers-Thiery, A., Auffray, C., Rougeon, F. & Changeux, J. P. Identification of a cDNA clone coding for the acetylcholine binding subunit of Torpedo marmorata acetylcholine receptor. *EMBO J* **1**, 713–717 (1982).
20. Connolly, C. N. & Wafford, K. A. The Cys-loop superfamily of ligand-gated ion channels: the impact of receptor structure on function. *Biochem Soc Trans* **32**, 529–534 (2004).
21. Valera, S. *et al.* A new class of ligand-gated ion channel defined by P2X receptor for extracellular ATP. *Nature* **371**, 516–519 (1994).
22. Hansen, K.B. *et al.* Structure, function, and pharmacology of glutamate receptor ion channels. *Pharmacol Rev.* **4**, 298–487 (2021).
23. Ware, D. K., Kellaris, K. v., Smith, S. & Kyte, J. Assessment of the number of free cysteines and isolation and identification of cystine-containing peptides from acetylcholine receptor. *Biochemistry* **28**, 3469–3481 (1989).
24. Sine, S. M. & Engel, A. G. Recent advances in Cys-loop receptor structure and function. *Nature* **440**, 448–455 (2006).
25. Lynagh, T. & Pless, S. A. Principles of agonist recognition in Cys-loop receptors. *Front Physiol.* **5**, 160 (2014).
26. Ralevic, V. & Dunn, W. R. Purinergic transmission in blood vessels. *Autonomic Neuroscience* **191**, 48–66 (2015).
27. Pankratov, Y., Lalo, U., Krishtal, O. A. & Verkhratsky, A. P2X receptors and synaptic plasticity. *Neuroscience* **158**, 137–148 (2009).
28. North, R. A. Molecular physiology of P2X receptors. *Physiol Rev* **82**, 1013–1067 (2002).
29. Ben-Ari, Y. & Gho, M. Long-lasting modification of the synaptic properties of rat CA3 hippocampal neurones induced by kainic acid. *J Physiol* **404**, 365 (1988).
30. Curtis, D. R. & Watkins, J. C. The excitation and depression of spinal neurones by structurally related amino acids. *J Neurochem* **6**, 117–141 (1960).
31. Krogsgaard-Larsen, P. *et al.* Synthesis and structure-activity studies on excitatory amino acids structurally related to ibotenic acid. *J Med Chem* **28**, 673–679 (1985).
32. Sobolevsky, A. I., Rosconi, M. P. & Gouaux, E. X-ray structure, symmetry and mechanism of an AMPA-subtype glutamate receptor. *Nature* **462**, 745–756 (2009).
33. Jin, R. *et al.* Crystal structure and association behaviour of the GluR2 amino-terminal domain. *EMBO J* **28**, 1812–1823 (2009).

34. Ayalon, G. & Stern-Bach, Y. Functional assembly of AMPA and kainate receptors is mediated by several discrete protein-protein interactions. *Neuron* **31**, 103–113 (2001).
35. Ayalon, G., Segev, E., Elgavish, S. & Stern-Bach, Y. Two regions in the N-terminal domain of ionotropic glutamate receptor 3 form the subunit oligomerization interfaces that control subtype-specific receptor assembly. *Journal of Biological Chemistry* **280**, 15053–15060 (2005).
36. Pasternack, A. *et al.* α -amino-3-hydroxy-5-methyl-4-isoxazolepropionic acid (AMPA) receptor channels lacking the N-terminal domain. *Journal of Biological Chemistry* **277**, 49662–49667 (2002).
37. Watson, J. F., Ho, H. & Greger, I. H. Synaptic transmission and plasticity require AMPA receptor anchoring via its N-terminal domain. *Elife* **6**, (2017).
38. Stern-Bach, Y. *et al.* Agonist selectivity of glutamate receptors is specified by two domains structurally related to bacterial amino acid-binding proteins. *Neuron* **13**, 1345–1357 (1994).
39. Armstrong, N., Sun, Y., Chen, G. Q. & Gouaux, E. Structure of a glutamate-receptor ligand-binding core in complex with kainate. *Nature* **395**, 913–917 (1998).
40. Soderling, T. R. & Derkach, V. A. Postsynaptic protein phosphorylation and LTP. *Trends Neurosci* **23**, 75–80 (2000).
41. Contractor, A. *et al.* Loss of kainate receptor-mediated heterosynaptic facilitation of mossy-fiber synapses in KA2^{-/-} mice. *The Journal of Neuroscience* **23**, 422 (2003).
42. Mathew, S. S., Pozzo-Miller, L. & Hablitz, J. J. Kainate modulates presynaptic GABA release from two vesicle pools. *The Journal of Neuroscience* **28**, 725–31 (2008).
43. Lerma, J. Roles and rules of kainate receptors in synaptic transmission. *Nature Reviews Neuroscience* **4**, 481–495 (2003).
44. Contractor, A., Mulle, C. & Swanson, G. T. Kainate receptors coming of age: milestones of two decades of research. *Trends Neurosci* **34**, 154–163 (2011).
45. Kullmann, D. M. Presynaptic kainate receptors in the hippocampus: slowly emerging from obscurity. *Neuron* **32**, 561–564 (2001).
46. Lauri, S. E., Ryazantseva, M., Orav, E., Vesikansa, A. & Taira, T. Kainate receptors in the developing neuronal networks. *Neuropharmacology* **195**, 108585 (2021).
47. Hanse, E., Taira, T., Lauri, S. & Groc, L. Glutamate synapse in developing brain: an integrative perspective beyond the silent state. *Trends Neurosci* **32**, 532–537 (2009).
48. Banerjee, A., Larsen, R. S., Philpot, B. D. & Paulsen, O. Roles of presynaptic NMDA receptors in neurotransmission and plasticity. *Trends Neurosci* **39**, 26–39 (2016).

49. Pittaluga, A. & Raiteri, M. Release-enhancing glycine-dependent presynaptic NMDA receptors exist on noradrenergic terminals of hippocampus. *Eur J Pharmacol* **191**, 231–234 (1990).
50. Madara, J. C. & Levine, E. S. Presynaptic and postsynaptic NMDA receptors mediate distinct effects of brain-derived neurotrophic factor on synaptic transmission. *J Neurophysiol* **100**, 3175 (2008).
51. Crair, M. C. & Malenka, R. C. A critical period for long-term potentiation at thalamocortical synapses. *Nature* **375**, 325–328 (1995).
52. Hansen, K. B., Yi, F., Perszyk, R. E., Menniti, F. S. & Traynelis, S. F. NMDA receptors in the central nervous system. *Methods Mol Biol* **1677**, 1 (2017).
53. Forsythe, I. D., Westbrook, G. L. & Mayer, M. L. Modulation of excitatory synaptic transmission by glycine and zinc in cultures of mouse hippocampal neurons. *The Journal of Neuroscience* **8**, 3733 (1988).
54. Johnson, J. W. & Ascher, P. Equilibrium and kinetic study of glycine action on the N-methyl-D-aspartate receptor in cultured mouse brain neurons. *J Physiol* **455**, 339 (1992).
55. Mayer, M. L., Westbrook, G. L. & Guthrie, P. B. Voltage-dependent block by Mg²⁺ of NMDA responses in spinal cord neurones. *Nature* **309**, 261–263 (1984).
56. Mayer, M. L. The structure and function of glutamate receptors: Mg²⁺ block to X-ray diffraction. *Neuropharmacology* **112**, 4–10 (2017).
57. Mayer, M. L. Structural biology of glutamate receptor ion channel complexes. *Curr Opin Struct Biol* **41**, 119–127 (2016).
58. Collingridge, G. L., Kehl, S. J. & McLennan, H. Excitatory amino acids in synaptic transmission in the Schaffer collateral-commissural pathway of the rat hippocampus. *J Physiol* **334**, 33 (1983).
59. Tallan, H. H., Moore, S. & Stein, W. H. Studies on the free amino acids and related compounds in the tissues of the cat. *Journal of Biological Chemistry* **211**, 927–939 (1954).
60. Stern, J. R., Eggleston, L. v., Hems, R. & Krebs, H. A. Accumulation of glutamic acid in isolated brain tissue. *Biochemical Journal* **44**, 410 (1949).
61. Krebs, H. A., Eggleston, L. v. & Hems, R. Distribution of glutamine and glutamic acid in animal tissues. *Biochemical Journal* **44**, 159 (1949).
62. Weil-Malherbe, H. Significance of glutamic acid for the metabolism of nervous tissue. *Physiol Rev* **30**, 549–568 (1950).
63. Hayashi, T. A physiological study of epileptic seizures following cortical stimulation in animals and its application to human clinics. *Jpn J Physiol* **3**, 46–64 (1952).

64. Harreveld, A. Van. Compounds in brain extracts causing spreading depression of cerebral cortical activity and contraction of crustacean muscle. *J Neurochem* **3**, 300–315 (1959).
65. Curtis, D. R., Phillis, J. W. & Watkins, J. C. The chemical excitation of spinal neurones by certain acidic amino acids. *J Physiol* **150**, 656 (1960).
66. Curtis, D. R., Phillis, J. W. & Watkins, J. C. Evidence for glutamate as a neurotransmitter in the cat vestibular nerve: radiographic and biochemical studies. *Exp. Brain Res.* **56**, 523–31 (1984).
67. Hollmann, M. & Heinemann, S. Cloned glutamate receptors. *Annu Rev Neurosci* **17**, 31–108 (1994).
68. Armstrong, N. & Gouaux, E. Mechanisms for activation and antagonism of an AMPA-sensitive glutamate receptor: crystal structures of the GluR2 ligand binding core. *Neuron* **28**, 165–181 (2000).
69. Burnashev, N., Villarroel, A. & Sakmann, B. Dimensions and ion selectivity of recombinant AMPA and kainate receptor channels and their dependence on Q/R site residues. *J Physiol* **496**, 165 (1996).
70. Dale, N. & Roberts, A. Dual-component amino-acid-mediated synaptic potentials: excitatory drive for swimming in *Xenopus* embryos. *J Physiol* **363**, 35 (1985).
71. Lüscher, C. *et al.* Role of AMPA Receptor Cycling in Synaptic Transmission and Plasticity. *Neuron* **24**, 649–658 (1999).
72. Schiller, J., Schiller, Y. & Clapham, D. E. NMDA receptors amplify calcium influx into dendritic spines during associative pre- and postsynaptic activation. *Nat. Neurosci.* **1:2** **1**, 114–118 (1998).
73. Paoletti, P. & Neyton, J. NMDA receptor subunits: function and pharmacology. *Curr Opin Pharmacol* **7**, 39–47 (2007).
74. Davies, J. & Watkins, J. C. Selective antagonism of amino acid-induced and synaptic excitation in the cat spinal cord. *J Physiol* **297**, 621–635 (1979).
75. Perszyk, R. E. *et al.* GluN2D-containing N-methyl-D-aspartate receptors mediate synaptic transmission in hippocampal interneurons and regulate interneuron activity. *Mol Pharmacol* **90**, 689–702 (2016).
76. Chang, E. H. *et al.* AMPA receptor downscaling at the onset of Alzheimer's disease pathology in double knockin mice. *PNAS* **103**, 3410–3415 (2006).
77. Baglietto-Vargas, D. *et al.* Impaired AMPA signaling and cytoskeletal alterations induce early synaptic dysfunction in a mouse model of Alzheimer's disease. *Aging Cell* **17**, 12791 (2018).
78. Qu, W. *et al.* Emerging role of AMPA receptor subunit GluA1 in synaptic plasticity: Implications for Alzheimer's disease. *Cell Prolif* **54**, 1 (2021).

79. Kuner, R. *et al.* Late-onset motoneuron disease caused by a functionally modified AMPA receptor subunit. *PNAS* **102**, 5826–5831 (2005).
80. van Damme, P., van den Bosch, L., van Houtte, E., Callewaert, G. & Robberecht, W. GluR2-dependent properties of AMPA receptors determine the selective vulnerability of motor neurons to excitotoxicity. *J Neurophysiol* **88**, 1279–1287 (2002).
81. Soto, D., Altafaj, X., Sindreu, C. & Bayés, À. Glutamate receptor mutations in psychiatric and neurodevelopmental disorders. *Communicative and Integrative Biology* **7**, 1 (2014).
82. Cull-Candy, S. G. & Farrant, M. Ca²⁺-permeable AMPA receptors and their auxiliary subunits in synaptic plasticity and disease. *J Physiol* **599**, 2655-71 (2021).
83. Rakhade, S. N. *et al.* Early alterations of AMPA receptors mediate synaptic potentiation induced by neonatal seizures. *Journal of Neuroscience* **28**, 7979–7990 (2008).
84. Salpietro, V. *et al.* AMPA receptor GluA2 subunit defects are a cause of neurodevelopmental disorders. *Nat. Comm.* 2019 10:1 **10**, 1–16 (2019).
85. Wu, Q.-L., Gao, Y., Li, J.-T., Ma, W.-Y. & Chen, N.-H. The role of AMPARs composition and trafficking in synaptic plasticity and diseases. *Cellular and Molecular Neurobiology* **42**, 2489-2504 (2021).
86. Burgess, N., Maguire, E. A. & O'Keefe, J. The Human Hippocampus and Spatial and Episodic Memory. *Neuron* **35**, 625–641 (2002).
87. Diering, G. H. & Huganir, R. L. The AMPA receptor code of synaptic plasticity. *Neuron* **100**, 314–329 (2018).
88. Riedel, G., Platt, B. & Micheau, J. Glutamate receptor function in learning and memory. *Behavioural Brain Research* **140**, 1–47 (2003).
89. SCOVILLE, W. B. & MILNER, B. Loss of recent memory after bilateral hippocampal lesions. *J Neurol Neurosurg Psychiatry* **20**, 11–21 (1957).
90. Dunwiddie, T. & Lynch, G. Long-term potentiation and depression of synaptic responses in the rat hippocampus: localization and frequency dependency. *J Physiol* **276**, 353 (1978).
91. Whitlock, J. R., Heynen, A. J., Shuler, M. G. & Bear, M. F. Learning induces long-term potentiation in the hippocampus. *Science* **313**, 1093–1097 (2006).
92. Bliss, T. V. P. & Lømo, T. Long-lasting potentiation of synaptic transmission in the dentate area of the anaesthetized rabbit following stimulation of the perforant path. *J Physiol* **232**, 331 (1973).
93. Bliss, T. V. P. & Collingridge, G. L. A synaptic model of memory: long-term potentiation in the hippocampus. *Nature* **361**, 31–39 (1993).

94. Malleret, G. *et al.* Bidirectional regulation of hippocampal long-term synaptic plasticity and its influence on opposing forms of memory. *The Journal of Neuroscience* **30**, 3813 (2010).
95. Randic, M., Jiang, M. C. & Cerne, R. Long-term potentiation and long-term depression of primary afferent neurotransmission in the rat spinal cord. *The Journal of Neuroscience* **13**, 52286241 (1993).
96. Chung, H. J., Steinberg, J. P., Huganir, R. L. & Linden, D. J. Requirement of AMPA receptor GluR2 phosphorylation for cerebellar long-term depression. *Science* **300**, 1751–1755 (2003).
97. Gundersen, C. B., Miledi, R. & Parker, I. Messenger RNA from human brain induces drug- and voltage-operated channels in *Xenopus* oocytes. *Nature* **308**, 421–424 (1984).
98. Hollmann, M., O’Shea-Greenfield, A., Rogers, S. W. & Heinemann, S. Cloning by functional expression of a member of the glutamate receptor family. *Nature* **342**, 643–648 (1989).
99. Sakimura, K. *et al.* Functional expression from cloned cDNAs of glutamate receptor species responsive to kainate and quisqualate. *FEBS Lett* **272**, 73–80 (1990).
100. Sun, W. *et al.* Molecular cloning, chromosomal mapping, and functional expression of human brain glutamate receptors. *PNAS* **89**, 1443 (1992).
101. Keinänen, K. *et al.* A family of AMPA-selective glutamate receptors. *Science* **249**, 556–560 (1990).
102. Nakanishi, N., Shneider, N. A. & Axel, R. A family of glutamate receptor genes: Evidence for the formation of heteromultimeric receptors with distinct channel properties. *Neuron* **5**, 569 (1990).
103. Greger, I. H., Watson, J. F. & Cull-Candy, S. G. Structural and functional architecture of AMPA-type glutamate receptors and their auxiliary proteins. *Neuron* **94**, 713–730 (2017).
104. Jin, R., Horning, M., Mayer, M. L. & Gouaux, E. Mechanism of activation and selectivity in a ligand-gated ion channel: Structural and functional studies of GluR2 and quisqualate. *Biochemistry* **41**, 15635–15643 (2002).
105. Sommer, B. *et al.* Flip and Flop: A cell-specific functional switch in glutamate-operated channels of the CNS. *Science* **249**, 1580–1585 (1990).
106. Mosbacher, J. *et al.* A molecular determinant for submillisecond desensitization in glutamate receptors. *Science* **266**, 1059–1062 (1994).
107. Krampfl, K., Schlesinger, F., Wolfes, H., Dengler, R. & Bufler, J. Functional diversity of recombinant human AMPA type glutamate receptors: possible implications for selective vulnerability of motor neurons. *J Neurol Sci* **191**, 19–23 (2001).
108. Partin, K. M., Bowie, D. & Mayer, M. L. Structural determinants of allosteric regulation in alternatively spliced AMPA receptors. *Neuron* **14**, 833–843 (1995).

109. Grosskreutz, J. *et al.* Kinetic properties of human AMPA-type glutamate receptors expressed in HEK293 cells. *European Journal of Neuroscience* **17**, 1173–1178 (2003).
110. Koike, M., Tsukada, S., Tsuzuki, K., Kijima, H. & Ozawa, S. Regulation of kinetic properties of GluR2 AMPA receptor channels by alternative splicing. *The Journal of Neuroscience* **20**, 2166 (2000).
111. Lomeli, H. *et al.* Control of kinetic properties of AMPA receptor channels by nuclear RNA editing. *Science* **266**, 1709–1713 (1994).
112. Song, I. & Huganir, R. L. Regulation of AMPA receptors during synaptic plasticity. *Trends Neurosci* **25**, 578–588 (2002).
113. Zhou, Z. *et al.* The C-terminal tails of endogenous GluA1 and GluA2 differentially contribute to hippocampal synaptic plasticity and learning. *Nat. Neurosci.* **21**, 50–62 (2017).
114. Derkach, V., Barria, A. & Soderling, T. R. Ca²⁺/calmodulin-kinase II enhances channel conductance of α -amino-3-hydroxy-5-methyl-4-isoxazolepropionate type glutamate receptors. *PNAS* **96**, 3269–3274 (1999).
115. Verdoorn, T. A., Burnashev, N., Monyer, H., Seeburg, P. H. & Sakmann, B. Structural determinants of ion flow through recombinant glutamate receptor channels. *Science* **252**, 1715–1718 (1991).
116. Cull-Candy, S., Kelly, L. & Farrant, M. Regulation of Ca²⁺-permeable AMPA receptors: synaptic plasticity and beyond. *Curr Opin Neurobiol* **16**, 288–297 (2006).
117. Schwenk, J. *et al.* Regional diversity and developmental dynamics of the AMPA-receptor proteome in the mammalian brain. *Neuron* **84**, 41–54 (2014).
118. Lu, W. *et al.* Subunit composition of synaptic AMPA receptors revealed by a single-cell genetic approach. *Neuron* **62**, 254 (2009).
119. Liu, S. Q. J. & Cull-Candy, S. G. Synaptic activity at calcium-permeable AMPA receptors induces a switch in receptor subtype. *Nature* **405**, 454–458 (2000).
120. Coombs, I. *et al.* Enhanced functional detection of synaptic calcium-permeable AMPA receptors using intracellular NASPM. *Elife* **12**, (2023).
121. Studniarczyk, D., Coombs, I., Cull-Candy, S. G. & Farrant, M. TARP γ -7 selectively enhances synaptic expression of calcium-permeable AMPARs. *Nat Neurosci* **16**, 1266–1274 (2013).
122. Soto, D. *et al.* Selective regulation of long-form calcium-permeable AMPA receptors by an atypical TARP, γ -5. *Nat Neurosci* **12**, 277–285 (2009).
123. Bats, C., Farrant, M. & Cull-Candy, S. G. A role of TARPs in the expression and plasticity of calcium-permeable AMPARs: Evidence from cerebellar neurons and glia. *Neuropharmacology* **74**, 76–85 (2013).

124. Iino, M. *et al.* Glia-synapse interaction through Ca²⁺-permeable AMPA receptors in Bergmann glia. *Science* **292**, 926–929 (2001).
125. Saab, A. S. *et al.* Bergmann glial AMPA receptors are required for fine motor coordination. *Science* **337**, 749–753 (2012).
126. Zhang, Q., Zhang, G., Meng, F. & Tian, H. Biphasic activation of apoptosis signal-regulating kinase 1-stress-activated protein kinase 1-c-Jun N-terminal protein kinase pathway is selectively mediated by Ca²⁺-permeable alpha-amino-3-hydroxy-5-methyl-4-isoxazolepropionate receptors involving oxidative stress following brain ischemia in rat hippocampus. *Neurosci. Lett* **337**, 51–55 (2003).
127. Selvaraj, B. T. *et al.* C9ORF72 repeat expansion causes vulnerability of motor neurons to Ca²⁺-permeable AMPA receptor-mediated excitotoxicity. *Nat. Commun* **9**, (2018).
128. Yamazaki, M. *et al.* Relative contribution of TARPs γ -2 and γ -7 to cerebellar excitatory synaptic transmission and motor behavior. *PNAS* **112**, 371–379 (2015).
129. Park, P. *et al.* The Role of Calcium-Permeable AMPARs in Long-Term Potentiation at Principal Neurons in the Rodent Hippocampus. *Front Synaptic Neurosci* **10**, 42 (2018).
130. Brill, J. & Huguenard, J. R. Sequential Changes in AMPA Receptor Targeting in the Developing Neocortical Excitatory Circuit. *The Journal of Neuroscience* **28**, 13918 (2008).
131. Plant, K. *et al.* Transient incorporation of native GluR2-lacking AMPA receptors during hippocampal long-term potentiation. *Nat. Neurosci* **9**, 602–604 (2006).
132. Yang, Y., Wang, X. bin & Zhou, Q. Perisynaptic GluR2-lacking AMPA receptors control the reversibility of synaptic and spines modifications. *PNAS* **107**, 11999–12004 (2010).
133. Clem, R. L. & Huganir, R. L. Calcium-Permeable AMPA receptor dynamics mediate fear memory erasure. *Science* **330**, 1108 (2010).
134. Huupponen, J., Atanasova, T., Taira, T. & Lauri, S. E. GluA4 subunit of AMPA receptors mediates the early synaptic response to altered network activity in the developing hippocampus. *J Neurophysiol* **115**, 2989 (2016).
135. Wenthold, R. J., Petralia, R. S. & Niedzielski, A. S. Evidence for multiple AMPA receptor complexes in hippocampal CA1/CA2 neurons. *The Journal of Neuroscience* **16**, 1982-89 (1996).
136. Soto, D., Coombs, I. D., Kelly, L., Farrant, M. & Cull-Candy, S. G. Stargazin attenuates intracellular polyamine block of calcium-permeable AMPA receptors. *Nat Neurosci* **10**, 1260–7 (2007).
137. Burnashev, N., Monyer, H., Seeburg, P. H. & Sakmann, B. Divalent ion permeability of AMPA receptor channels is dominated by the edited form of a single subunit. *Neuron* **8**, 189–198 (1992).
138. Bowie, D. Polyamine-mediated channel block of ionotropic glutamate receptors and its regulation by auxiliary proteins. *J Biol Chem* **293**, 18789–18802 (2018).

139. Pellegrini-Giampietro, D. E. An activity-dependent spermine-mediated mechanism that modulates glutamate transmission. *Trends in Neurosciences* **26**, 9–11 (2003).
140. Kelly, L., Farrant, M. & Cull-Candy, S. G. Synaptic mGluR activation drives plasticity of calcium-permeable AMPA receptors. *Nat. Neurosci* **12**, 593–601 (2009).
141. Biedermann, J., Braunbeck, S., Plested, A. J. R. & Sun, H. Nonselective cation permeation in an AMPA-type glutamate receptor. *PNAS* **118**, e2012843118 (2021).
142. Jatzke, C., Watanabe, J. & Wollmuth, L. P. Voltage and concentration dependence of Ca²⁺ permeability in recombinant glutamate receptor subtypes. *J Physiol* **538**, 25 (2002).
143. Kumar, S. & Kumar, S. S. A Model for Predicting cation selectivity and permeability in AMPA and NMDA receptors based on receptor subunit composition. *Front Synaptic Neurosci* **13**, 63 (2021).
144. Zhao, Y., Chen, S., Swensen, A. C., Qian, W. J. & Gouaux, E. Architecture and subunit arrangement of native AMPA receptors elucidated by cryo-EM. *Science* **364**, 355–362 (2019).
145. Yu, J. *et al.* Hippocampal AMPA receptor assemblies and mechanism of allosteric inhibition. *Nature* **594**, 448–453 (2021).
146. Jiang, J., Suppiramaniam, V. & Wooten, M. W. Posttranslational modifications and receptor-associated proteins in AMPA receptor trafficking and synaptic plasticity. *Neurosignals* **15**, 266–282 (2006).
147. Milstein, A. D. & Nicoll, R. A. Regulation of AMPA receptor gating and pharmacology by TARP auxiliary subunits. *Trends Pharmacol Sci* **29**, 333–9 (2008).
148. Kato, A. S., Siuda, E. R., Nisenbaum, E. S. & Bredt, D. S. AMPA receptor subunit-specific regulation by a distinct family of Type II TARPs. *Neuron* **59**, 986–996 (2008).
149. Shi, Y. *et al.* Functional comparison of the effects of TARPs and cornichons on AMPA receptor trafficking and gating. *PNAS* **107**, 16315–9 (2010).
150. Chen, S. *et al.* Activation and desensitization mechanism of AMPA receptor-TARP complex by cryo-EM. *Cell* **170**, 1234–1246 (2017).
151. Yamazaki, M. *et al.* Relative contribution of TARPs γ -2 and γ -7 to cerebellar excitatory synaptic transmission and motor behavior. *PNAS* **112**, 371–9 (2015).
152. Cho, C.-H., St-Gelais, F., Zhang, W., Tomita, S. & Howe, J. R. Two families of TARP isoforms that have distinct effects on the kinetic properties of AMPA receptors and synaptic currents. *Neuron* **55**, 890–904 (2007).
153. Twomey, E. C. & Sobolevsky, A. I. Structural mechanisms of gating in ionotropic glutamate receptors. *Biochemistry* **57**, 267–276 (2018).

154. Armstrong, N., Jasti, J., Beich-Frandsen, M. & Gouaux, E. Measurement of conformational changes accompanying desensitization in an ionotropic glutamate receptor. *Cell* **127**, 85–97 (2006).
155. Sun, Y. *et al.* Mechanism of glutamate receptor desensitization. *Nature* **417**, 245–253 (2002).
156. Chen, L., Dürr, K. L. & Gouaux, E. Activation mechanism of AMPA receptors illuminated by complexes with cone snail toxin, allosteric potentiator and orthosteric agonists. *Science* **345**, 1021 (2014).
157. Dürr, K. L. *et al.* Structure and dynamics of AMPA receptor GluA2 in resting, pre-open, and desensitized States. *Cell* **158**, 778–792 (2014).
158. Twomey, E. C., Yelshanskaya, M. v, Grassucci, R. A., Frank, J. & Sobolevsky, A. I. Elucidation of AMPA receptor-stargazin complexes by cryo-electron microscopy. *Science* **353**, 83–6 (2016).
159. Twomey, E. C., Yelshanskaya, M. v., Grassucci, R. A., Frank, J. & Sobolevsky, A. I. Channel opening and gating mechanism in AMPA-subtype glutamate receptors. *Nature* **549**, 60–65 (2017).
160. Twomey, E. C., Yelshanskaya, M. v., Grassucci, R. A., Frank, J. & Sobolevsky, A. I. Structural basis of desensitization in AMPA receptor-auxiliary subunit complexes. *Neuron* **94**, 569-580 (2017).
161. Sobolevsky, A. I. Structure and gating of tetrameric glutamate receptors. *J Physiol* **593**, 29–38 (2015).
162. Bergles, D. E., Diamond, J. S. & Jahr, C. E. Clearance of glutamate inside the synapse and beyond. *Curr Opin Neurobiol* **9**, 293–298 (1999).
163. Zhang, D., Watson, J. F., Matthews, P. M., Cais, O. & Greger, I. H. Gating and modulation of a hetero-octameric AMPA glutamate receptor. *Nature* **594**, 454-458 (2021).
164. Yelshanskaya, M. v., Patel, D. S., Kottke, C. M., Kurnikova, M. G. & Sobolevsky, A. I. Opening of glutamate receptor channel to subconductance levels. *Nature* **605**, 172-178 (2022).
165. Smith, T. C., Wang, L. Y. & Howe, J. R. Heterogeneous conductance levels of native AMPA receptors. *Journal of Neuroscience* **20**, 2073–2085 (2000).
166. Jahr, C., *et al.* Glutamate activates multiple single channel conductances in hippocampal neurons. *Nature* **325**, 522–525 (1987).
167. Cull-Candy, S. G. & Usowicz, M. M. Multiple-conductance channels activated by excitatory amino acids in cerebellar neurons. *Nature* **325**, 525–528 (1987).
168. Partin, K. M., Fleck, M. W. & Mayer, M. L. AMPA receptor flip/flop mutants affecting deactivation, desensitization, and modulation by cyclothiazide, aniracetam, and thiocyanate. *Journal of Neuroscience* **16**, 6634–6647 (1996).

169. Robert, A. & Howe, J. R. How AMPA receptor desensitization depends on receptor occupancy. *J Neurosci* **23**, 847–58 (2003).
170. Salazar, H., Mischke, S. & Plested, A. J. R. Measurements of the timescale and conformational space of AMPA receptor desensitization. *Biophys J* **119**, 206–218 (2020).
171. Klykov, O., Gangwar, S. P., Yelshanskaya, M. v., Yen, L. & Sobolevsky, A. I. Structure and desensitization of AMPA receptor complexes with type II TARP $\gamma 5$ and GSG1L. *Mol Cell* **81**, 4771–4783 (2021).
172. Stern-Bach, Y., Russo, S., Neuman, M. & Rosenmund, C. A point mutation in the glutamate binding site blocks desensitization of AMPA receptors. *Neuron* **21**, 907–918 (1998).
173. Meyerson, J. R. *et al.* Structural mechanism of glutamate receptor activation and desensitization. *Nature* **514**, 328–334 (2014).
174. Lawrence, J. & Trussell, L. O. Long-term specification of AMPA receptor properties after synapse formation. *Journal of Neuroscience* **20**, 4864–4870 (2000).
175. Orlandi, C. *et al.* AMPA receptor regulation at the mRNA and protein level in rat primary cortical cultures. *PLOS One* **6**, e25350 (2011).
176. Nusser, Z. *et al.* Cell type and pathway dependence of synaptic AMPA receptor number and variability in the hippocampus. *Neuron* **21**, 545–559 (1998).
177. Shi, Y., Lu, W., Milstein, A. D. & Nicoll, R. A. The stoichiometry of AMPA receptors and TARPs varies by neuronal cell type. *Neuron* **62**, 633–640 (2009).
178. Penn, A. C. *et al.* Hippocampal LTP and contextual learning require surface diffusion of AMPA receptors. *Nature* **549**, 384–388 (2017).
179. Schwenk, J. & Fakler, B. Building of AMPA-type glutamate receptors in the endoplasmic reticulum and its implication for excitatory neurotransmission. *J Physiol* **599**, 2639–2653 (2020).
180. Schwenk, J. *et al.* An ER assembly line of AMPA-Receptors controls excitatory neurotransmission and its plasticity. *Neuron* **104**, 680–692 (2019).
181. Zhao, H. *et al.* Preferential assembly of heteromeric kainate and AMPA receptor amino terminal domains. *Elife* **6**, e32056 (2017).
182. Schwenk, J. *et al.* Functional proteomics identify cornichon proteins as auxiliary subunits of AMPA receptors. *Science* **323**, 1313–9 (2009).
183. Bats, C., Soto, D., Studniarczyk, D., Farrant, M. & Cull-Candy, S. G. Channel properties reveal differential expression of TARPed and TARPless AMPARs in stargazer neurons. *Nat Neurosci* **15**, 853–861 (2012).

184. Schwenk, J. *et al.* High-resolution proteomics unravel architecture and molecular diversity of native AMPA receptor complexes. *Neuron* **74**, 621–633 (2012).
185. Chen, L. *et al.* Stargazin regulates synaptic targeting of AMPA receptors by two distinct mechanisms. *Nature* **408**, 936–943 (2000).
186. Nakamura, S. *et al.* Morphologic determinant of tight junctions revealed by claudin-3 structures. *Nat Comm.* **10**, 816 (2019).
187. Simms, B. A. & Zamponi, G. W. Neuronal voltage-gated calcium channels: structure, function, and dysfunction. *Neuron* **82**, 24–45 (2014).
188. Kamalova, A. & Nakagawa, T. AMPA receptor structure and auxiliary subunits. *Journal of Physiology* **599**, 453–469 (2020).
189. Maher, M. P. *et al.* Discovery and characterization of AMPA receptor modulators selective for TARP- γ 8. *Journal of Pharmacology and Experimental Therapeutics* **357**, 394–414 (2016).
190. Hoshino, H. *et al.* Cornichon-like protein facilitates secretion of HB-EGF and regulates proper development of cranial nerves. *Mol Biol Cell* **18**, 1143–52 (2007).
191. Boudkkazi, S., Brechet, A., Schwenk, J. & Fakler, B. Cornichon2 dictates the time course of excitatory transmission at individual hippocampal synapses. *Neuron* **82**, 848–858 (2014).
192. Herring, B. E. *et al.* Cornichon proteins determine the subunit composition of synaptic AMPA receptors. *Neuron* **77**, 1083–96 (2013).
193. Coombs, I. D. *et al.* Cornichons modify channel properties of recombinant and glial AMPA receptors. *J Neurosci* **32**, 9796–804 (2012).
194. Nakagawa, T. Structures of the AMPA receptor in complex with its auxiliary subunit cornichon. *Science* **366**, 1259–1263 (2019).
195. Haering, S. C., Tapken, D., Pahl, S. & Hollmann, M. Auxiliary subunits: shepherding AMPA receptors to the plasma membrane. *Membranes (Basel)* **4**, 469 (2014).
196. Jacobi, E. & Engelhardt, J. Modulation of information processing by AMPA receptor auxiliary subunits. *J Physiol* **599**, 471–483 (2020).
197. Kirk, L. M. *et al.* Distribution of the SynDIG4/proline-rich transmembrane protein 1 in rat brain. *Journal of Comparative Neurology* **524**, 2266–2280 (2016).
198. Díaz, E. Beyond the AMPA receptor: Diverse roles of SynDIG/PRRT brain-specific transmembrane proteins at excitatory synapses. *Curr Opin Pharmacol* **58**, 76–82 (2021).
199. Kalashnikova, E. *et al.* SynDIG1: An activity-regulated, AMPA receptor-interacting transmembrane protein that regulates excitatory synapse development. *Neuron* **65**, 80–93 (2010).

200. Troyano-Rodriguez, E., Mann, S., Ullah, R. & Ahmad, M. PRRT1 regulates basal and plasticity-induced AMPA receptor trafficking. *Molecular and Cellular Neuroscience* **98**, 155–163 (2019).
201. Martin, E. E., Wleklinski, E., Hoang, H. T. M. & Ahmad, M. Interaction and subcellular association of PRRT1/SynDIG4 with AMPA receptors. *Front Synaptic Neurosci* **13**, 705664 (2021).
202. Hastie, P. *et al.* AMPA receptor/TARP stoichiometry visualized by single-molecule subunit counting. *PNAS* **110**, 5163–5168 (2013).
203. Zhao, Y., Chen, S., Yoshioka, C., Bacongus, I. & Gouaux, E. Architecture of fully occupied GluA2 AMPA receptor–TARP complex elucidated by cryo-EM. *Nature* **536**, 108–111 (2016).
204. Herguedas, B. *et al.* Architecture of the heteromeric GluA1/2 AMPA receptor in complex with the auxiliary subunit TARP- γ 8. *Science* **364**, 6438 (2019).
205. Lu, W. *et al.* Subunit composition of synaptic AMPA receptors revealed by a single-cell genetic approach. *Neuron* **62**, 254 (2009).
206. Nakagawa, T., Cheng, Y., Ramm, E., Sheng, M. & Walz, T. Structure and different conformational states of native AMPA receptor complexes. *Nature* **433**, 545–549 (2005).
207. Jacobi, E. & von Engelhardt, J. AMPA receptor complex constituents: Control of receptor assembly, membrane trafficking and subcellular localization. *Molecular and Cellular Neuroscience* **91**, 67–75 (2018).
208. Kato, A. S. *et al.* Hippocampal AMPA receptor gating controlled by both TARP and cornichon proteins. *Neuron* **68**, 1082–1096 (2010).
209. Dawe, G. B. *et al.* Nanoscale mobility of the apo state and TARP stoichiometry dictate the gating behavior of alternatively spliced AMPA receptors. *Neuron* **102**, 976–992 (2019).
210. Hume, R. I., Dingledine, R. & Heinemann, S. F. Identification of a site in glutamate receptor subunits that controls calcium permeability. *Science* **253**, 1028–1031 (1991).
211. Whitehead, G., Regan, P., Whitcomb, D. J. & Cho, K. Ca²⁺-permeable AMPA receptor: A new perspective on amyloid-beta mediated pathophysiology of Alzheimer's disease. *Neuropharmacology* **112**, 221–227 (2017).
212. Kwak, S. & Weiss, J. H. Calcium-permeable AMPA channels in neurodegenerative disease and ischemia. *Curr Opin Neurobiol* **16**, 281–287 (2006).
213. Liu, S. J. & Zukin, R. S. Ca²⁺-permeable AMPA receptors in synaptic plasticity and neuronal death. *Trends Neurosci* **30**, 126–134 (2007).
214. Punjani, A., Rubinstein, J. L., Fleet, D. J. & Brubaker, M. A. cryoSPARC: algorithms for rapid unsupervised cryo-EM structure determination. *Nat Methods* **14**, 290–296 (2017).

215. Kawate, T. & Gouaux, E. Fluorescence-detection size-exclusion chromatography for precrystallization screening of integral membrane proteins. *Structure* **14**, 673–681 (2006).
216. Chen, S. & Gouaux, E. Structure and mechanism of AMPA receptor — auxiliary protein complexes. *Curr Opin Struct Biol* **54**, 104–111 (2019).
217. Sans, N. *et al.* Aberrant formation of glutamate receptor complexes in hippocampal neurons of mice lacking the GluR2 AMPA receptor subunit. *Journal of Neuroscience* **23**, 9367–9373 (2003).
218. Coleman, S. K. *et al.* Aggregation limits surface expression of homomeric GluA3 receptors. *J Biol Chem* **291**, 8784 (2016).
219. Reinders, N. R. *et al.* Amyloid- β effects on synapses and memory require AMPA receptor subunit GluA3. *PNAS* **113**, (2016).
220. Antunes, F. M., Rubio, M. E. & Kandler, K. Role of GluA3 AMPA receptor subunits in the presynaptic and postsynaptic maturation of synaptic transmission and plasticity of endbulb–bushy cell synapses in the cochlear nucleus. *Journal of Neuroscience* **40**, 2471–2484 (2020).
221. Gutierrez-Castellanos, N. *et al.* Motor learning requires purkinje cell synaptic potentiation through activation of AMPA-receptor subunit GluA3. *Neuron* **93**, 409 (2017).
222. Salin, P. A., Malenka, R. C. & Nicoll, R. A. Cyclic AMP mediates a presynaptic form of LTP at cerebellar parallel fiber synapses. *Neuron* **16**, 797–803 (1996).
223. Nuriya, M. & Huganir, R. L. Regulation of AMPA receptor trafficking by N-cadherin. *J Neurochem* **97**, 652–661 (2006).
224. Matthews, P. M., Pinggera, A., Kampjut, D. & Greger, I. H. Biology of AMPA receptor interacting proteins - From biogenesis to synaptic plasticity. *Neuropharmacology* **197**, 108709 (2021).
225. Sia, G. M. *et al.* Interaction of the N-terminal domain of the AMPA receptor GluR4 subunit with the neuronal pentraxin NP1 mediates GluR4 synaptic recruitment. *Neuron* **55**, 87–102 (2007).
226. Thalhammer, A., Everts, I. & Hollmann, M. Inhibition by lectins of glutamate receptor desensitization is determined by the lectin's sugar specificity at kainate but not AMPA receptors. *Molecular and Cellular Neuroscience* **21**, 521–533 (2002).
227. Copits, B. A., Vernon, C. G., Sakai, R. & Swanson, G. T. Modulation of ionotropic glutamate receptor function by vertebrate galectins. *J Physiol* **592**, 2079 (2014).
228. Rossmann, M. *et al.* Subunit-selective N-terminal domain associations organize the formation of AMPA receptor heteromers. *EMBO J* **30**, 959 (2011).
229. Smith, T. C. & Howe, J. R. Concentration-dependent substate behavior of native AMPA receptors. *Nat Neurosci* **3**, 992–997 (2000).

230. Jin, R., Banke, T. G., Mayer, M. L., Traynelis, S. F. & Gouaux, E. Structural basis for partial agonist action at ionotropic glutamate receptors. *Nat Neurosci* **6**, 803–810 (2003).
231. Prieto, M. L. & Wollmuth, L. P. Gating modes in AMPA receptors. *The Journal of Neuroscience* **30**, 4449 (2010).
232. Smith, T. C., Wang, L. Y. & Howe, J. R. Heterogeneous conductance levels of native AMPA receptors. *The Journal of Neuroscience* **20**, 2073 (2000).
233. Matthies, D. *et al.* Cryo-EM structures of the magnesium channel CorA reveal symmetry break upon gating. *Cell* **164**, 747–756 (2016).
234. Liu, F., Zhang, Z., Csanády, L., Gadsby, D. C. & Chen, J. Molecular structure of the human CFTR ion channel. *Cell* **169**, 85–95 (2017).
235. Mathes, A. & Engelhardt, H. Nonlinear and asymmetric open channel characteristics of an ion-selective porin in planar membranes. *Biophys J* **75**, 1255–1262 (1998).
236. Li, J., Sheng, S., Perry, C. J. & Kleyman, T. R. Asymmetric organization of the pore region of the epithelial sodium channel. *Journal of Biological Chemistry* **278**, 13867–13874 (2003).
237. Ekstrom, A. D. *et al.* Human hippocampal theta activity during virtual navigation. *Hippocampus* **15**, 881–889 (2005).
238. Kandel, E. R. & Spencer, W. A. Electrophysiology of hippocampal neurons. II. Afterpotentials and repetitive firing. *J Neurophysiol* **24**, 243–259 (1961).
239. Diener, H. -C & Dichgans, J. Pathophysiology of cerebellar ataxia. *Movement Disorders* **7**, 95–109 (1992).
240. Takakusaki, K. Functional neuroanatomy for posture and gait control. *J Mov Disord* **10**, 1 (2017).
241. Lalanne, T., Oyrer, J., Farrant, M. & Sjöström, P. J. Synapse type-dependent expression of calcium-permeable AMPA receptors. *Front Synaptic Neurosci* **10**, 34 (2018).
242. Bellone, C. & Lüscher, C. Cocaine triggered AMPA receptor redistribution is reversed in vivo by mGluR-dependent long-term depression. *Nat Neurosci* **9**, 636–641 (2006).
243. Goffer, Y. *et al.* Calcium-permeable AMPA receptors in the nucleus accumbens regulate depression-like behaviors in the chronic neuropathic pain state. *The Journal of Neuroscience* **33**, 19034 (2013).
244. Greger, I. H., Watson, J. F. & Cull-Candy, S. G. Structural and functional architecture of AMPA-type glutamate receptors and their auxiliary proteins. *Neuron* **94**, 713–730 (2017).
245. Penn, A. C., Williams, S. R. & Greger, I. H. Gating motions underlie AMPA receptor secretion from the endoplasmic reticulum. *EMBO J* **27**, 3056–68 (2008).

246. Boudreau, A. C. & Wolf, M. E. Behavioral sensitization to cocaine is associated with increased AMPA receptor surface expression in the nucleus accumbens. *Journal of Neuroscience* **25**, 9144–9151 (2005).